COMPREHENSIVE STUDY OF THE ELECTROCHEMICAL FORMATION OF THIN OXIDE LAYERS ON NICKEL AND THE ELECTROCHEMICAL REDUCTION OF MONOLAYER OXIDES ON PLATINUM

By

Mohammad Alsabet

A thesis submitted to the Department of Chemistry

in conformity with the requirements for

the degree of Doctor of Philosophy

Queen's University

Kingston, Ontario, Canada

February, 2011

ABSTRACT

The anodic polarization of Ni electrode in 0.5 M aqueous KOH solution at various polarization potential (E_p), time (t_p) and temperature (T) values leads to the formation of β-$Ni(OH)_2$ films. The growth of the hydroxide layers are irreversible and cannot be reduced electrochemically to metallic Ni. The hydroxide layer becomes thicker at higher values of E_p and/or t_p and/or T. The thickness of β-$Ni(OH)_2$ hydroxide were determined using ex–situ XPS and depth–profile techniques. Application of the oxide growth theories to our data indicate that the development of the β-$Ni(OH)_2$ layer follows inverse logarithmic growth kinetics. The driving force of the process is the strong electric field that is established across the oxide layer. The strength of electric field is in the range of $0.015 - 0.197 \times 10^9$ V m^{-1}.

The oxidation mechanism of the Ni(II) surface compound to Ni(III) is electrochemically irreversible and the process is treated according to Randles–Sevcik equation. A linear relation was determined between the peak current density (j_p) and the square root of the potential scan rate ($v^{1/2}$) for the entire range of E_p, t_p and T. The diffusion coefficient (D) values calculated for anodic and cathodic processes are 8.1 ± 0.2 x 10^{-12} and 4.3 ± 0.2 x 10^{-12} cm^2 s^{-1}, respectively. The activation energy (E_a) values for the diffusion process are 23 ± 2 kJ mol^{-1} (anodic) and 26 ± 2 kJ mol^{-1} (cathodic). The D and E_a values calculated from chronoamperometry measurements are comparable with those calculated from j_p vs. $v^{1/2}$ plots.

The electro–reduction of PtO electrochemically pre–formed on Pt electrode in 0.5 M aqueous H_2SO_4 solution was also investigated. A well–controlled reduction conditions (E_r, t_r and T) were applied to determine the amount of the reduced PtO oxide. The reduction of the PtO requires much less time once ca. 1 monolayer (ML) of the oxide has been removed (ca. 1 ML of PtO remains). As expected, the longer t_r and/or lower E_r values, the greater the amount of the reduced oxide and consequently the smaller the amount of the remaining PtO oxide.

CO-AUTHORSHIP

All work done in this thesis was carried out by the author in the Department of Chemistry at Queen's University under the supervision of Dr. Gregory Jerkiewicz. The entire experimental work was carried out by the author, while the NiOOH growth results analysis were done in collaboration with Dr. Michal Grden, a postdoctoral fellow from Warsaw University, who worked on another Ni–related project in our laboratory. Dr. Grden will be a co–author on the future resulting papers.

ACKNOWLEDGEMENTS

I would like to express my sincere appreciation to my supervisor, Dr. Gregory Jerkiewicz, for all his support, patience and guidance throughout the course of this research. I would also like to extend my sincere thanks to Dr. Michal Grden for all the invaluable science discussions and debates we had, which generated many interesting theories.

I would also like to thank the members of the Jerkiewicz laboratory, the former and the current ones; Dr. Michal Grden, Dr. Baodong Zhao, Dr. Maja Obradovic, Dr. Shin-ichi Tanaka, Julia van Drunen, Rebecca Holmberg, Alessandra Lucredio, Andrew Munro, Edward Thomas and Yoseif Makonnen for their friendship and humor that made my days eventful.

I am also very grateful to my committee members, Dr. Richard Oleschuk and Dr. Hans-Peter Loock, for their advice and suggestions. I also would like to acknowledge the financial support from Kuwait University.

Above all and most importantly, I would like to express my special thank to my parents and my wife for all their prayers, love, and support throughout my entire M.Sc. and Ph.D. studies, which I will never be able to pay back.

STATEMENT OF ORIGINALITY

This work represents the first qualitative and quantitative results for the electro–oxidation of nickel electrode in the potential region where the β-$Ni(OH)_2$ formation takes place. Furthermore, a comprehensive set of data for the electro–oxidation of Ni(II) to NiOOH is presented. All the experimental work was carried out in alkaline solution and the kinetics of the process was analyzed. A comprehensive set of results for the electro–reduction of PtO was obtained in order to assess the kinetics of the process. To the best of the author's knowledge, this is the first detailed study of this type.

TABLE OF CONTENTS

LIST OF FIGURES

LIST OF TABLES

ABBREVIATIONS AND SYMBOLS

AES	Auger Electron Spectroscopy
AFM	Atomic Force Microscopy
BE	Binding Energy
CA	Chronoamperometry
CC	Chronocoulometry
CPE	Constant Potential Electrolysis
CV	Cyclic Voltammetry
DCA	DC Potential Amperometry
EIS	Electrochemical Impedance Spectroscopy
EQCN	Electrochemical Quartz–Crystal Nanobalance
ESCA	Electron Spectroscopy for Chemical Analysis
G–C	Gouy–Chapman model (A model of electric double layer in which the thermal motion is taken into account)
GDP	Gross Domestic Product
HOR	Hydrogen Oxidation Reaction
IHP	Inner Helmholtz Plane
KE	Kinetic Energy
LCD	Liquid Crystal Display
LSV	Linear Sweep Voltammetry

ML	Mono–Layer
NACE	National Association of Corrosion Engineers
NLLS	Non–Linear Least Square
OER	Oxygen Evolution Reaction
OHP	Outer Helmholtz Plane
PEM	Proton Exchange Membrane or Photon Emission Microscopy (as referred to it in the text)
Poly	Polycrystalline
r.d.s.	Rate Determining Step
RHE	Reversible Hydrogen Electrode
SCC	Stress Corrosion Cracking
SCE	Standard Calomel Electrode
SCR	Space Charge Region
SHE	Standard Hydrogen Electrode
SOC	State Of Charge
SXS	Soft/Surface X–ray scattering
UHV	Ultra High Vacuum
XPS	X–ray Photoelectron Spectroscopy
XRD	X–ray Diffraction
$\emptyset_M$	Electric potential of a metal in V
$\emptyset_s$	Electric potential of a solution in V
[A]	Concentration of a substance A

Γ_o	Surface coverage
Γ_m	Surface concentration of one monolayer coverage
$\Delta_r G^o$	Standard Gibbs energy change of a reaction
$\Pi_{a\ \mathrm{ox}}$	Products of activities of oxidized species
$\Pi_{a\ \mathrm{red}}$	Products of activities of reduced species
C_{ox}^{∞}	Concentration of the electroactive species in the solution bulk in mol cm^{-3}
D	Diffusion coefficient in cm s^{-1}
$D_{Ni(OH)_2}$	Diffusion coefficient of the proton in the $Ni(OH)_2$ layer in cm s^{-1}
D_{ads}	Adsorption coefficient (the ratio between the mass of the adsorbed substance to the concentration of the substance in the solution)
D_{NiOOH}	Diffusion coefficient of the proton in the NiOOH layer in cm s^{-1}
D_{eff}	Effective diffusion in cm s^{-1}
E_{corr}	Corrosion potential in V
N_{trap}	Concentration of the proton trap
Z_{A}	Charge of a substance A
a'	Distance between the metal cation and the top of the activation energy barrier (usually assumed to be 1.72 Å)
a_{A}	Activity or the effective concentration of a substance A
d_{L}	Limiting thickness of the oxide/hydroxide in nm
j_{a}	Anodic current density in A cm^{-2}
j_{c}	Cathodic current density in A cm^{-2}
j_{corr}	Corrosion current density in A cm^{-2}

j_o	Exchange current density in A cm^{-2}
j_{diff}	Rate of diffusion (diffusion flux)
j_α	Diffusional transport according to Fick's law of diffusion
k_B	Boltzmann constant ($1.3806503 \times 10^{-23}$ m^2 kg s^{-2} K^{-1})
n_α	Number of electrons passed in the rate determining step
$v_{de-trap}$	Rate of proton de-trapping
v_{trap}	Rate of proton trapping
ε_o	Vacuum permittivity (8.85419×10^{-12} J^{-1} C^2 m^{-1})
ε_r	Dielectric permittivity of semi–conducting layer J^{-1} C^2 m^{-1}
$\bar{\mu}$	Electrochemical potential in V
μ_{ideal}	Chemical potential of the ideal solution at the same molality
A_{geom}	Geometric surface area of the electrode in cm^{-2}
A_r	Real surface area of the electrode in cm^{-2}
b	Molality in mol kg^{-1}
b_o	Molality of a substance at standard state in mol kg^{-1}
C_{dl}	Double layer capacitance in F cm^{-2}
C_{sc}	Space charge capacitance in F cm^{-2}
d	Thickness of the oxide or hydroxide in nm
D	Intensity of an XPS peak
D_o	Diffusion coefficient at infinite T value (constant)
E	Electric field in V nm^{-1}

E_1	Potential at which the oxidation peak of α-$Ni(OH)_2$ stars in V
E_2	Potential at which the oxidation peak of α-$Ni(OH)_2$ ends in V
E_a	Activation energy
E_{crit}	Critical potential in V
E_f	Final potential in V
E_F	Fermi energy level
E_{fb}	Flat–band potential
E_i	Initial potential in V
E_{irr}	Irreversible potential of the electrode (not equal to the standard electrode potential, E^o) in V
E_{mix}	Mixed potential
E^o	Standard electrode potential in V
E_p	Polarization potential in V
E_{pass}	Passive potential in V
E_r	Reduction potential in V
E_v	Vacuum energy level
F	Faraday's constant (96485.3415 s A mol^{-1})
f	Frequency in Hz
h	Planck constant (6.626068×10^{-34} m^2 kg s^{-1})
H_i	Enthalpy of solution of the cation in the oxide
I_{para}	Number of parallel processes
I	Intercept

I_{ox}	Oxygen evolution current density in A cm^{-2}
j_m	Total angular momentum
j_p	peak current density in A cm^{-2}
j_{pass}	Passive current density in A cm^{-2}
j_{tot}	Total current density in A cm^{-2}
k_i	Rate constant of trapping and de–trapping processes
L	Thickness of the depleted layer
ℓ	Angular quantum number
M	Molecular weight of the dissolved metal in g mol^{-1}
M_p	Number of moles of the cation M
n	Number of electrons transferred in the process
n_{ion}	Number of metal ions per unit volume
N	Surface density of atoms
O_{chem}	Chemisorbed oxygen
p	pressure in atm
p–type	Positive type semiconductor
Q_{hox}	Charge of the hydroxide in C
q_{mono}	Charge density associated with the formation of one monolayer in C cm^{-2}
q_{ox}	Charge density of the oxide in C cm^{-2}
q_{ox1}	Charge density of the Ni(II) oxidation peak till peak maximum in C cm^{-2}
q_{red}	Charge density of the reduced oxide in C cm^{-2}

q_{rm}	Charge density of the remaining (unreduced) oxide in C cm^{-2}
R	Gas constant (8.314472 J K^{-1} mol^{-1})
R_f	Roughness factor (A_r/A_{geom})
s	Magnetic field of spin
S	Slope
T	Temperature in K
t_p	Polarization time in s
t_r	Reduction time in s
U	Activation energy barrier
v	Frequency of the radiation
V	Potential drop across the oxide in V
v	Scan rate in mV s^{-1}
v_{ib}	Vibration frequency of the surface metal atom
w	Rate of weight loss in g cm^{-2}
W	A function of the slope and the intercept of Eq. 5.3 independent of V
X_q	Number of moles of the anion X
α	Transfer coefficient
ΔE_p	Peak separation in V
$\Delta\phi$	Galvani potential difference
κ	Dielectric constant of the oxide/hydroxide film
Ψ	Outer potential in V (a component of the inner potential of a metal)

Ω	Volume of the oxide per metal atom
a	Distance between two metal cations (i.e. M^{n+}–M^{n+})
a'	Distance between a metal atom and metal cation (i.e. M–M^{n+})
γ	Activity coefficient
η	Overpotential in V
λ	Mean free path
μ	Chemical potential
μ^o	Standard chemical potential
χ	Surface potential in V (a component of the inner potential of a metal)
ϕ	Work function

Chapter 1 – Introduction

Nickel is widely used to manufacture stainless steels, i.e. specialty alloys that are often used to construct a variety of objects that span from stainless steel structure to daily use as kitchen utensils [1,2]. It resists atmospheric corrosion by forming a surface oxide/hydroxide layer, which protects the bulk of the metal. Maximovitch et al. [3] showed that the oxidation of nickel is limited to the surface region and results in the formation of a hydroxide film on the metal surface. In relation to electrochemical science and engineering, Ni and Ni–containing alloys, as a corrosion resistance material, are used to electroplate the less–resistant metals/alloys, as electro–catalysts for water electrolyzers in basic media [4], in electrochromic devices [5], and in electro–oxidation of alcohols and amines [6]. Mechanical, chemical and catalytic properties of nickel and its corrosion resistance make it a suitable material for the chemical, automotive, and electronics industries. Nickel is used as an electrode in various batteries (e.g. Ni-Cd, Ni-Fe, Ni-Zn, etc.) and in alkaline fuel cells due to its electro–catalytic properties [7]. It is a very important constituent of many alloys and super–alloys used in construction of e.g. metallic structures subjected to high temperature, since Ni–based alloys retain much of the nickel's strength at high temperature. Nickel is stable in alkaline media and for this reason is considered a good catalyst for the hydrogen oxidation reaction (HOR) and serves as an alternative to platinum, which is expensive and whose availability is limited [8].

Nickel oxide/hydroxide is a material often used as an electrode that exists in four structural phases: α-$Ni(OH)_2$, β-$Ni(OH)_2$, γ-NiOOH and β-NiOOH [9]. The initial stage

of Ni electro–oxidation occurs at potential values ≤ 0.5 V vs. the reversible hydrogen electrode (RHE). The α-$Ni(OH)_2$ phase is considered the product of the electro–oxidation of metallic Ni at this potential [10-17]. Some data suggest that the oxide formed in this potential range could contain NiO [15,18-21]. At more positive potentials, α-$Ni(OH)_2$ is slowly transformed to β-$Ni(OH)_2$ as well as oxidation of the metallic Ni at the metal–hydroxide interface takes place. The transformation of α-$Ni(OH)_2$ to β-$Ni(OH)_2$ phase is irreversible in the sense that β-$Ni(OH)_2$ cannot be converted to α-$Ni(OH)_2$ by changing the applied potential or using other simple approaches. In addition, the α-$Ni(OH)_2$ phase has higher charge/discharge capacity than that of β-$Ni(OH)_2$. Thus, stabilization of the α-$Ni(OH)_2$ form is a subject of interest to battery technologists [22-26]. At potential values ≥ 1.3 V (RHE), both phases of $Ni(OH)_2$ are further oxidized to NiOOH species. Despite numerous studies on the nickel electrode behavior in alkaline media, the mechanisms by which the oxidation proceeds are not yet completely understood (no detailed studies for the oxidation kinetics). In particular, the kinetics and the mechanisms of formation of the various Ni hydroxides and oxyhydroxides and knowledge of their structure in the form of thin films are still a subject of research [9].

The development of surface oxides on platinum is an extensively studied subject because Pt is a noble metal and serves as a model system in research on oxide growth at non–noble metals. Platinum is chemically inert and it is a very effective catalyst for many catalytic processes and is used in fuel cells. The electro–oxidation refers to the polarization conditions which result in the formation of an oxide. The oxide growth kinetics, mechanisms and determination of respective rate–determining steps can be investigated using a variety of electrochemical techniques combined with surface–science

techniques [27-36]. The electro–oxidation of Pt starts at ca. 0.80 V (RHE) and at the present time the process is known to proceed according to the following steps [37]: discharge of the water molecule which leads to two hydrated protons (H^{+}_{aq}) and a chemisorbed oxygen (O_{chem}) (Eq. 1.1) followed by a formation of quasi–3D lattice of PtO in a place–exchange process (Eq. 1.2):

$$Pt + H_2O \xrightarrow{\text{electro-adsorption}} Pt^{\delta+}\text{-}\,O^{\delta-}_{Chem} + 2H^{+}_{aq} + 2e^{-} \qquad (1.1)$$

$$Pt^{\delta+}\text{-}\,O^{\delta-}_{Chem} \xrightarrow{\text{quasi-3D lattice formation}} Pt^{2+}\text{-}\,O^{2-} \qquad (1.2)$$

These equations represent a stable surface compound that can be detected using different interfacial techniques, such as cyclic voltammetry (CV), Auger electron spectroscopy (AES) and electrochemical quartz–crystal nanobalance (EQCN). At potentials greater than 1.5 V (RHE), PtO_2 starts to develop on top of the PtO layer previously formed at low potentials. The reduction of PtO was studied in different acidic, alkaline and neutral media, such as HF, $HClO_4$, H_2SO_4, and phosphate buffer solution at different pH values [38-47]. The reduction of PtO commences at ca. 0.75 V (RHE), while the reduction of PtO_2 occurs at less–positive potentials [34]. This means, during a single negative–going potential scan (sweep), the underlying PtO layer is reduced first leaving the PtO_2 layer in contact with the Pt substrate (*metal*–PtO_2–*electrolyte* interphase). The PtO_2 oxide is then reduced at less positive potential values. In the presence of dissolved hydrogen and under

open–circuit conditions, the reduction of the PtO layer residing on the electrode surface follows the following equation (the rate determining step is the dissociative adsorption of hydrogen):

$$PtO + H_2 \longrightarrow Pt + H_2O \qquad (1.3).$$

Shibata et al. [43] reported that the reduction rate of the multilayer PtO in $HClO_4$ solution depends on the hydrogen coverage. Barz et al. [38] reported that the dissociation of the adsorbed hydrogen is the rate determining step and the reduction of PtO in H_2SO_4 and in the presence of hydrogen, follows an island mechanism. A variety of electrochemical and interfacial techniques was applied to study the PtO electro–reduction, i.e. galvanostatic transient, linear potential sweep, chronoamperometry, rotating ring–disc electrode, and double beam photoemission spectroscopy [42-46,48]. In spite of these efforts, the kinetics and mechanism of the process and the elementary steps involved in it are not well understood.

The first objective of this research is to investigate the mechanism of electro–oxidation of metallic nickel and of the elementary steps involved at well–defined polarization potential (E_p), polarization time (t_p) and temperature (T) conditions. The second objective is to study the electro–reduction of a pre–formed PtO layer at well–defined reduction potential (E_r), reduction time (t_r) and T conditions. These two metals have a wide span of industrial and catalytic applications because of their unique properties (catalytic activity, applicability to fuel cells, corrosion resistance, etc.).

Following this research, nickel and platinum will serve as model systems in the electro–oxidation studies of other non–noble and noble metals. An exhaustive set of data was collected and the results were subsequently modeled using various oxide–growth theories. The kinetics of electro–oxidation and electro–reduction can be studied in detail by application of a variety of complementary electrochemical, materials science and surface science techniques, such as cyclic and linear–sweep voltammetries (CV, LSV), X–ray photoelectron spectroscopy (XPS), Auger electron spectroscopy (AES), electrochemical impedance spectroscopy (EIS), electrochemical quartz–crystal nanobalance (EQCN) techniques and surface X–ray scattering (SXS) [49-64]. The outcome of this research contributes to an atomic–level comprehension of the mechanisms and kinetics of the electro–oxidation and electro–reduction of transition metals.

Chapter 2 – Background

2.1 History of Nickel

Nickel (Ni) is one of the few ferromagnetic metallic elements at room temperature (others are: Fe, Co and Gd) and is a silvery–white lustrous solid with slight golden tinge (Fig. 2.1) [65]. Nickel has the following chemical and physical properties: high melting and boiling points (1453°C and 2913°C, respectively), resistance to corrosion, hardness, attractive appearance, etc. Nickel and Ni–containing alloys are suitable materials for a variety of applications due to their properties. Nickel electroplating is extensively applied to provide corrosion resistance and visually attractive materials due to its lustrous appearance. The field of Ni plating on plastics, has expanded considerably in recent years and offers lightweight products, while providing appearance and protection characteristic of nickel. Electroforming of Ni can be used to manufacture items via deposition of Ni layer on a mandrel which retains the desired surface detail when the mandrel is removed at the end of the electroplating process (Fig. 2.2).

Figure 2.1. Nickel ore, Sudbury, Ontario [65].

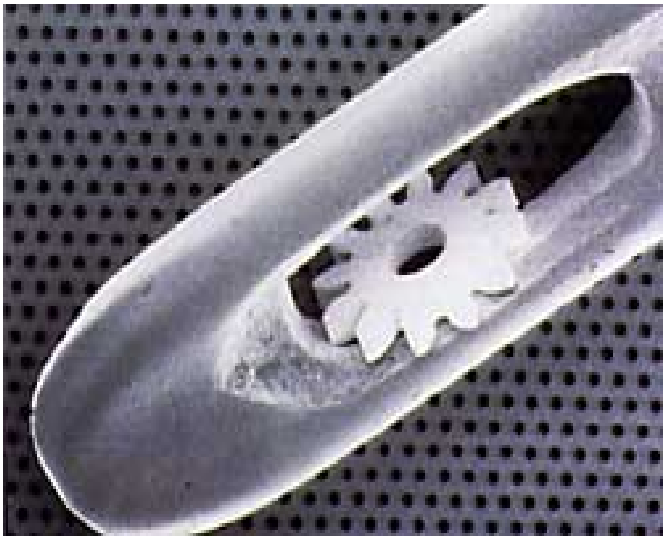

Figure 2.2. Electroformed nickel micro–gear in a needle eye [66].

About two–thirds of Ni applications are related to usage that requires corrosion resistance. One of the main applications is the manufacture of stainless steels, which provides stable and ductile corrosion–resistance material. Stainless steels are the main choice in the production lines for the manufacture of food and construction of medical instruments and devices because they are chemically stable and can be easily cleaned and maintain cleanliness. In the case of highly corrosive environments, such as marine, power generation, oil and gas industries, increase of the amount of Ni and addition of molybdenum, vanadium, chromium and other metals to the standard stainless steels leads to the formation of specialized alloys that resist general, pitting, crevice, and stress corrosion. Nickel combined with Cr, Mo and W forms alloys that possess superior corrosion–protection property. Therefore, nickel–based alloys in general can be used in more highly corrosive environments rather than regular stainless steels.

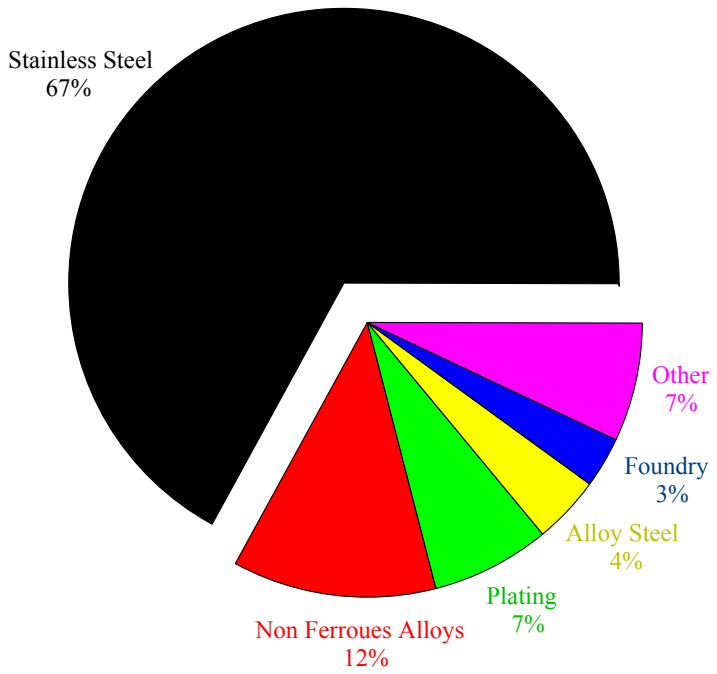

Figure 2.3. Nickel demand by application in 2006 [67].

The combination of physical and chemical properties of Ni (i.e. high boiling and melting points, formation of oxides, alloying ability, relatively low cost, longevity, etc.) make it suitable for a wide range of heat–resistant alloys that are very important materials in the chemical and aerospace industries. The equiatomic Ni-Ti alloys possess a unique property referred to as the shape–memory effect. An object made of this alloy that has been deformed recovers its original shape upon heating [2]. In addition, the Ni-Ti alloy exhibits a super–elasticity property upon heating, in which the elasticity increases about 20 – 30 times higher than the regular metal [2]. These type of alloys are biocompatible that make them suitable for use in orthopedic implants. Nickel and its oxides are very important materials in battery technologies [68,69]. There are several types of Ni rechargeable batteries such as nickel–cadmium battery (NiCd), nickel–metal hydride cell (NiMH), nickel–zinc battery (NiZn), Ni hydrogen battery (NiH_2), Ni–iron battery (NiFe) as well as the Ni oxyhydroxide primary battery (NiOx) which is non–rechargeable. Application of these batteries includes portable electronics, toys, emergency lighting, remote controls, cordless power tools, digital cameras, electric vehicles, etc. In the portable power provision industry, Ni-Cd rechargeable batteries which consist of nickel plates and nickel hydroxides have been used for several years. The high performance rechargeable NiMH batteries can have up to three times the capacity of NiCd battery with a comparable size.

Figure 2.4. Cast nickel–base alloys used in stationary gas turbine engine operates at temperatures > 650°C [66].

2.1.1 Corrosion of Nickel and Ni–Based Alloys

Nickel and nickel–based alloys are widely used in various industries due to their unique properties (high temperatures, highly corrosion resistance, etc.). Nickel resists atmospheric corrosion, as well it is stable in aqueous media. The corrosion rate of Ni and Ni–based alloys is typically less than ca. 0,0025 mm yr^{-1} with varying degrees of surface discoloration depending on the alloy. Addition of other chemical elements such as Cu and Mo, provides an improvement in the resistance of the Ni in non–oxidizing acids. Moreover, addition of chromium to the Ni improves the resistance to the oxidizing media

such as nitric and chromic acids. Molybdenum also enhances the resistance of Ni towards the pitting and crevice corrosion. Iron is used in the nickel–based alloys to reduce the costs and to improve the resistance of the Ni in sulfuric acid. Cobalt provides a unique strengthening characteristic to the Ni alloys which designed to be used in high temperature environments. In water, Ni and nickel–based alloys resist the stress corrosion cracking (SCC) in distilled and fresh water to a very decent extent. The Ni-Cu alloys known as alloy–400 and R–405 also have a very low corrosion rate in fresh water systems and can be used for valves and other pipe fittings.

2.2 History of Platinum

The origin of the word "platinum" was derived from the term "platina del Pinto" which is a Spanish term meaning "little silver of the Pinto River". Platinum was used by pre–Columbian Americans and was initially discovered by Charles Wood in 1741, and by Antonio de Ulloa in South America in 1746. The earth's crust contains only 0.003 ppm of platinum, which makes it thirty times less abundant than gold. The largest national suppliers of platinum and its group materials are South Africa, followed by Russia, and finally Canada. In Columbia and some western American states, platinum is commonly accompanied by small traces of osmium, palladium, iridium, rhodium, and ruthenium in nature. Platinum is more precious than gold or silver and as of February 2010 commercially pure Pt was worth, on average, $44 per gram. Pure platinum has a silvery–white color and is a dense, inert and ductile metal (see Fig. 2.5). The melting point of Pt is very high, ca. 1774°C, which is higher than that of gold. Platinum is insoluble in nitric

and hydrochloric acids, however, it dissolves in aqua–regia (1:3 nitric acid–hydrochloric acid mixture) and forms hexa chloroplatinic acid, H_2PtCl_6. Platinum resists corrosion in air at any temperature, but halogens, sulfur, caustic alkalis, and cyanides cause Pt to corrode. In general, corrosion is thermodynamically unfavorable for Pt (as well as other noble metals) and any corrosion products tend to decompose spontaneously to pure metal. The main applications of Pt are catalytic converters that are part of almost every automobile and jewelry. These two applications consume more than 70% of the world's supply of Pt, apart from all other known uses. Figure 2.6 shows the platinum demand by application in 2007.

Figure 2.5. Platinum nugget [70].

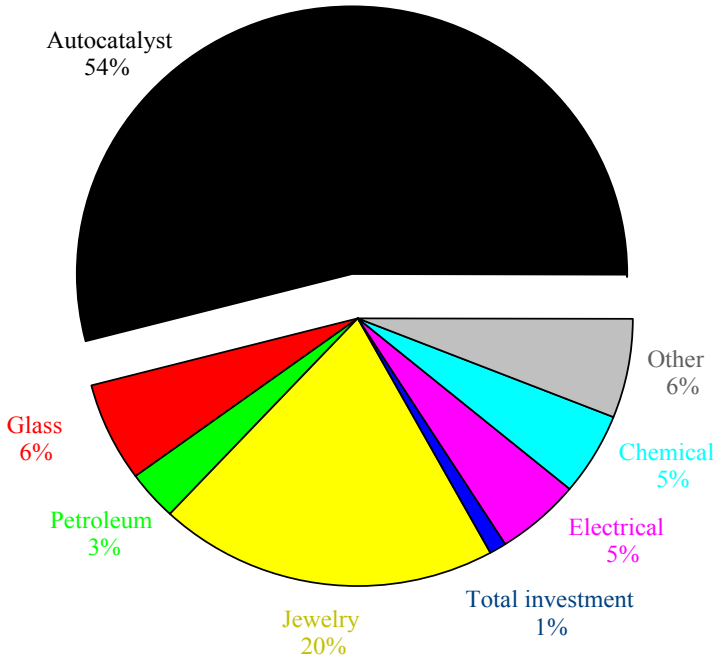

Figure 2.6. Platinum demand by application 2007 [data adapted from Ref. 71].

As a catalyst in a converter, Pt is used to convert the harmful gases in the exhaust system of an automobile, i.e. carbon monoxides and hydrocarbons, into carbon dioxide and water (also reduces the nitrogen oxides, such as NO or NO_2, to oxygen and nitrogen). In the most common type of fuel cell, i.e. the proton exchange membrane (PEM) fuel cells that employ H_2 gas as fuel, Pt is the effective element used as a catalyst for both hydrogen oxidation and oxygen reduction. Apart from their use in automobiles and as a replacement for conventional batteries, PEM fuel cells can also be used in power generation for buildings, or as generators for portable equipment. Platinum is also used as a homogeneous organometallic catalyst (the first organometallic compound was $K(C_2H_4)PtCl_3$ salt) [72]. The organometallic compounds are used as catalysts in synthesis of medicine in the pharmaceutical industry. Moreover, platinum is used in the

manufacturing of fiberglass, reinforced plastics, glass for liquid crystal displays (LCD), hard discs, and electronics.

2.3 Corrosion

Corrosion is the degradation of the properties of metals and alloys as a result of chemical reaction with the environment (oxygen, water, etc.), that begins on their surfaces. Basically, corrosion is the oxidation of a metal leading to the formation of metal cations, which are either dissolved in the phase being in contact with the corroding material or precipitate or deposit on the material as a salt or an oxide. When this effect is localized on a specific area of the metal surface (localized corrosion), it forms pits or cracks which provide sites for material fatigue to begin. The cost of corrosion can be very high and the risks associated with untreated corrosion are equally high. In the USA, the cost of corrosion as estimated by the National Association of Corrosion Engineers (NACE) is ca. $300 billion per year, which is about 3% of the gross domestic product (GPD) of the US. Also, corrosion may be costly in terms of human life and safety; it could lead to catastrophic collapses, explosions, or fires. Solutions to corrosion and valuable information about the process may be obtained through careful examination of the corroding system. There is a general agreement that is ca. 25% of the cost of corrosion can be saved by adequate application of the existing technology of corrosion detection and control. In the case of aqueous corrosion, some of the environmental factors that affect the corrosion rate are pH or acidity, temperature, presence of oxidizing agents, electrolyte composition and solute concentration.

The deterioration of metals occurs in all industrial, urban, marine, and agricultural environments, where the metals are in contact with water (or air moisture), acids, bases, salts, oils, aggressive metal polishes, or other solid and liquid chemicals. Furthermore, some materials will corrode when they are in contact with gaseous phases containing ammonia, acid vapors, or sulfur–containing gases. Corrosion is commonplace in many industries, for example in the chemical and petrochemical industries, electric power generation plants, desalination plants, transportation systems, water and sewer systems. Since corrosion is a surface process, the rate of corrosion can be expressed as mass loss of the material; mass loss per unit area per time is typically given in mg cm^{-2} s^{-1} or g m^{-2} yr^{-1}. This definition has a significant meaning only in the case of uniform corrosion and cannot be readily applied to localized corrosion. The corrosion rate can also be expressed as penetration rates, the rate of decrease or loss of the thickness of the material; in this case, the corrosion rate is given in cm s^{-1}. If the corrosion rate is expressed as mass loss, then it can be related to the corrosion current density through the Faraday's law, equation 2.1.

$$j_{\mathrm{corr}} = n\mathrm{F}\,\frac{\mathrm{W}}{\mathrm{M}} \tag{2.1}$$

where j_{corr} is the corrosion current density in A cm^{-2}, n is the number of electrons transferred in the process, F is the Faraday constant, W is the rate of mass loss in g cm^{-2} s^{-1}, and M is the molecular weight of the dissolving metal in g mol^{-1}. The corrosion current density is equivalent to the rate of dissolution of the metal surface into metal ions. Furthermore, in some cases, where the corrosion process is accompanied by an increase

in the weight of the test sample due to formation of insoluble oxides, hydroxides, etc. that adhere to the metal surface, the corrosion rate can be expressed as weight gain of the sample per unit of time.

This study focuses on the electrolytic corrosion of Ni and Pt, which occurs at the metal–electrolyte interface involving oxidation of a metal and reduction of an oxidizing agent. It has to be remembered that when a metal oxidizes (corrodes), then the electrons released must be consumed in a simultaneously occurring reduction process, so that electro–neutrality is maintained.

2.3.1 Forms of Corrosion

There are many forms of metallic corrosion, such as uniform/general corrosion, atmospheric corrosion, high temperature corrosion, pitting corrosion, stress cracking corrosion, hydrogen embrittlement, de–alloying or selective corrosion, just to mention a few. In order to avoid corrosion, one must learn to recognize the different forms of corrosion and the driving conditions or parameters that influence each type. Generally, there are eight forms of corrosion in which some of them may be categorized in the same group as they share certain similarities, i.e. pitting corrosion and crevice corrosion fall in the category of localized corrosion [73]. The basis of this classification is the appearance of the corroded metal, in which each of those forms may be identified by simple visual characteristics of the morphology of the attacked surface (sometimes the naked eye is inadequate, and magnification is required).

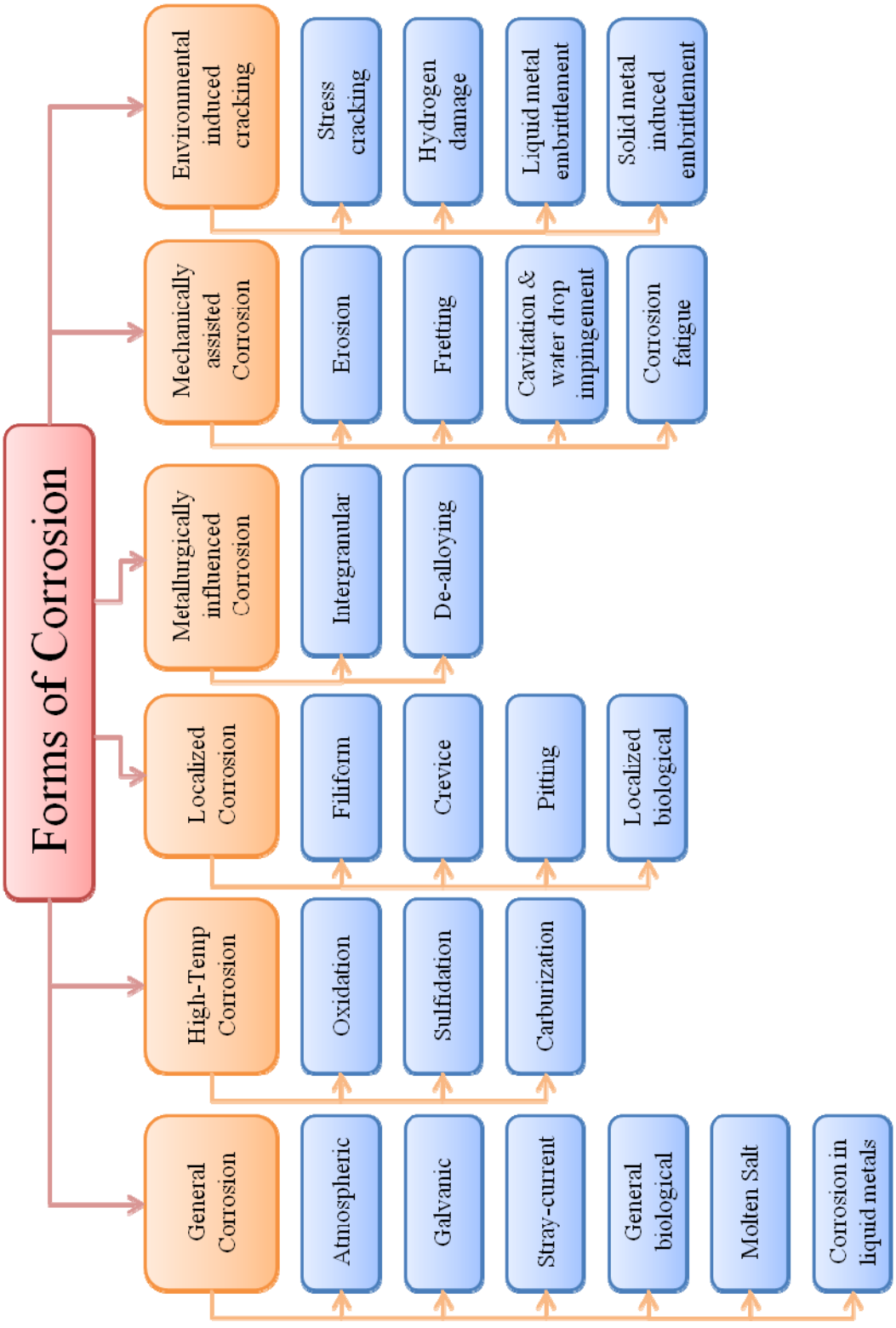

Figure 2.7. Forms of corrosion chart [74].

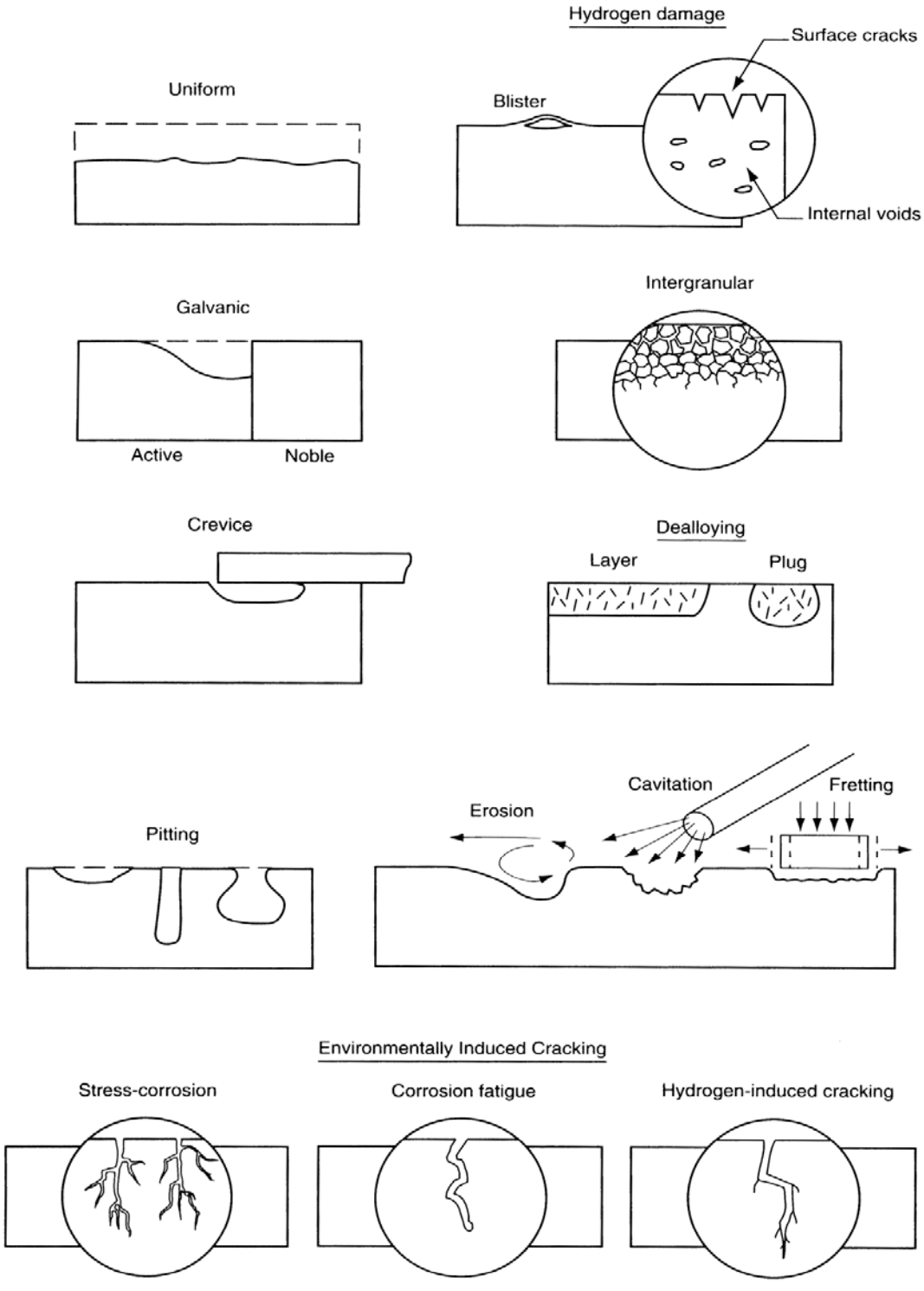

Figure 2.8. Types of metallic corrosion [74].

2.3.1.1 General or Uniform Corrosion

General corrosion, also called uniform corrosion, is the most common form of corrosion where the metal corrodes evenly over the entire exposed surface. As a result, the amount of unreacted metal decreases, while a corrosion product, typically a metal oxide, develops. From the corrosion protection point of view, the life time of a system (equipment) that is uniformly attacked by corrosion can be estimated with a very high degree of certainty by monitoring the weight change of the metal specimen in the same environment. Application of a suitable protective coating is a common method of preventing or reducing the rate of this type of corrosion.

2.3.1.2 Localized Corrosion

Localized corrosion is one of the most destructive and dangerous forms of corrosion. It starts at particular locations on the metal surface and penetrates into the bulk causing local but severe damage to the metal. Unlike general corrosion, localized corrosion is not accompanied by significant weight change or thinning of the material. It is divided into (i) crevice corrosion and (ii) pitting corrosion. Crevice corrosion is an intense localized corrosion often occurring within crevices or protected areas exposed to corrosive environments. Pitting corrosion is an extremely localized attack resulting in the formation of holes (pits) in the metal, hence its name. Generally, a pit may be described as a cavity or hole in the metal surface that is difficult to detect due to its size, and the fact that pits are often imbedded under some corrosion products on the metal surface.

Quantitative examination of pits is often difficult due to different numbers and shapes that pits can adopt under the same environmental conditions.

2.3.1.3 Galvanic Corrosion

Galvanic corrosion occurs when two dissimilar metals are in electrical contact and immersed in a corrosive environment. An electron flow establishes between the two metals promoting corrosion of the less–noble metal (sacrificial anode). In order to maintain electro–neutrality, the electrons released in the oxidation process are consumed in a concurrently occurring reduction process. This flow of electrons occurs due to the difference in standard redox potentials of the two metals in a given aqueous medium, thus making the more noble metal the cathode and the less noble metal the anode. The larger the difference of their standard redox potentials, the greater the corrosion rate. The more noble metal does not oxidize through galvanic corrosion as it is cathodically protected by the less–noble metal. The less–noble metal then corrodes, and for this reason a noble and an active metal should not be joined together directly without an insulator in between. The galvanic series, where the metals are ordered according to their standard redox potentials serves as a guide for metals to be joined in a specific environment. In general, the closer the metals to each other in the galvanic series, the lower the possibility for the corrosion to occur.

2.3.1.4 Selective or De–alloying Corrosion

Selective corrosion was originally known as "parting". Selective or de–alloying corrosion involves the selective removal of the more active alloy component, leaving behind a higher concentration of the nobler one. Examples of this form of corrosion are the removal of zinc from a brass alloy (de–zincification of brass) or removal of aluminum from bronze (de–aluminification of bronze).

2.3.1.5 Erosion Corrosion

In erosion corrosion, the corrosion rate is increased due to rapid movement of a corrosive fluid, or electrolyte along the metal surface, i.e. in pipes and valves. The effect of fluid flow is quit complicated and difficult to predict. In general, smooth surfaces suffer less erosion than rough ones. Erosion corrosion is characterized by the existence of grooves, gullies, waves, or rounded holes, and often exhibits a directional pattern. Erosion corrosion is common place at the inlet of condenser tubes and heat exchangers. Usually, failure as a result of erosion corrosion occurs unexpectedly in a short time due to estimated corrosion tests being performed at static conditions, and the erosion effects not being considered.

2.3.2 Methods of Metal Protection

The consequences of corrosion are different and the effects are often more critical than a loss of equipment, because loss of productivity can be substantial and in some

instances a loss of life can happen. The corrosion rate can be reduced or corrosion can even be prevented by applying an appropriate method of protection that fit a specific corrosive environment. The most common corrosion protection methods are applying a surface coating, and usage of corrosion inhibitors, while other methods are cathodic protection, anodic protection, anodization, and plating, just to mention a few.

2.3.2.1 Applied Coating

The most common corrosion treatment is the application of a protective coating that suits a specific corrosive environment. The protective coat could be plating, enamel or simply a layer of paint to provide a barrier between the metal and the surrounding environment. In the case of plating, if the plating material is more–noble than the substrate, then galvanic corrosion can take place in any exposed area and causes a severe corrosion to the substrate (e.g. chromium on steel). For this reason, it is usually better to plate with a more active material (less–noble) than the substrate itself (e.g. zinc on steel).

2.3.2.2 Corrosion Inhibition

When corrosion inhibitors are added to controlled environment, they form an electrically insulating coat on the surface of a metal to prevent electrochemical reactions from occurring. In a recirculation environment, inhibitors mask the metal surface whenever it is exposed, making the system less–sensitive to defects or scratches. Some of the most common corrosion inhibitors are as follows: hexamine, phenylediamine, sodium

nitrite, condensation products of aldehydes and amines, chromates, phosphates, and others.

2.3.2.3 Cathodic Protection

In cathodic protection, the metal surface is protected by making it a cathode of an electrochemical cell. In other words, the metal does not lose electrons due to oxidation. Therefore, this method can be applied when the structure to be protected is placed in an electrically conducting medium (e.g. sea water, underground structures). Cathodic protection is used to protect steels, ships, offshore oil platforms, fuel pipelines and storage tanks, just to mention a few.

2.3.3 Stability of Metals in Aqueous Environments

Metals and alloys are extensively used to construct objects exposed to aqueous environments, i.e. pipelines, sewer and water distribution systems, ships, valves, etc. They are also used in industrial, marine, urban and agricultural environments, where they encounter water vapor in their surroundings. At times, this water vapor condenses on the metallic surface into a thin liquid film covering the metal surface. They may also be used in harsher environments i.e. petroleum production or boiling water reactors, where they are subjected to high temperature. This aqueous environment could be pure water (no oxygen or solutes), aerated water, or solute–containing waters with or without oxygen. Here we will discuss the corrosion in pure aqueous media, as others are outside the scope

of this research project. In this case, water undergoes self–ionization according to the following equations:

$$2H_2O \longleftrightarrow H_3O^+ + OH^- \qquad (2.2)$$

where H_3O^+ refers to a hydrated proton (free proton, H^+, is unstable in aqueous media). The ionization constant of water is c.a. $K_w = 10^{-14}$ at 25° C. In pure de–aerated water, the only oxidizing agent present in solution is H_3O^+. The relative position of the metal with respect to the hydrogen in the standard potential series determines whether the metal will or will not corrode in the pure de–aerated water. In general, if the proton can attract electrons from a metal, the metal will corrode in this environment and the Gibbs energy of the reduction reaction (ΔG_{red}) of the hydrogen must be more negative than ΔG_{red} of the metal. Since the standard Gibbs energy ($\Delta G°$) for hydrogen equals zero by definition, it follows that H_3O^+ can extract electrons from all metals which have $\Delta G_{red} > 0$. Since $\Delta G° = -nFE^o$, it follows that all metals with standard potential (E^o) values that are lower than that of the H^+/H_2 redox couple are thermodynamically unstable in pure de–aerated water and they will corrode. These metals, with $E^o_{M^{n+}/M} < E^o_{H^+/H_2}$ values, are called active or base metals, i.e. iron, chromium, nickel, zinc, etc. Once the metal oxidizes and forms metal ions (M^{n+}) the latter can react with the OH^- ions or with H_2O molecules to give various solid corrosion products, i.e. metal hydroxides and oxides, which are able to dissolve in the solution or form solid species that can precipitate or adhere to the electrode surface. Conversely, metals with $E^o_{M^{n+}/M} > E^o_{H^+/H_2}$, are thermodynamically stable in pure de–aerated water and are called noble metals, i.e. platinum, palladium,

gold, etc. An example of a corrosion process that occurs in this medium is the rusting of iron; conversion of iron to iron hydroxide as a product occurs according to the following overall equation:

$$4Fe+6H_2O+3O_2 \rightarrow 4Fe(OH)_3 \qquad (2.3).$$

Furthermore, in atmospheric conditions, the iron hydroxide can dry and dehydrate to form reddish–brown rust (ferric oxide, Fe_2O_3) according to the following equation:

$$2Fe(OH)_3 \rightarrow Fe_2O_3+ 3H_2O \qquad (2.4).$$

2.3.4 Metal –Electrolyte Interface

The area of contact between the metal and the electrolyte, two different phases, is of particular importance to interfacial electrochemistry and corrosion. This "phase boundary" is characterized by properties that are greatly different than the properties of either the metal or the electrolyte. It is also the region where the corrosion reaction takes place, i.e. where the metal atoms change their oxidation state, and might become a part of a different phase. Oxidation of the metal creates metal ions, which might dissolve away in an electrolyte or remain within a solid as brittle corrosion products, e.g. oxides, hydroxides, carbonates, etc. on the metal surface undergoing corrosion. Consequently, it is essential to study the structure and properties of the interfacial region between the metal and the aqueous corrosive environment. Aqueous corrosion processes fall within

the domain of electrochemistry. The interfacial region is shown schematically in Fig. 2.9, which depicts vacancies in the metal surface formed through the corrosion of Fe that results in the formation of hydrated Fe^{2+} cations. The electrons released in the process are transferred to a different region of Fe where a reduction process takes place.

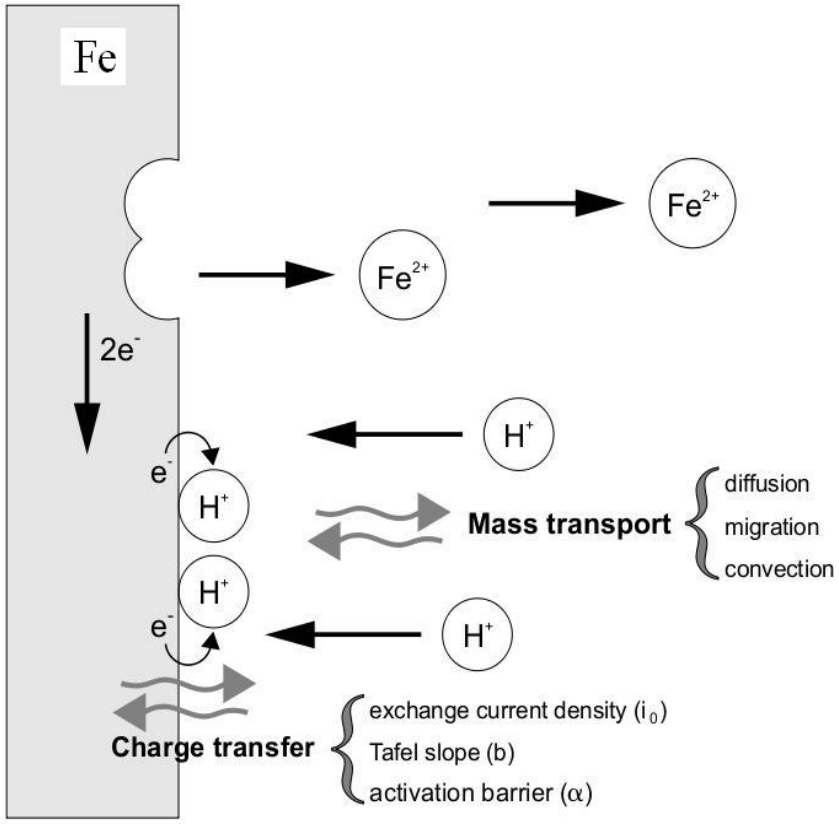

Figure 2.9. Schematic illustration of iron metal–electrolyte interface and the surface processes. The metal atom disengage from the electrode as it loses an electron, while the electron is then transferred to a different region within the electrode surface and participates in a reduction reaction [75].

2.3.5 Electrical Double Layer and Double Layer Capacity

The metal–electrolyte interfacial region is an area that possesses unique properties that differ from those of either phase. The classical model that describes the metal–electrolyte boundary is the simple Helmholtz model, which was introduced in 1853 [76]. In this model, the charged electrode attracts a layer of oppositely charged species to compensate for the charges on the electrode surface; for instance, positive electrode attracts negatively charged species, and vice versa. This simple model is considered to behave like a planar capacitor with molecular dimensions. The separation distance between the two charged layers is the closest approach (i.e. comparable to the diameter of a hydrated cation, c.a. 3 Å) [76]. The ions in the solution are held in their position by purely electrostatic forces and form the outer Helmholtz plane (OHP). The center of the ions that are attached to the electrode surface by a chemical bond then form the inner Helmholtz plane (IHP), see Fig. 2.10. This arrangement of the charges creates a potential difference between the bulk of the metal and the bulk of the solution. In general, the potential changes considerably over a relatively short distance. Another characteristic feature of the electrical double layer is the high capacitance value, in the order of 20 – 100 μF cm^{-2}, which results from the small distance that separate the charges (3 Å) [76]. If a potential difference of 1 V is established across an interface of ca. 1 nm, then the electric field is of the order of ca. 10^9 V m^{-1}.

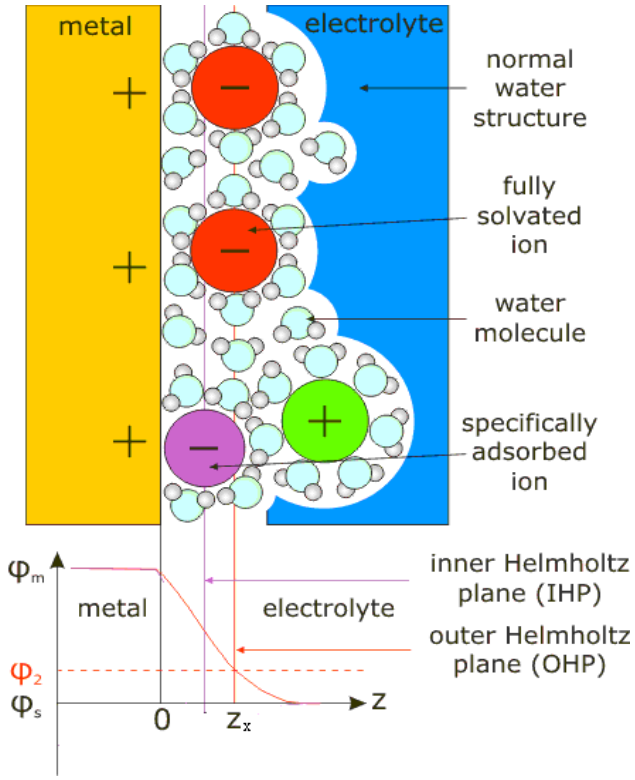

Figure 2.10. Schematic representation of Helmholtz model of the electrical double–layer region [77].

There are many advanced models of the electrical double layer introduced over the years by different scientists, such as the Gouy–Chapman (G–C) model of diffuse double layer, the Stern modification of the G–C model, the Graham's model, etc. Figure 2.11 illustrates the Gouy–Chapman and the Stern models of the electric double layer. Study of the electrical double layer is of importance to not only electrochemistry but also the area of colloids, semiconductors, electro–osmosis, electrophoresis, sedimentation, etc. Measurements of the double–layer capacitance provide one of the most desirable methods of monitoring corrosion and testing the integrity of coatings. The technique that is frequently employed to measure the double–layer capacitance is electrochemical impedance spectroscopy (EIS).

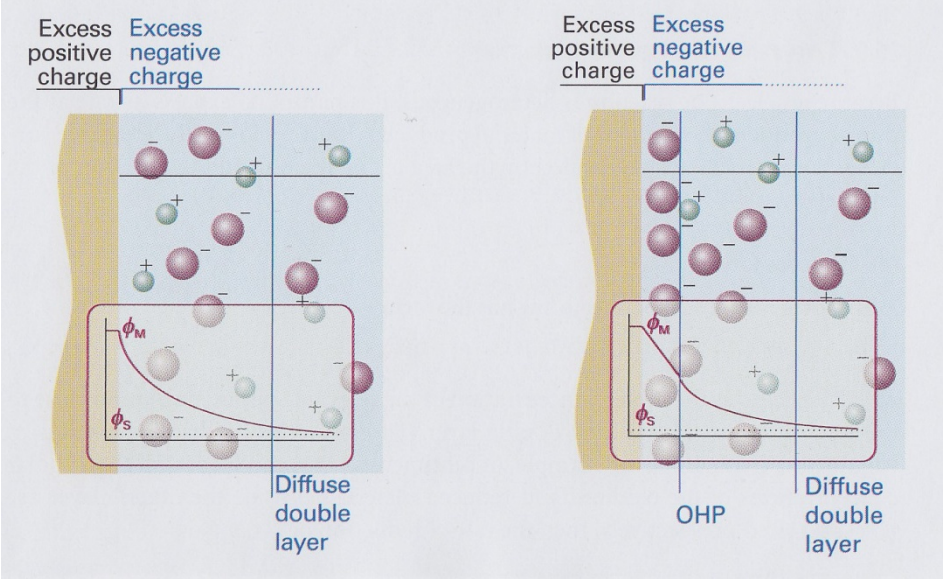

Figure 2.11. Schematic illustration of Gouy–Chapman (left) and Stern (right) models of the double layer [78].

2.3.6 Potential Difference in Electrolyte

Electrode potential is one of the important fundamental concepts of electrochemistry and corrosion science. Corrosion reactions involve at least two redox reactions, i.e. oxidation and reduction, occurring simultaneously on the metal surface. Therefore, to understand the respective electrode reactions and equilibria, the redox reactions must be well understood. When a metal is immersed in an aqueous electrolyte, an electrical double layer is formed at the metal–electrolyte interface as explained in sections 2.3.4 and 2.3.5. The existence of the electrical double layer (charge separation) creates a potential difference between the metal and the electrolyte; consequently the metal has an electric potential ($\emptyset_M$) that is different than that of the solution ($\emptyset_s$). The electric potentials $\emptyset_M$ and $\emptyset_s$ are called the inner potential of a point in the *bulk* of the metal and the electrolyte, respectively. The inner potential of a metal (or any phase) has

two distinct components; an outer potential (Ψ) value, which is the long range columbic interaction near the electrode surface and a surface potential (χ) value, which is determined by the short range effects of adsorbed ions and oriented water molecules. Thus, the inner potential, of a phase, is represented by the following equation [79]:

$$\emptyset = \chi + \Psi \qquad (2.5).$$

The potential difference between the two inner potentials of the metal and the electrolyte ($\emptyset_M$ and $\emptyset_s$) is then called the Galvani potential difference ($\Delta\emptyset$). In the case of a metal, the Galvani potential difference is known as the potential drop across the metal–electrolyte interface. The value of $\Delta\emptyset$ is particular for each specific metal–electrolyte interface and it is represented by the following equation:

$$\Delta\emptyset = \emptyset_M - \emptyset_s \qquad (2.6).$$

The Galvani potential difference, at single metal–electrolyte interface, cannot be measured directly, but the difference between two values of $\Delta\emptyset$ is measurable. In other words, when another metal (M_2) is immersed in the same electrolyte, a new Galvani potential difference will develop ($\Delta\emptyset_2 = \emptyset_{M2} - \emptyset_s$). Then, the difference between $\Delta\emptyset_1$ (for the first test electrode) and $\Delta\emptyset_2$ (for the second electrode) can be experimentally measured. In this case, the Galvani potential difference of the testing electrode is measured with respect to that of the second metal/electrode (the experimentally measured potential = $\Delta\emptyset_1 - \Delta\emptyset_2$). The second electrode is known as a reference electrode, which

has a stable and known Galvani potential value. Examples of some reference electrodes are: standard hydrogen electrode (SHE) that has a potential of 0 V by definition, saturated calomel electrode (SCE), 0.241 V in respect to the SHE, Hg/HgO electrode, 0.140 V in respect to the SHE, etc.

2.3.7 Thermodynamics of Corrosion

From the laws of thermodynamics, the value of Gibbs energy for a system decreases and attains a minimum value as the system reaches the equilibrium. An electrochemical equilibrium can be achieved when no electrons are flowing in or out of the system (open circuit conditions) through an external circuit, and also when only the respective metal ions can be reduced (no oxidizing agent, i.e. O_2 or Cl_2, are present). The presence of another oxidizing agent in the electrolyte that can consume the electrons released from the metal results in net corrosion of the metal. Therefore, the term "equilibrium" implies that the change in Gibbs energy (ΔG) for a system equals zero (G value for oxidation = G value for reduction). For simplicity, consider the following reaction:

$$n_A \mathrm{A}_{(\mathrm{aq})} \rightleftharpoons n_B \mathrm{B}_{(\mathrm{aq})} \tag{2.7}$$

where n_A and n_B are the number of moles of A and B, respectively. The corresponding change in the number of moles is then $\mathrm{d}n_A$ and $\mathrm{d}n_A$ for A and B, respectively. Thus, at

equilibrium, the associated change in Gibbs energy of the system is represented by the following equation [80]:

$$dG_{sys} = \left(\frac{\partial G}{\partial n_B}\right) dn_B + \left(\frac{\partial G}{\partial n_A}\right) dn_A \quad (2.8).$$

If A is converting to B in Eq. 2.7, then the number of moles lost of A participate in forming more moles of B, i.e. $-dn_A = +dn_B$, thus Eq. 2.8 can be rewritten as:

$$dG_{sys} = [\left(\frac{\partial G}{\partial n_B}\right) - \left(\frac{\partial G}{\partial n_A}\right)]dn \quad (2.9).$$

The terms $\left(\frac{\partial G}{\partial n_A}\right)$ and $\left(\frac{\partial G}{\partial n_B}\right)$ are the chemical potentials (μ) of A and B, respectively. Accordingly, the chemical potential for a component in a system is the rate of change of Gibbs energy per mole of this substance, also known as the partial molar Gibbs energy of a substance (at constant T, p and n_j). Equation 2.9 can be rewritten as $dG_{sys} = [\mu_B - \mu_A]dn$ and at equilibrium $\mu_A = \mu_B$. Equation 2.10 relates the concentration of species A and B to their chemical potential:

$$\mu_A = \mu_A^0 + RT\ln[A], \text{ and } \mu_B = \mu_B^0 + RT\ln[B] \quad (2.10)$$

where μ_A^0 and μ_B^0 are the standard chemical potentials of A and B species, [A] and [B] are the concentrations of A and B, respectively. At the metal–electrolyte interface, which involves two phases, one should consider not only the Gibbs energy difference but also

the difference in the electrical energy, since there is a transfer of charged particles. In thermodynamics, the electrochemical potential ($\bar{\mu}$) relates the chemical potential and the electrical energy of a substance according to the following equation:

$$\bar{\mu}_A = \mu_A + z_A F\emptyset \tag{2.11}$$

where z_A is the charge of the substance A. At the electrochemical equilibrium, for instance ($M^{n+}_{(aq)} + ne^- \rightleftharpoons M_{(s)}$), Eq. 2.11 can be applied. As is the case of chemical equilibrium, the total electrochemical potential for the reactants is equal to that of the products, thus Eq. 2.11 gives:

$$(\mu_{M^{n+}} + nF\emptyset_s) = (\mu_M + nF\emptyset_M) \tag{2.12}$$

The concentration of a substance at its standard state (i.e. solid) equals zero, thus rearranging Eq. 2.12 after introducing Eq. 2.10 gives the following Nernst–like equation for this system:

$$\emptyset_M - \emptyset_s = \Delta\emptyset^o - \frac{RT}{nF} \ln[M^{n+}] \tag{2.13}$$

A more general form of Nernst equation is represented in the following equation:

$$E = E^o - \frac{2.3\,RT}{nF} \log \frac{\prod a_{Red}}{\prod a_{Ox}} \tag{2.14}$$

where E^o is the standard electrode potential, i.e. when the activities of both oxidized and reduced species are equal to unity, while Πa_{Ox} and Πa_{Red} are the products of the activities of oxidized and reduced species, respectively. This form of Nernst equation assumes that the solution species are behaving ideally, while in reality the electrolyte species are unlikely to behave ideally. For this reason, it is essential to use the activities rather than the concentrations. Thus, the chemical potential of a substance in non–ideal electrolyte is given by the following equation:

$$\mu_A = \mu_A^o + RT \ln a_A \tag{2.15}$$

where a_A is the activity or the effective concentration of A. The activity is related to the concentration by the activity coefficient (γ) according to the following equation:

$$a_A = \gamma_A \frac{b}{b_o} \tag{2.16}$$

where b_o is the molality of A at the standard state (b_o = 1 mol kg^{-1}). Thus, the standard chemical potential in Eq. 2.15 refers to a hypothetical solution, the molality of which is at the standard state. From Eq. 2.16 it follows that when γ_A is unity then, the activity is equal to b/b_o, and in fact the deviation of γ_A from unity is a measure of the solution's non–ideality. The chemical potential is then given by the following equation:

$$\mu = \mu^o + RT \ln b + RT \ln \gamma = \mu^{ideal} + RT \ln \gamma \tag{2.17}$$

where μ^{ideal} is the chemical potential of the ideal–dilute solution at the same molality of b. Thus, the total molar Gibbs energy (recalling Eq. 2.9, $\mu = \frac{\partial G}{\partial n}$) for a real solution containing univalent cation (M^+) and anion (A^-) with chemical potentials μ^+ and μ^-, respectively is:

$$G_m = \mu_+^{ideal} + \mu_-^{ideal} + RT ln\, \gamma_+ + RT ln\, \gamma_- \quad (2.18a)$$

$$G_m = G_m^{ideal} + RT \ln \gamma_+ \gamma_- \quad (2.18b)$$

where γ_+ and γ_- are the activity coefficients that are the measure of the deviation from ideality of the cation and the anion, respectively. The last term in Eq. 2.18b ($\gamma_+\gamma_-$) indicates that the deviation from ideality is equally shared between the cation and the anion. The value of γ_+ or γ_- cannot be measured experimentally, therefore for 1,1–electrolyte, a mean activity coefficient ($\gamma_\pm$) is introduced. A general form of the molar Gibbs energy for a compound, i.e. M_pX_q (where p and q are the number of moles of the cation M and the anion X, respectively) is represented in the following equation:

$$G_m = p\mu_+ + q\mu_- = G_m^{ideal} + pRT \ln \gamma_+ + qRT \ln \gamma_- \quad (2.19).$$

Introducing the mean activity coefficient ($\gamma_\pm = \sqrt[s]{\gamma_+^p\, \gamma_-^q}$, where $s = p + q$) in Eq. 2.19, the chemical potential of individual ions and the molar Gibbs energy are presented in Eqs. 2.20 and 2.21, respectively.

$$\mu_{\mathrm{i}} = \mu_{\mathrm{i}}^{ideal} + RT \ln \gamma_{\pm} \quad (2.20)$$

$$\mathrm{G}_m = p\mu_+ + q\mu_- \quad (2.21).$$

At equilibrium, when both reactants and products, i.e. O_x and R_{ed}, are separated at different electrodes, one of the most important equations is obtained that describes the electrochemical equilibrium, equation 2.22:

$$\Delta_r G^o = -nFE^o \quad (2.22)$$

where $\Delta_r G^o$ is the standard Gibbs energy change of the reaction, n is the number of the electrons involved in the equilibrium, F is Faraday's constant and E^o is the standard potential of the electrode ($E^o_{M^{n+}/M}$).

2.3.8 Kinetics of Corrosion

The value $\Delta_r G$ for the reduction reactions in a certain environment indicates whether a particular metal will or will not corrode in this environment. The partial reaction with the largest driving force for reduction (i.e. lowest $\Delta_r G$ of reduction) will proceed in the reduction direction (consumes electrons), while the second partial reaction with lower driving force of reduction must then proceed in the oxidation direction and releases electrons. The difference between these two $\Delta_r G$ values determines the thermodynamics driving force for corrosion of the metal (when no other oxidizing agent

is present). If the value of $\Delta_r G$ is negative, then E must have a positive value (see Eq. 2.22), and the reaction will proceed in the reduction direction. Conversely, when the value of $\Delta_r G$ is positive and E is negative, then the reaction will proceed in the oxidation direction. When the equilibrium prevailing at a single electrode is disturbed, the system is said to be polarized. The disturbance may result from a non–open circuit situation, or from oxidizing agents dissolved in the electrolyte. In this case, the electrode potential (E_{irr}) is not equal to the standard electrode potential (E^o) that measured at equilibrium. This difference in potentials of the electrode is called overpotential (η) and the process is referred to as polarization:

$$\eta = E_{irr} - E^o \qquad (2.23).$$

If $\eta > 0$ ($E_{irr} > E^o$), then it is called anodic polarization; the electrode is anodically polarized and the total current (j_{tot}) will be anodic. Conversely, when $\eta < 0$, then the electrode will be cathodically polarized and the net current will be cathodic. As the magnitude of polarization increases, the magnitude of the net/total current increases. The relation between the net current and the overpotential is quantified through the Butler–Volmer equation, which has the following form:

$$j = j_o \left(e^{\frac{(1-\alpha)nF\eta}{RT}} - e^{\frac{-\alpha nF\eta}{RT}} \right) \qquad (2.24)$$

where j_o is the exchange current density (anodic and cathodic currents at equilibrium and the net current is equal to zero), n is the number of electrons transformed, and α is the

transfer coefficient. From this relation, the net current density is the difference between the anodic current density and the cathodic current density. In the case of low overpotential i.e. $\eta << 0$, then $|j_c| >> |j_a|$ and the total current equals $|j_{tot}| = |j_c|$ and vice versa. The Butler–Volmer equation can be rearranged to give a Tafel equation for the anodic process that has the following form [74,81,82]:

$$\eta = \frac{2.3\,RT}{\alpha\, n\, F}\log j_a - \frac{2.3\,RT}{\alpha\, n\, F}\log j_o \qquad (2.25).$$

Figure 2.12 illustrates the Tafel (η vs. log j) relation for a single electrode reaction [83]. The general form of the Tafel relation, which shows the anodic and cathodic reactions of a hydrogen electrode, is represented in Fig. 2.13. This plot is also known as Evan's diagram or polarization curve.

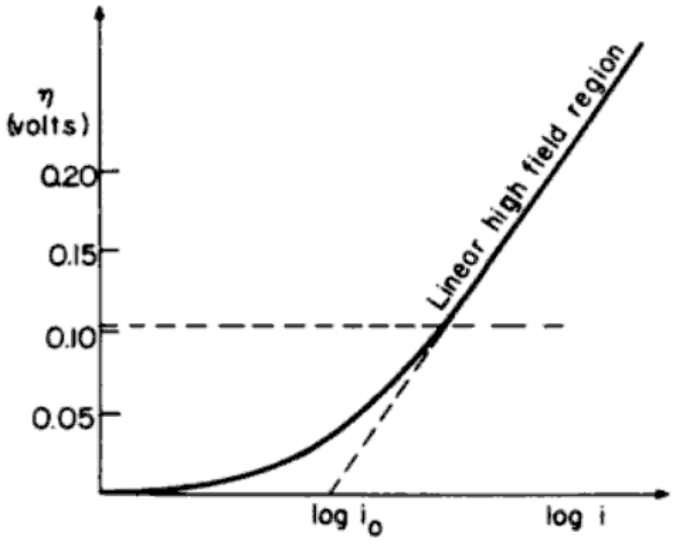

Figure 2.12. Typical Tafel plot for a single electrode reaction [83].

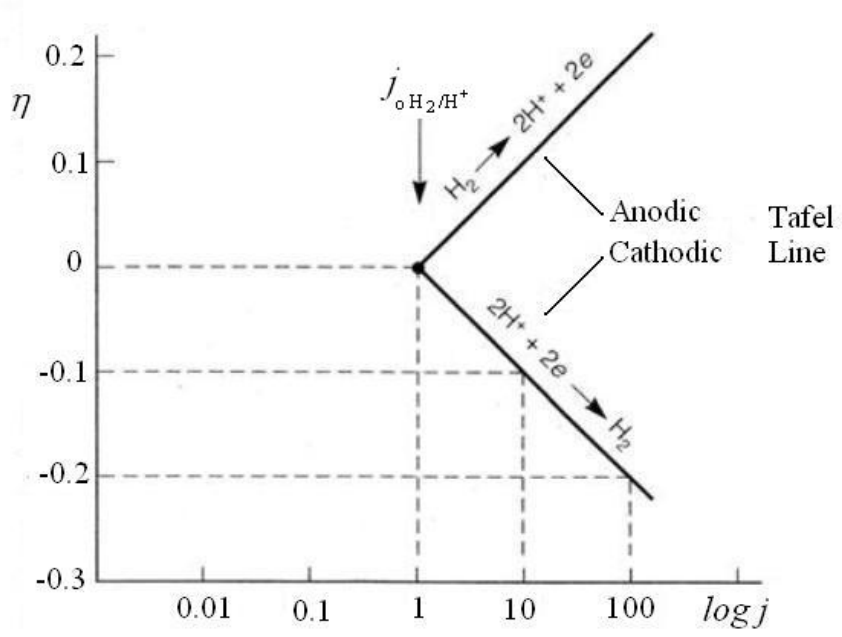

Figure 2.13. Evan's diagram for standard hydrogen electrode illustrates the anodic and cathodic Tafel relation [74].

2.3.9 Catalysis

Catalysis is a very important area in the chemical industry since the production of most industrially important chemicals involves a catalyst. Research into catalysis is a major field in applied science, and involves many fields of chemistry, chemical engineering, material science and physics. Catalysis is define as an increase of the chemical reaction rate through the presence of a catalyst that lowers the Gibbs activation energy of the rate determining step. The catalyst alone cannot make the reaction happen, but it speeds up the thermodynamically favorable reaction. The catalysis process involves the formation of an intermediate, which has lower activation energy than required for the direct reaction without the catalyst. Electrocatalysis is important to electrochemistry since the energy efficiency of any electrochemical cell is determined by the overpotential at the

anode and at the cathode [84,85]. The objective of the electrocatalysis is to provide a lower energy of activation pathway and to permit the electrode reaction to occur at high current density and at a low overpotential. In this case, the metal electrode surface acts as a reaction site to provide or accept electrons. The overpotential for each current density is given by the Tafel equation. Rearrangement of equation 2.25 gives:

$$\eta = \frac{2.3\,RT}{\alpha\, n\, F}\,[\log j - \log j_o] \qquad (2.26).$$

The catalysis speeds up the reaction rate via homogeneous or heterogeneous processes. In homogeneous catalysis both, the catalyst and the reagents are dissolved in the same phase, while in heterogeneous catalysis the catalyst and the reagents are in two different phases (i.e. metal/adsorbed species or ions).

2.3.10 Mixed Potential

In a corroding system, the overall corrosion reaction involves two (or more) electrochemical redox reactions. Each electrochemical reaction has its own polarization curve. Plotting each polarization curve on the same current and potential coordinates forms an Evan's diagram for this system. In general, a metal will corrode when its anodic partial reaction (i.e. $M \rightarrow M^{z+} + ne^-$) intersects with the cathodic partial reaction of other electrode (i.e. $2H^+ + 2e^- \rightarrow H_2$), and vice versa. Figure 2.14 shows a corroding system of zinc ($E^o_{Zn^{2+}/Zn} = -0.763$ V) in presence of hydrogen. The anodic Tafel line of the metal intersects with the cathodic Tafel line of the hydrogen, which leads to produce metal ions.

Intersection of the two Tafel lines determines the condition of general corrosion, j_{corr} and E_{corr}, which falls between the two standard potentials [74]. In corrosion science, the potential arising from two electrochemical potentials is called a 'mixed potential' (E_{mix}). Usually, the two reactions contributing to E_{corr} are the metal oxidation (anodic process) and the hydrogen evolution or the oxygen reduction when the corrosion proceeds in oxygen containing solutions.

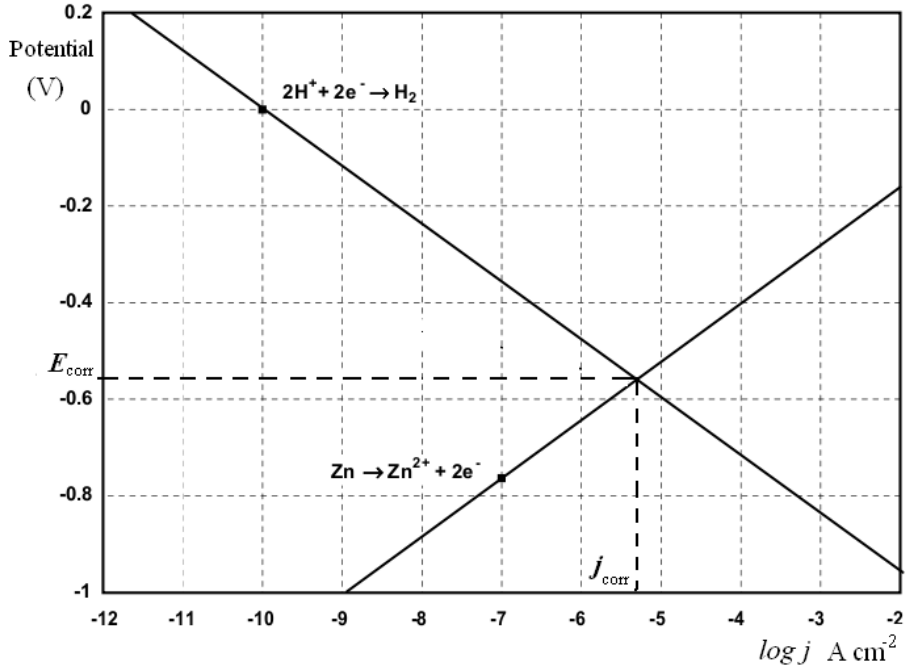

Figure 2.14. Polarization of anodic and cathodic half–cell reactions of a corroding system consisting of zinc in acid solution, giving a mixed potential, E_{corr} and corrosion rate, j_{corr} [74].

In order to measure the polarization (j vs. E) curve of a certain electrode, one must use a polarization cell which is composed of three electrodes; working electrode, counter/auxiliary electrode and a reference electrode, see Fig. 2.15. The ammeter

measures the current flowing between the working and the counter electrodes, while the high input voltmeter measures the potential of the working electrode against the reference electrode. When current flows between the counter and the working electrodes, the equilibrium at the working electrode is disturbed and hence its potential shifts away from the equilibrium value. Then, this value of the overpotential is measured against the reference electrode using a voltmeter.

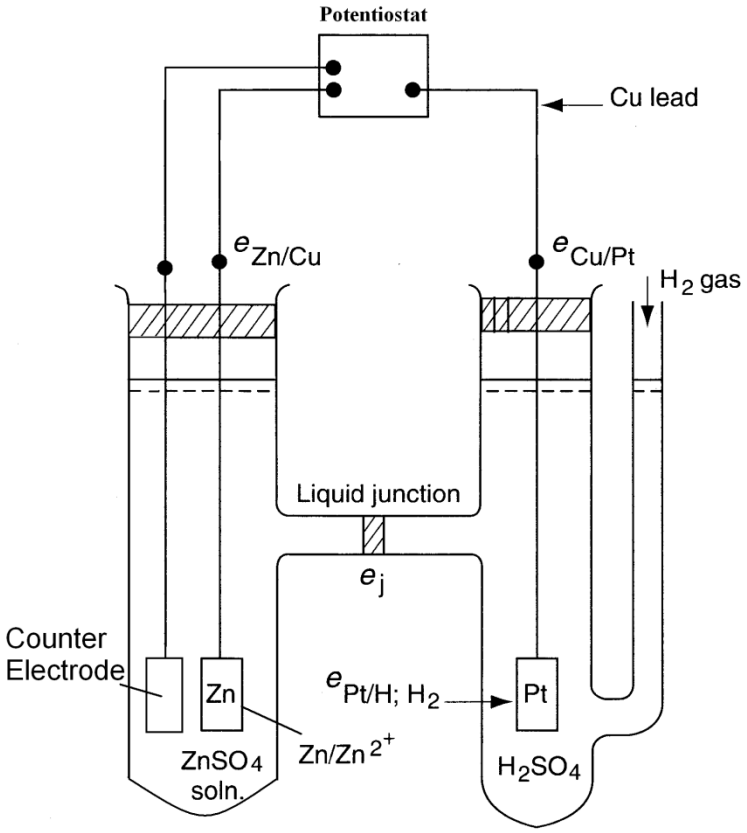

Figure 2.15. Schematic diagram for the standard three compartment electrochemical cell [74].

2.3.11 Passivation

Passivity of metals and alloys is a very important phenomenon in the field of corrosion and protection of metals. It describes the state of an active metal surface when its rate of corrosion is lower than expected at a specific potential value positive to E_{corr}. Passivity is attributed to the formation of a thin film (less than a micrometer) which adheres onto the metal surface spontaneously, thereby protecting it from further oxidation (corrosion) at specific conditions [86,87]. This phenomenon explains the remarkable stability of many active metals and alloys in various environments where they are expected to corrode, in view of thermodynamic considerations. This is the case for stainless steels, aluminum, nickel, chromium, and super alloys in aqueous environments. Although the standard potential values for those metals are negative in relative with that for the hydrogen electrode, their corrosion rates in the passive region are very low. They are said to be in passive condition, i.e. their surfaces are passivated, and thus they do not corrode to any measurable extent. For example, aluminum metal has $E^{o}_{Al^{3+}/Al} = -1.66\ \text{V}$ (SHE) which represents an enormous driving force for corrosion as its ΔG_{red} has a large positive value, however, Al does not corrode in water to any measurable extent due to the formation of a passive layer. In Fig. 2.16, we show a typical polarization curve of a metal that demonstrates the active, passive and transpassive regions. The passive region is characterized by a drop in the current density value (a few orders of magnitude). The width (potential range) of the passive region varies from one metal to another, and it is also affected by the medium.

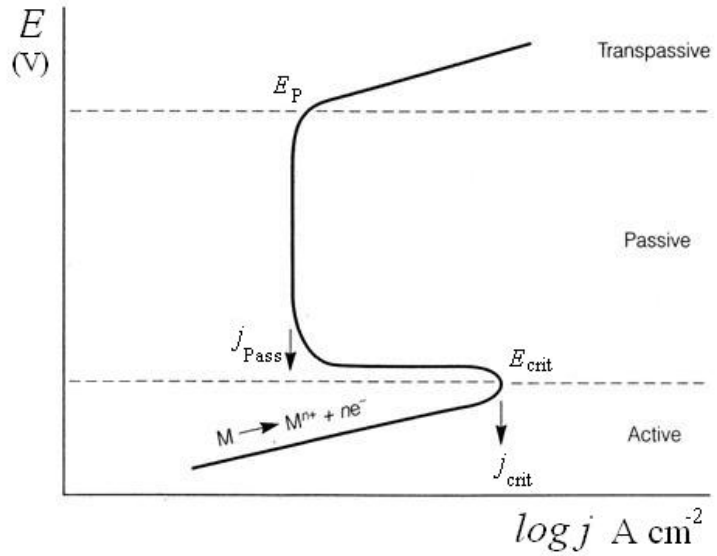

Figure 2.16. Schematic representation of a polarization curve of a metal showing the active–passive region [74].

In Fig. 2.16, the E_{crit} is called the critical potential or the flade potential at which the current drops. Once the potential of the metal reaches this value, the surface of the metal becomes passivated. The passive current density (j_{pass}) represents the corrosion rate of the passive surface. This value may be some orders of magnitude lower than the anodic dissolution current density, just before the potential reaches E_{crit}. The point at which the current starts to increase above the passive value (E_{pass}) indicates the beginning of the transpassive region. Some factors that inhibit passivation are: very high/low pH, presence of chloride ions, high temperature, or fluoride ions. The passive range, as well as the values of E_{crit}, j_{pass} and E_{pass} depends on the composition of the electrolyte and the nature of the metal. In general, as the concentration of i.e. Cl^- (or other halides or H^+) ions increases, the width of passive region decreases (E_{crit} increases and E_{pass} decreases), and the passive current increases. These changes indicate that the passive layer becomes

less protective. Thus, a more positive potential than E_{crit} must be applied to form the passive film. At high concentrations of Cl^- or other corrosion–causing ions, the passive region could disappear entirely.

2.3.12 *Pourbaix Diagram*

The value of the electrode potential (E), in a certain environment, indicates whether this metal will or will not corrode in this medium. The E–pH relation is known as "Pourbaix diagram" that demonstrates graphically the various thermodynamic stable metal phases (i.e. metal ions, oxides, hydroxides and any other species that can combine the oxides). The Pourbaix diagram provides useful information for corrosion science and technology as it demonstrates the stable phases. A disadvantage of Pourbaix diagrams is their lack of the kinetics; the rate of the corrosion cannot be predicted based on these diagrams. Figure 2.17 illustrates the Pourbaix diagram for Ni electrode in water at 25^o C [88]. The regions where the Ni, $Ni(OH)_2$ and Ni oxides are stable can be determined from Pourbaix diagram. It is important to remember that the presence of ions such as chloride, citrate, cyanide, etc. can affect (expand) the corrosion area in Pourbaix diagram.

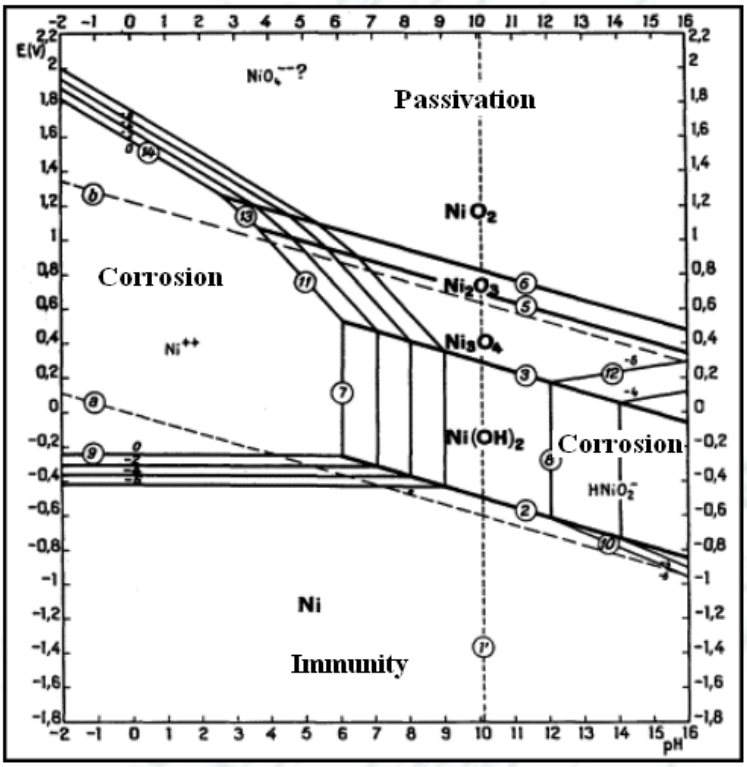

Figure 2.17. Pourbaix (*E* vs. pH) diagram for Ni in water at 25^{o} C [88].

2.4 Metal Oxide Characterization Methods

The electrochemical methods used in this study are cyclic voltammetry (CV) and chronoamperometry (CA). Also, an ex–situ surface science technique such as X–ray photoelectron spectroscopy (XPS) coupled with Ar^{+} depth profiling is used to characterize the metal surface. To understand the basics of these electrochemical and surface science techniques, it is important to explain the process by which the electroactive species transports towards/away from the electrode surface. Mainly, there are three physical mechanisms that govern the movement of the electroactive species from/to the bulk of the solution to/from the electrode surface: migration, convection, and

diffusion. In these mechanisms, the movement of the species is influenced by an electric field gradient, a pressure gradient, and a concentration gradient, respectively. An attempt is made to minimize the effect of the former two processes, due to the difficulty to make an accurate treatment, so that the mass transport is influenced only by the diffusion. The migration process can be minimized by the addition of the supporting electrolyte of high concentration, while the convection process can be minimized by agitation of the solution (e.g. by gas bubbling inside the electrolyte) or mechanical stirring. As the redox reactions proceed on the electrode surface, the diffusion layer adjacent to the electrode grows to a limiting thickness with time (e.g. 10^{-6} – 10^{-4} m depending on the electrolyte concentration), after that the charges distribute uniformly.

2.4.1 Cyclic Voltammetry

The intention of employing controlled–potential experiments is to attain a current response that is related to the transfer of electron(s) during the redox couple. The resulting current of the redox reaction is known as Faradic–current and the consequential current–potential relation is known as a voltammogram. The voltammetric current corresponds to the Faradic–current, as well as the non–Faradic current due to double layer charging. Cyclic voltammetry (CV) is one of the most important electroanalytical techniques due to its ability to provide qualitative kinetic and thermodynamic data for a given system. It allows one to obtain both qualitative information, such as reversibility of the system or the mechanism of the process, as well as quantitative data, such as the amount of oxide formed (charge transferred). The CV is based on the linear potential

sweep voltammetry (LSV) in which the direction of the potential scan is reversed at the final potential (E_f) and the potential range is scanned again in the reverse direction back to the initial potential (E_i) at time τ. The exact shape of the CV profile in many cases is very characteristic for a specific element, thus it can be treated as its "electrochemical fingerprint". In some cases, the potential can be scanned past the final potential to a second final potential, and then the direction of the potential scan is again reversed. In this technique, the electrode current is monitored as a function of the applied potential (j – E relation is obtained). Figure 2.18 illustrates a cyclic voltammetry program used to form and to characterize a surface oxide in this study and Fig. 2.19 shows a typical CV for a reversible system.

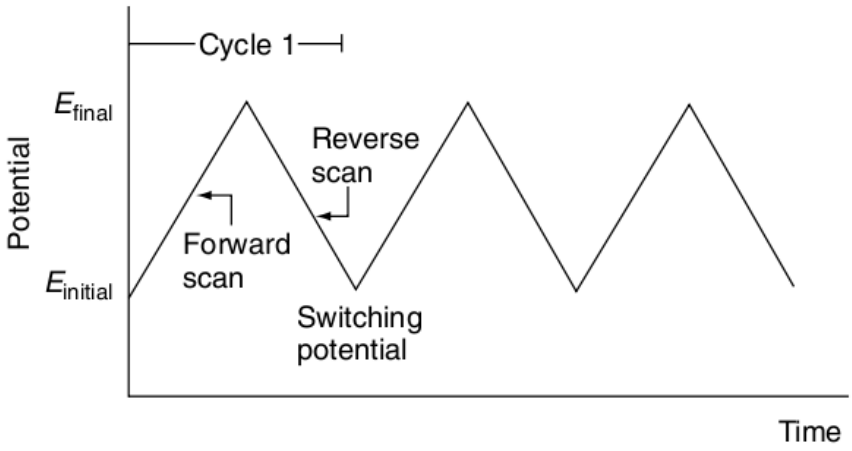

Figure 2.18. Potential program used in cyclic voltammetry. Initial potential (E_i), and final potential (E_f), are adjusted for different systems [89].

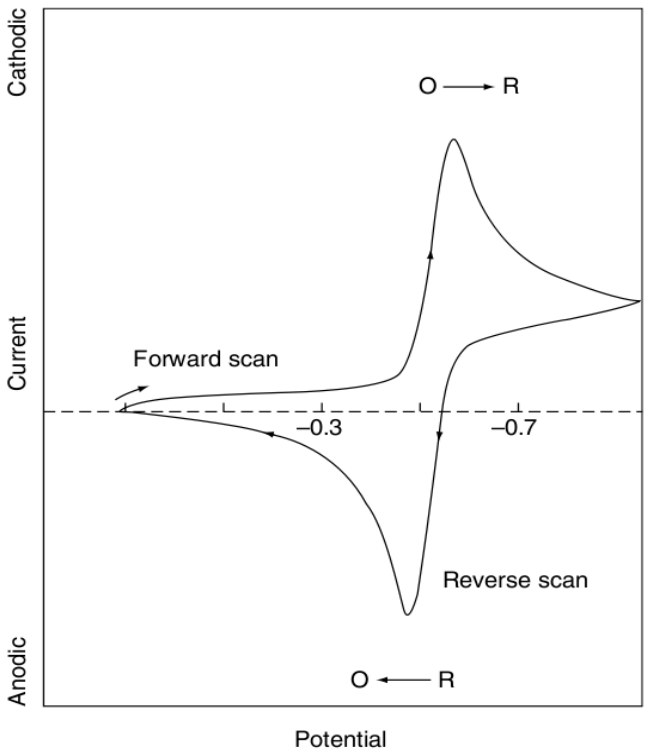

Figure 2.19. Typical CV profile recorded for a reversible system [89].

In its most basic case, CV is used to study a redox couple system, with both species (oxidized and reduced) present in the solution and transported from/into the bulk of the solution by infinite planar diffusion. During the forward potential scan, a current will flow between the electrode and the solution species as the potential approaches a value equivalent to the oxidation potential of the investigated species. The current will increase as a result of a charge transfer and then falls down as the concentration of the investigated species decreases in the vicinity of the electrode surface. Subsequently, the solution species to be oxidized must now transport from the bulk of the solution to the electrode surface by diffusion. The increase in the current and the subsequent decrease develops an anodic current peak in the corresponding CV profile. In the backward

potential scan, when the potential reaches a value corresponding to the reduction of the species previously formed in the anodic scan, a cathodic current peak arises at opposite polarity of the anodic one. In order to elucidate the current behavior, first we need to consider the following process: $O_x + ne^- \rightleftharpoons R_{ed}$ and there are no other solution species which consumes the electrons. A state of equilibrium establishes at the electrode surface which can be described by Nernst equation when the rate of electron transfer is fast in comparison to the potential scan rate. As the potential is scanned, the current will flow and the equilibrium is adjusted accordingly. The current will increase with the progress in the potential scan as a result of converting more reactant to product species. At this point, a concentration gradient develops between the electrode surface and the bulk of the solution which forms the diffusion layer. The thickness of the diffusion layer will increase (the diffusion layer will grow away from the electrode surface) when the concentration of the reactant is further decreases. The current peak in the corresponding CV profile develops when the diffusion layer grows sufficiently away from the electrode surface and the flux from the solution to the electrode is not fast enough to satisfy Nernst equation. In this case, the current starts to fall down as the species to be oxidized must diffuse from the bulk of the solution. This drop in the current follows Cottrell equation that depicts the change in the current as a function of the concentration of the electroactive species and the time of the potential scan.

The shape of the CV profile depends on the electrochemical reversibility of the process (different profile for reversible process than irreversible one). For a reversible

process, i.e. when the rate of electron transfer is faster than the rate of mass transfer, the peak current density (j_p) can be described by Randles – Sevcik equation [82]:

$$j_p = (2.69 \times 10^5)\, n^{3/2} C_{ox}^{\infty} D_{ox}^{1/2} v^{1/2} \quad (2.26)$$

where j_p is the current density in A cm^{-2}, n is the number of the electrons transferred in the reaction, C_{ox}^{∞} is the concentration of the electroactive species in the solution bulk in mol cm^{-3}, D_{ox} is the diffusion coefficient in cm^2 s^{-1}, and v is the scan rate in V s^{-1}. The constant (2.69×10^5) originates from Faraday's constant (F), the gas constant (R), and other integration constants. From Randles–Sevcik equation, it follows that the current is directly proportional to concentration of the electroactive species and increases with the square root of the scan rate. In the case of a simple reversible redox couple, the ratio of the peak current for the anodic and cathodic processes is equal to unity, i.e. $\left|j_p^A / j_p^C\right| = 1$. Furthermore, the potential of the reversible redox couple (the standard potential) is located in between the two peaks, as follows:

$$E^o = \frac{E_{\text{p(anodic)}} + E_{\text{p(cathodic)}}}{2} \quad (2.27).$$

The peak potential for the anodic and cathodic peaks are independent on the scan rate, see Fig. 2.20a. In addition, the separation between the two peak potentials is described by the following equation that can also be used to determine the number of electrons transferred:

$$\Delta E_{\mathrm{p}} = E_{\mathrm{p(anodic)}} - E_{\mathrm{p(cathodic)}} = \frac{0.059}{n}\ \mathrm{V} \qquad (2.28).$$

The time required to record a CV profile is directly related to the potential scan rate and strongly affects the shape of the CV profile at constant E_{i} and E_{f} values. This is due the fact that the thickness of the diffusion layer at the electrode surface depends on the scan rate and consequently the time needed to record the CV profile. For low scan rates, the time needed to record the CV profile is longer, thus the diffusion layer will grow much further from the electrode surface in comparison to the high scan rates. Accordingly, as the current is proportional to the flux of the electroactive species towards the electrode, the magnitude of the current will be lower at slow scan rate than that for the fast scan rates, Fig 2.20a. Additionally, the position of the current maximum is the same for different scan rates and this is a characteristic of electrode reaction with rapid electron transfer kinetics which is referred to as reversible electron transfer process.

In the case of irreversible system, the electron transfer process is slower than the potential sweep rate and the peak potential is shifted as a function of scan rate (see Fig. 2.20b). The applied potential will not lead to a concentration gradient between the electrode surface and the bulk of the solution. This is due to the fact that the reaction kinetics are slow and the potential does not reflect the equilibrium of the redox couple. Furthermore, the position of the current maximum is shifted as a result of the slow response of the current versus the applied potential. The peak current density (j_{p}), for an irreversible system, is described by the following equation:

$$j_p = -(2.99 \times 10^5)\, n\, (\beta\, n_\alpha)^{1/2}\, C_{ox}^{\infty}\, D_{ox}^{1/2}\, v^{1/2} \qquad (2.29)$$

where n_α is the number of electron transferred up to the rate determining step, and β is a symmetry factor (other parameters are the same as in Eq. 2.26). Table 2.1 lists some parameters and features of the CV profiles for the reversible and the irreversible systems [82]. It must be stressed that the terms presented in Table 2.1 are applicable when the oxidized and reduced species are present in the solution. The E_p and j_p parameters make the cyclic voltammetry suitable for characterization and mechanistic studies for redox reaction at the electrode surface.

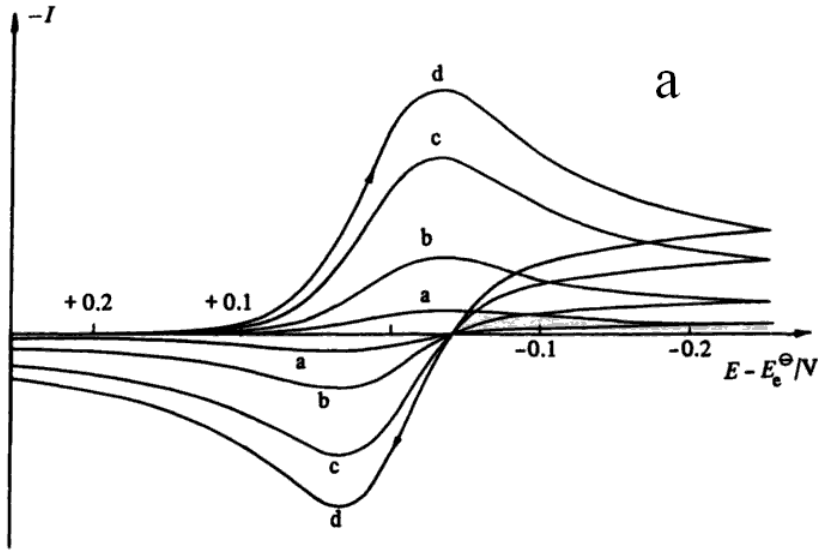

Figure 2.20a. Series of CV profiles recorded at different scan rates (v) when only O is initially present in solution for a reversible system [82].

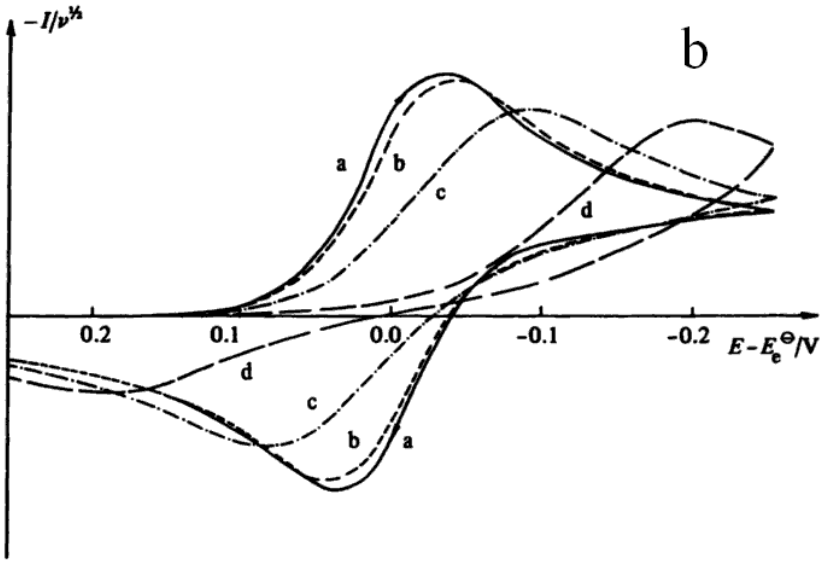

Figure 2.20b. Series of CV profiles recorded for irreversible systems at different scan rates (v) when only O is initially present in solution [82].

Table 2.1: List of the cyclic voltammogram's parameters for reversible and irreversible process at T = 298 K [82].

Reversible processes	**Irreversible processes**
$\Delta E_p = E_p^A - E_p^C = 59/n$ (mV)	$\left\|E_p - E_{p/2}\right\| = \frac{48}{\alpha_c n_\alpha mV}$
$\left\|j_p^A/j_p^C\right\| = 1$	E_p^c shifts $30/\alpha_c n_\alpha$ mV for each decade increase in v
$j_p \propto v^{1/2}$	$j_p \propto v^{1/2}$
E_p is independent of v	

2.4.1.1 Cyclic Voltammetry for Surface Process

The cyclic voltammetry experiment is also applied to study the interfacial behavior of electroactive species which confined to the immediate vicinity of the electrode surface (i.e. adsorption forces or covalent bonds). In this case, no concentration gradient develops and the process is limited to the species attached to the electrode. The shape of the CV profile is different in this instance than for the case of thin films. In addition, the peak current is directly proportional to the surface coverage (Γ_o) and the scan rates (not the square root of the scan rate). The current–potential CV profile for adsorbed oxidized (O) species is given by the following equation [89]:

$$j_p = \frac{n^2 F^2 A\, v\, \Gamma_o}{4\, R\, T} \tag{2.30}$$

where Γ_o is the surface concentration (before the experiment), n is number of electrons, F is Faraday constant, A is the surface area and v is the potential scan rate. The CV profile is characteristic by symmetric anodic and cathodic peaks with peak separation (ΔE_p) equals zero. The anodic or cathodic peak half–width is 90.6/n mV, see Fig. 2.21. The surface coverage or the area occupied by the adsorbed species can be determined using the charge density which obtained from the integration of the CV peak according to the following equation [89]:

$$q = nFA\Gamma_o \tag{2.31}.$$

An adsorption isotherm (for example Langmuir isotherm) is usually used to relate the surface coverage to the bulk concentration (C) of the solution, see the following equation [89]:

$$\Gamma_o = \Gamma_m \frac{D_{ads}\, C}{1+ D_{ads}\, C} \tag{2.32}$$

where Γ_m is the surface concentration of one monolayer coverage and D_{ads} is the adsorption coefficient. The Langmuirian isotherm is applicable for sub–monolayer coverage with the assumption of no interactions exists between the adsorbed species on the surface. Such interaction is considered in different isotherms (i.e. Temkin or Frumkin isotherm).

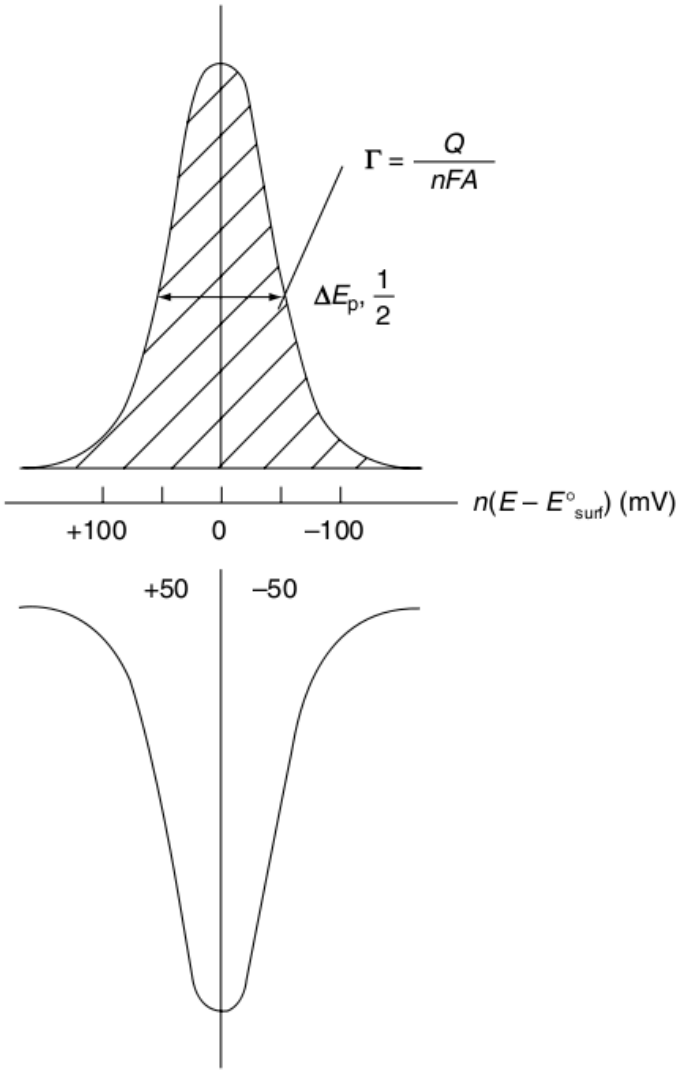

Figure 2.21. Typical cyclic voltamogram for a surface layer on an electrode [89].

2.4.2 Chronoamperometry

Chronoamperometry (CA) is one of the most important potential step techniques in electroanalytical chemistry. The potential of the working electrode is held and the current response is monitored as a function of time. The time scale in this technique is usually in milliseconds up to seconds, while in other potential step techniques, such as

constant potential electrolysis (CPE) and DC potential amperometry (DCA), the time scale extends from seconds up to minutes or hours. The simplest case of this technique is single potential step chronoamperometry. In this case, the potential of the working electrode is changed instantaneously from E_1 (for a short time) where there is no electrode reaction occurring, to E_2, where one is occurring, for example the reduction of O_x species. The E_2 is held for a specific time (Fig. 2.22). The theory of the diffusion process depends upon the geometric characteristics of the electrode and the surrounding solution; the two extreme geometric cases are planar electrode and spherical electrode. For planar electrodes, the diffusion can occur only in one direction (linear diffusion), while for spherical electrodes the diffusion can occur in all directions (spherically symmetrical diffusion). A test for diffusion control is the plotting of j vs. $t^{-1/2}$, which should be linear and passes through the ($j = 0$, $t = 0$) point. The diffusion coefficient of species O_x can then be calculated from the slope of the $j - t^{-1/2}$ relation. Furthermore, the scan rate can also be used in place of time in the form of $v^{1/2}$; typical scan rates are in the range of 10 up to 2000 mV s^{-1}. The theoretical relation between current and time for linear diffusion was derived by solving the Fick's 2nd law of diffusion for a planar electrode, and it is presented by the Cottrell equation, which describes the change in electric current with respect to time [82]:

$$|j_c| = \frac{n\,F\,A\,D_o^{1/2}C_o^{\infty}}{\pi^{1/2}t^{1/2}} \tag{2.33}$$

where n is the number of electrons transferred in the reaction, F is the Faraday's constant in C mol^{-1}, A is the area of the electrode in m^2, D_o is the diffusion concoefficient in m^2 s^{-}

[1], and C_o^∞ is the concentration of the diffusion species in mol cm^{-3} in the bulk of the electrolyte solution. Deviation from linearity in the plot of j vs. $t^{-1/2}$ sometimes indicates that the redox process is associated with other processes, such as association of a ligand, dissociation of a ligand, or a change in the geometry where the species are diffusing (i.e. at the surface).

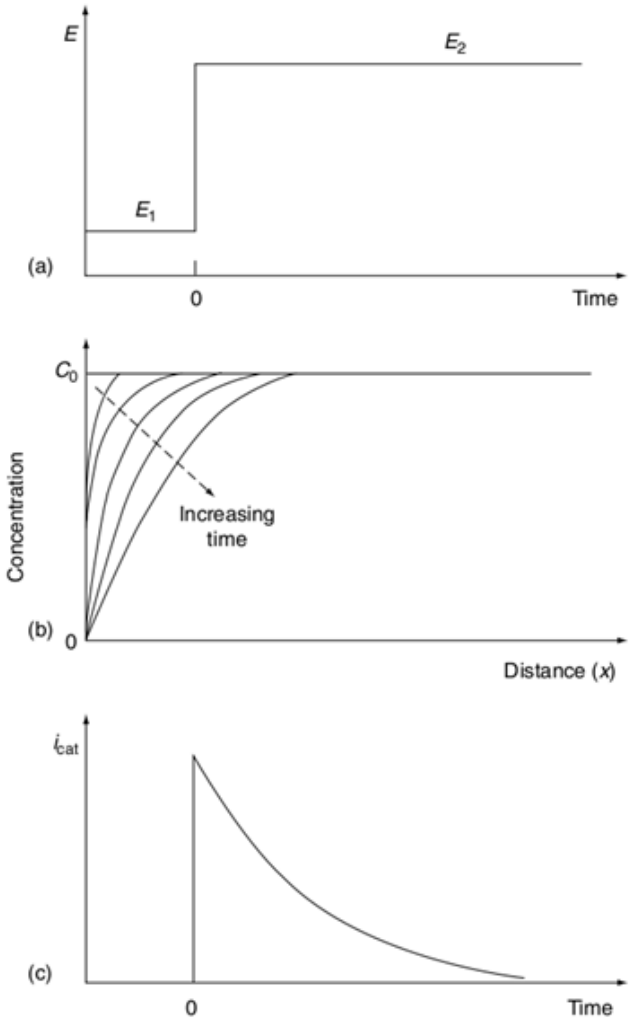

Figure 2.22. Typical CA curves showing (a) potential–time relation, (b) changes in the concentration of the diffusing species in the vicinity of the electrode surface, and (c) the corresponding current–time relation [89].

Chronoamperometry can also be applied as a double–potential step. In this case, the single potential step is followed by another potential step at which the reduced species are reoxidized at time τ. Thus, for $t > \tau$ the anodic current follows the equation:

$$|j_a| = \frac{n\,F\,A\,D_o^{1/2}C_o^{\infty}}{\pi^{1/2}}\left[\frac{1}{(t-\tau)^{1/2}} - \frac{1}{t^{1/2}}\right] \qquad (2.34)$$

Another advantage of chronoamperometry is that the recorded current during the experiment, can be converted to charge and plotted as a function of time, Q vs. t. This technique is called chronocoulometry (CC). The chronoamperometry allows one to investigate the diffusion–controlled process, such as nucleation and growth that cannot be analyzed by application of CV. An important advantage of CA as compared to CV is that, in the case of cyclic voltammetry the double layer (non–Faradic) charging currents must be subtracted from the recorded currents during a potential scan, while in the case of CA as long as the electrode surface is not changed significantly with time, double layer current corrections are only necessary immediately after the potential change.

2.4.3 X–ray Photoelectron Spectroscopy (*XPS*) *and Depth Profiling*

X–ray photoelectron spectroscopy (XPS), also known as electron spectroscopy for chemical analysis (ESCA), is a surface analysis technique that is unique in providing quantitative information of the composition and electronic state of the elements being analyzed. XPS is used to characterize the surface of different material, such as metals, alloys, semiconductors, polymers, glasses, and others. In this technique, a monochromatic

beam of X–rays (usually a value between 200 – 2000 eV) is used to irradiate a sample. The most commonly used X–ray sources are Mg and Al (Mg Kα radiation; hν = 1253.6 eV is used in this study). The absorbed photon excites a core electron from an atom in the sample resulting in its ionization. The overall process of photoionization and the corresponding energies are as follows:

$$\mathrm{A} + h\nu \rightarrow \mathrm{A}^{+} + e^{-} \tag{2.35}$$

$$E_{(A)} + h\nu = E_{(A^{+})} + E_{(e^{-})} \tag{2.36}$$

where h is the Plank constant (6.62 x 10^{-34} J s) and ν is the frequency of the radiation in s^{-1}. The term $E_{(A^{+})} - E_{(A)}$ represents the difference in energies between the ionized and neutral atom, which is called the binding energy (BE). The kinetic energy (KE) of the photoelectron is represented by the electron's energy $E_{(e^{-})}$. Thus, rearrangement of Eq. 2.36 gives:

$$\mathrm{KE} = h\nu - \mathrm{BE} \tag{2.37}$$

The BE is accepted to be a direct measure of the energy required to excite an electron from the core level to the vacuum level in the analyzed sample. This process is described schematically in Fig. 2.23, bearing in mind that for solids, the binding energy is measured with respect to the Fermi level (E_{F}) rather than the vacuum level (E_{v}). Thus, the work

function (∅) of the solid should be included in Eq. 2.37, and the equation describing this process is given by the following equation:

$$KE = h\nu - BE - \emptyset \tag{2.38}$$

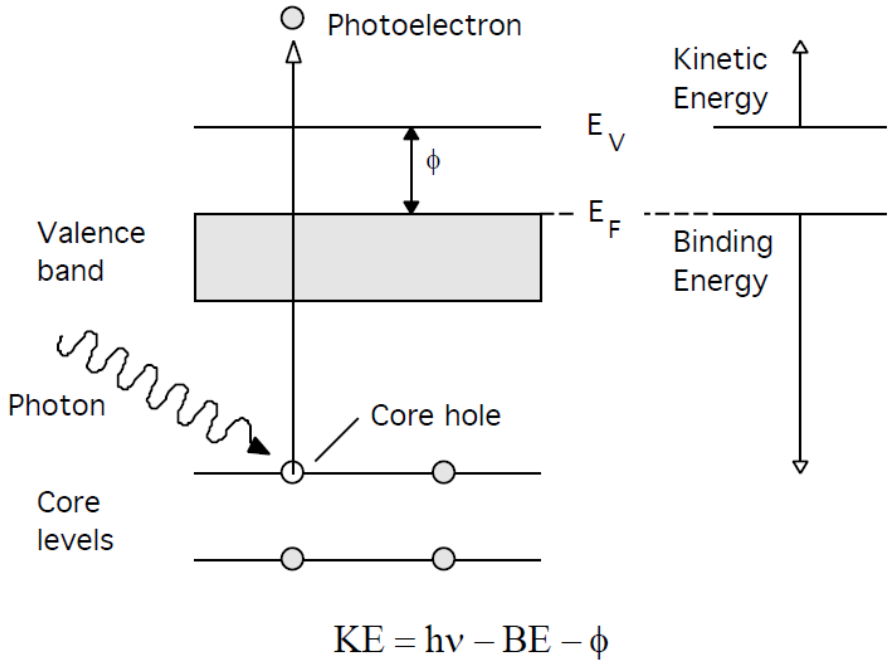

Figure 2.23. Schematic diagram of photoelectron ejection in XPS.

The BE associated with each core atomic level is characteristic for each element. For instance, each element gives rise to a set of peaks in the photoelectron spectrum at a specific kinetic (or binding) energy. Therefore, the presence of these peaks at particular KE or BE indicates the presence of a specific element in the sample. Emission of

photoelectrons from some atomic levels gives rise to two peaks in the corresponding XPS spectrum, rather than a single peak. These two peaks are slightly separated from each other, with respect to their binding energy. This effect arises from spin–orbit coupling between the magnetic fields of spin (s) and the angular quantum number (ℓ). The total angular momentum (j_m) of a particle is then a function of ℓ and s ($j_m = \ell \pm s$). The maximum value of the angular quantum number is equal to ℓ = n – 1 (where n is the principal quantum number, n = 1, 2, 3, etc.), while s has the value of ± ½. If we consider a palladium atom, for instance, the photoelectron will be emitted from the core level, n = 3. In the XPS spectrum for Pd, see Fig. 2.24, the most intense peak is due to the emission from 3d level. By applying the spin–orbit coupling theory, the values of the total angular momentum are 5/2 and 3/2, which results in doublet peaks ($3d_{5/2}$ and $3d_{3/2}$) in the corresponding XPS spectrum. The lowest energy peak is the one with maximum j_m, the $3d_{5/2}$ peak (as the orbital is more than half–full), and it appears at a lower binding energy in the XPS spectrum than the other peak ($3d_{3/2}$). Figure 2.25 shows XPS spectrum (in the region of Pd 3d peaks) that illustrates the splitting of the 3d peaks.

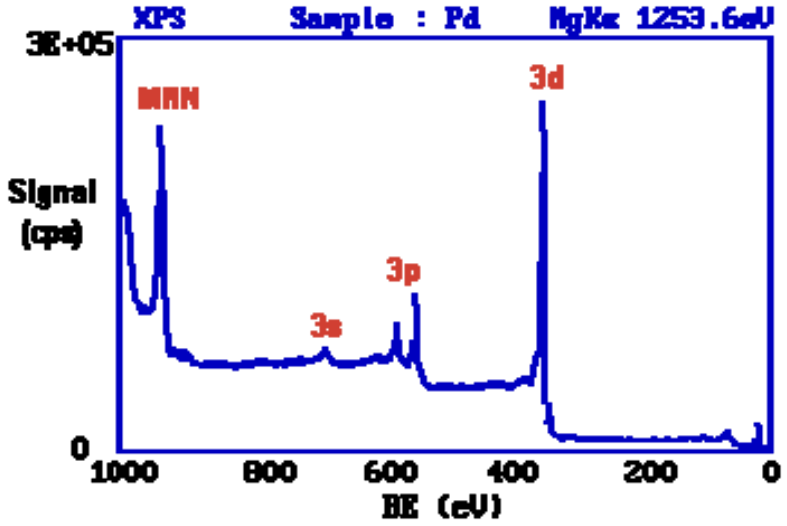

Figure 2.24. XPS survey spectrum for Pd electrode [90].

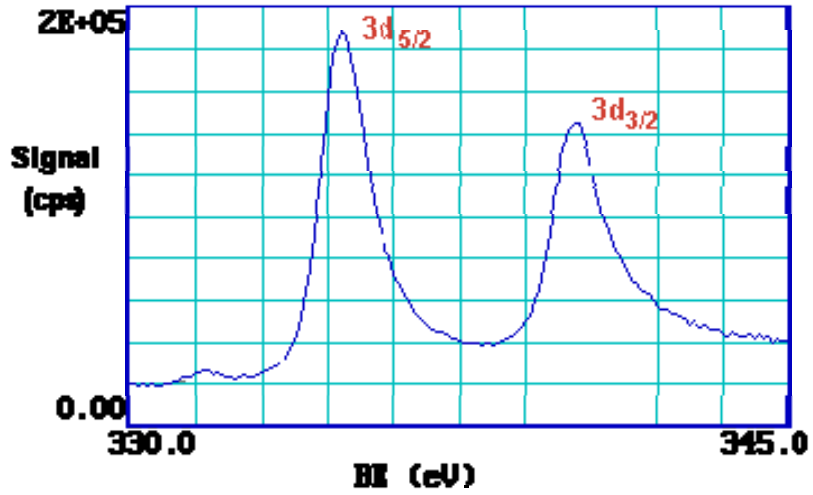

Figure 2.25. High resolution XPS spectrum for Pd electrode showing only the 3d peaks [90].

The ratio of the intensities of the two 3d peaks can be determined from the following equation:

$$\mathrm{D} = 2\, j_m + 1 \tag{2.39}$$

thus, for d orbital, the intensity of the two peaks is equal to:

$$\mathrm{D} = 2 \times \left(\frac{3}{2}\right) + 1 = 4 \qquad and \qquad \mathrm{D} = 2 \times \left(\frac{5}{2}\right) + 1 = 6 \tag{2.40}$$

which gives rise to an intensity ratio of the two peaks of 2:3. Accordingly, the intensity of the doublet peaks of p orbital is 1:2 (this is the case for nickel), while for the f orbital the ratio is 3:4. The exact binding energy value of the emitted photoelectron depends also on the oxidation state of the atom, and the physical and chemical environments. Therefore, a change of the oxidation state of an atom gives rise to a small peak shift in the XPS spectrum, which is known as a chemical shift. An atom with a higher oxidation state reveals a higher binding energy due to the extra columbic interaction between the ion core and the emitting photoelectron. Fig. 2.26 illustrates an example of the chemical shift of the p orbital for Ti and TiO_2. The ability to distinguish between different oxidation states is one of the strengths of XPS.

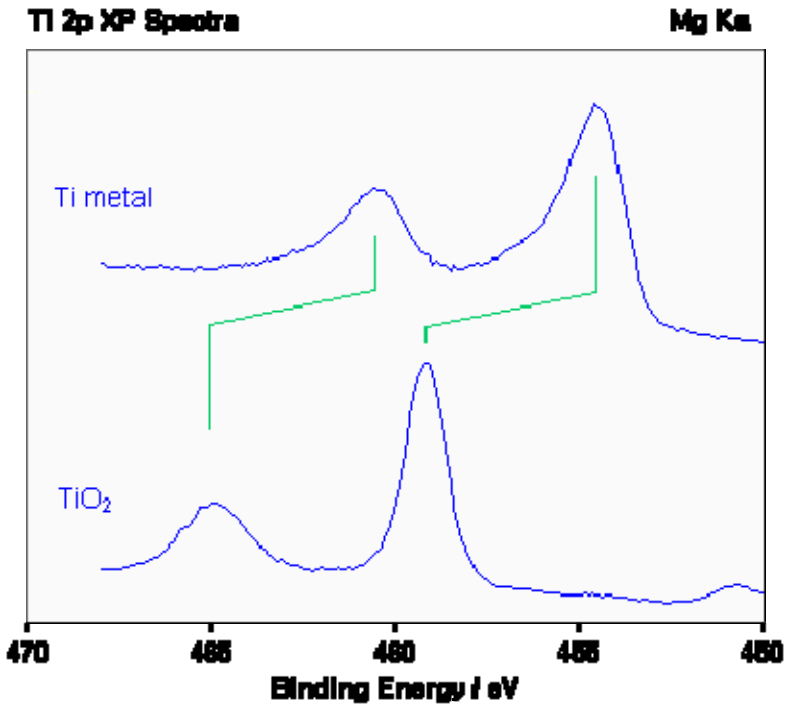

Figure 2.26. XPS spectra for metallic Ti and TiO_2 showing chemical shift [90].

One can notice a stepped background in XPS spectra (i.e. the baseline is at higher intensities for higher values of BE, see Fig. 2.24). This is due the fact that electrons emitted from core levels need to travel through the sample to reach the surface; this distance is known as the mean free path (λ). Electrons close to the surface will escape from the sample and produce a peak in the XPS spectrum, while electrons emitted from deeper levels lose some of their energy due to inelastic interaction. This lost energy is scattered randomly and contributes to the background noise, which appears as an extrinsic tail at higher binding energy in the XPS spectrum, causing an increase in the background at higher values of BE. Fig. 2.27 schematically illustrates the effect of the energy loss on the XPS spectrum.

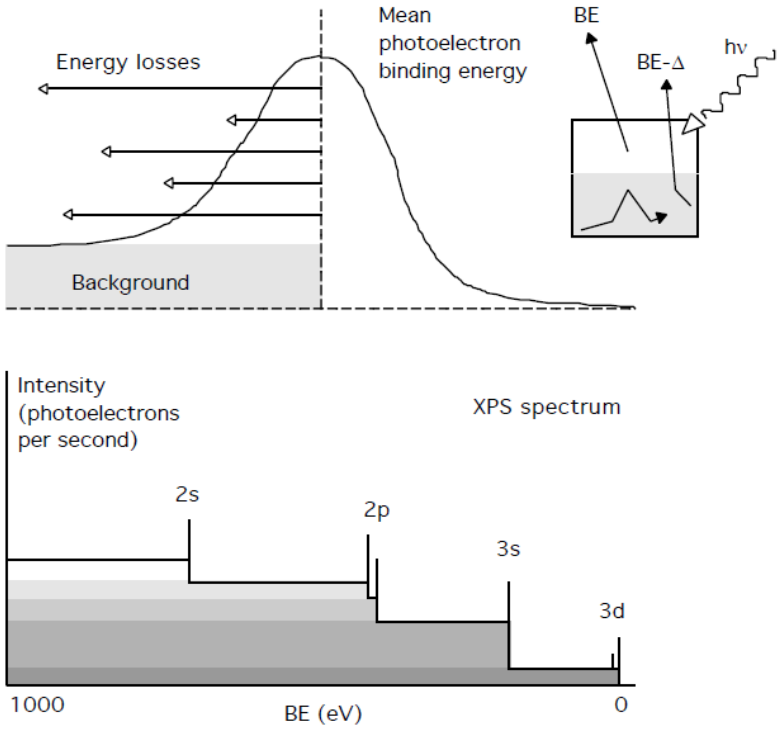

Figure 2.27. Schematic relating the energy loss of core electrons to the stepped baseline in XPS spectra.

Chapter 3 – Experimental Procedures

3.1 Electrodes Preparation

The Ni working electrode was made of a Ni rod (99.999% in purity, AlfaAesar Puratronic) and was 5.0 ± 0.1 mm in diameter. The Ni rod was pre–fitted into a Teflon sleeve (see a in Fig. 1). One side of the electrode was delicately threaded so that it can be connected either to a Teflon covered stainless steel rod, except for the threaded top, which serves as an electrical connector in the electrochemical measurements (see b in Fig. 1) or to a stainless steel made sample holder designed by us and especially fabricated to be used in the Microlab 310 UHV surface analysis system (see c in Fig. 3.1). The other side of the electrode provides a contact surface with the electrolyte; for the electrochemical measurements, as well as a surface chemical analysis where the depth profile experiments are performed. The counter electrode was a Pt foil (99.999% in purity, Goodfellow) of ca. 1.0 cm^2 in geometric surface area. The reference electrode was a Pt/Pt black electrode placed in a separate compartment through which $H_2(g)$ (99.999% Praxair) was bubbled at p = 1 atm. It was immersed in the same electrolyte in which experiments were carried out and served as a reversible hydrogen electrode (RHE). In this contribution, all potentials are given with respect to RHE.

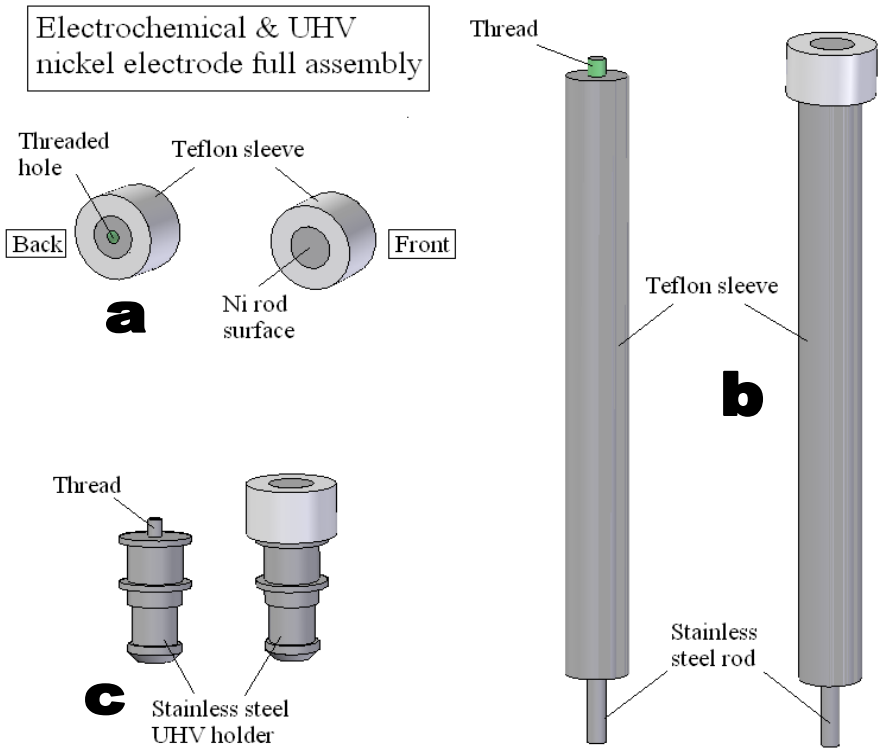

Figure 3.1. Full assembly of the Ni electrode with the two sets to be used in the electrochemical cell and the UHV chamber.

A Pt(poly) wire–shaped working electrode was prepared according to the following steps: (i) initial cleaning the Pt wire (99.999% in purity, and 0.5 mm in diameter, Goodfellow) in acetone under reflux for 6 hours; (ii) welding the Pt wire to an Ag wire for electrical contact; (iii) sealing the Pt wire into pre–cleaned soft–glass tubing, while keeping the welding spot inside the tube (Ag wire was not in contact with the solution), followed by step (i), (iv) cleaning the electrode in concentrated H_2SO_4 for 24 hours, and (v) repetitive washing in high–purity water followed by soaking in water for 24 hours. The geometric surface area (A_{geom}) was determined by measuring the length of the Pt wire using a Vernier microscope and by using the above mentioned diameter; it

was calculated to be 0.59 cm^2. The real surface area (A_r) of the Pt electrode was determined from the charge of H_{UPD} adsorption and desorption [91]. The roughness factor ($R_f = A_r / A_{geom}$) was found to be 1.3.

3.2 Electrolyte and Electrochemical Cell

The electro–oxidation of Ni electrode was studied in 0.5 M aqueous KOH electrolyte solution, while the electro–reduction of Pt electrode was in 0.5 M H_2SO_4 electrolyte solution. The high purity KOH electrolyte solution was prepared from KOH pellets (99.99% in purity, Sigma–Aldrich) dissolved in ultra high purity water (18.2 MΩ cm^{-1}, MilliPore, Milli–Q3). The H_2SO_4 solution was prepared from concentrated H_2SO_4 (Suprapur®, Merck) and ultra high purity water. The electrolyte solutions were subjected to pre–electrolysis with two Pt electrodes for several hours in order to remove any impurities. Nitrogen gas (99.999%, Praxair) was passed through the working–electrode compartment for at least 30 min before the experiment and during experiments to expel any dissolved gases and to remove any gases generated during electrochemical measurements. The working electrodes were cycled 200 times (the Ni electrode was cycled in the potential region where α-$Ni(OH)_2$ formation takes place, while the Pt electrode cycled between 0.05 and 1.4 V) in which the CV profile did not change anymore upon cycling to ensure the reproducibility of the CV profiles. The electrochemical cell used in the course of research was a standard two–compartment all–Pyrex cell with sleeved stopcocks. The glassware was cleaned according to a well–established procedure [55,92].

3.3 Temperature Control

The electrochemical cell was immersed in a water bath (Haake C10) coupled with a chiller (Haake EK20) and the temperature was controlled to within ± 0.5 K by means of a thermostat (Haake D1). To ensure a uniform temperature, the water level in the bath was maintained above that of the electrolyte in the cell. The Ni and Pt electrodes were cycled 200 times at every temperature applied before recording the CV profiles.

3.4 Instrumentation

The electrochemical oxide formation and oxide reduction experiments were performed using a standard EG&G PAR 263A potentiostat interfaced to a Sony Pentium computer that has an EG&G PowerSuite electrochemical software. A 5210 EG&G lock–in amplifier was used for the EIS experiments and data were analyzed using the 2.44 PAR PowerSine software. The XPS depth–profiling experiments were performed using a Microlab 310 UHV surface analysis system coupled with an Acer computer that has an Avantage software.

3.5 Electrochemical and Depth–Profiling Procedures for the Ni Electrode

The Ni rod embedded in the Teflon sleeve was degreased in acetone under reflux and polished with an alumina suspension (down to 0.05 μm, Buehler Micropolish® Alumina) to obtain a mirror–like surface. After polishing, the Ni electrode was thoroughly rinsed with de–ionized water (including rinsing in an ultrasonic bath) and

quickly transferred to the electrochemical cell. To eliminate contact with air, the Ni electrode was protected with a droplet of de–ionized water. Prior to the oxide formation/reduction experiments, the Ni(poly) electrode was polarized at E = –0.2 V for 200 s to reduce any traces of oxide/hydroxide [93], followed by polarization at E = 0 V for 400 s in order to remove any traces of H_2(g) generated in the preceding step. Afterwards, the Ni electrode was cycled 200 times between E = –0.2 and E = 0.5 V to generate a reproducible CV profile and to release any stress from the near–surface region. Surface Ni hydroxide was formed by application of a constant polarization potential (E_p) for a given polarization time (t_p) and at constant temperature in 0.5 M aqueous KOH. The experimental work covered the following range of E_p, t_p, and T values: $0.7 \leq E_p \leq 1.2$ V, $30 \leq t_p \leq 7200$ s, and $278 \leq T \leq 348$ K. Once the oxide grows on the surface of the electrode according to the well–defined experimental procedures, the electrode was immediately removed from the electrolyte solution, rinsed with distilled water and quickly transferred into the UHV chamber (with a droplet of water on the surface). Covering the electrode surface with a droplet of water prevents/decreases the possibility of contaminating the electrode by isolating the surface from being in contact with the atmosphere. As we observed from the XPS analysis, even for the shortest oxidation times, the thickness of the oxidized layer formed is ca. one monolayer. Under such conditions, the metallic Ni surface was no longer in contact with the droplet of water and the rate of possible further oxidation is very small indicating that additional thickening of the passive layer during transport of water covered Ni electrode can be disregarded. An XPS source (Mg anode, XR3, 300 W) and an Ar^+ gun (EX05, 3 kV) were used for photoelectron excitation and sputtering procedures, respectively. The XPS depth profile

experiments were performed as follows: (i) an XPS survey spectrum was recorded before starting the Ar sputtering; (ii) sputtering with the Ar gun for 20 s (the sputtering current in the range of ca. 1.41 μA per ca. 0.172 cm^2); (iii) recording high resolution XPS spectra in the binding energy range of $Ni2p_{3/2}$ and O1s peaks; (iv) repeating step (ii) and (iii) with monitoring the progress in the sputtering process; and (v) recording an XPS survey spectrum to compare the changes before and after the sputtering. The comprehensive set of experimental conditions resulted in over two hundred reproducible results that were subsequently interpreted using oxide–growth theories.

3.6 Electrochemical Procedures for the Pt Electrode

The Pt electrodes were cycled 200 times, prior to the experiments, between 0.05 and 1.5 V to release any stress from the near–surface region and ensure the reproducibility of the CV profiles. The oxide films were grown on Pt by potentiostatic conditions, constant E_p, and well controlled t_p, and T to give more–well–defined methodology than galvanostatic polarization. The formed oxide was reduced in a single negative going CV transient at 50 mV s^{-1}. The oxide reduction CV profiles were integrated and the oxide charge density, q_{ox}, was evaluated. Since the dissolution of Pt in investigated potential range is insignificant [94], the oxide reduction profiles are not influenced by redeposition of previously dissolved Pt cations. We did not face any unexpected difficulties of the reproducibility nature [92] due to the initial electrochemical treatment of Pt electrodes and the electrochemical cleaned condition.

3.7 Chronoamperometry Experiments

The CA experiments were applied to monitor the current density (j) during the Ni hydroxide formation and reduction at E_p = constant according to the following steps: (i) polarization at –0.2 V for 200 s, (ii) polarization at 0 V for 400 – 600 s in order to remove H_2 from the electrolyte by passing N_2 through the solution and (iii) polarization of the electrode at the desired potential for different polarization times.

3.8 Electrochemically Active Surface Area Determination

The electrochemically active surface area (A_r) of the Ni(poly) electrodes was determined on the basis of the charges required to form α-$Ni(OH)_2$ on the electrode surface and according to the method proposed by Avaca et al. [95]. This was accomplished by recording CV profiles at T = 298 K and a scan rate of ν = 100 mV s^{-1} between –0.15 and 0.5 V. The lower potential limit of –0.15 V and the scan rate of 100 mV s^{-1} were selected to minimize the addition of current density from hydrogen evolution reaction to the CV features (H_2(g) generation commences the lower potential limit is approached). The charge (Q_{hox}) of Ni oxidation to α-$Ni(OH)_2$ and that of α-$Ni(OH)_2$ reduction to Ni were found to be in good agreement. The electrochemically active surface area can be calculated from the following equation [95]:

$$Q_{hox} = q_{mono} \times A + C_{dl} \times (E_2 - E_1) \quad (3.1)$$

where q_{mono} is the charge density associated with the formation of 1 ML of α-$Ni(OH)_2$, $q_{1ML,hox}$ = 514 μC cm^{-2} [95,96], A is the electrochemically active surface area of the working electrode, C_{dl} is the double layer capacitance of the material (it is approximately constant throughout the scan and equals to 20 μF cm^{-2} [97]), and E_1 and E_2 are the initial and final potentials of the examined CV peak, respectively. The value of A_r of the Ni disk–shaped electrode was determined to be 0.28 ± 0.04 cm^2.

An alternative method of determining the real surface area is based on double–layer capacitance measurements using electrochemical impedance spectroscopy (EIS) at a constant potential value that is in the region of HER (–0.20 ≤ E ≤ 0.25 V) and at T = 298 K. Under these conditions, Ni electrodes are free of any oxide. The frequency of the AC signal was in the 0.5 Hz ≤ f ≤ 100 kHz range and the other parameters were the same as in routine EIS measurements. The EIS results were treated using the PowerSine software [98]. The HER, which involves an adsorbed intermediate, was represented in the equivalent circuit by a component containing a resistance in series with a sub–circuit containing adsorption capacitance and a resistance, both in parallel [97,99,100]. The double–layer capacitance was represented by a constant phase element and treated according to the procedure described elsewhere and successfully applied to Ni–containing electrodes [97,101,102]. Such an obtained double–layer capacitance value was used to determine the electrode's real surface area by accepting the specific capacitance to be 20 μF cm^{-2} [97,103,104]. According to our data, the real surface area determined using EIS measurements is smaller than the one determined using CV experiments by ca. 9%.

Chapter 4 – Electrochemical Properties of Nickel and Platinum Electrodes

4.1 Nickel Electrode

4.1.1 Structure and Properties of Nickel Compounds

There are two important types of the Ni electrodes used in electrochemistry; the metallic Ni electrode and the nickel hydroxide ($Ni(OH)_2$) electrode. The common preparation method for the nickel hydroxide electrode is by precipitation the hydroxide from a solution containing Ni^{2+} salts [105]. Studies of the structure of the nickel hydroxides are mostly performed using $Ni(OH)_2$ electrodes as starting material rather than metallic Ni electrode. It has been reported that the electrochemical processes for the metallic Ni and nickel hydroxide electrodes reveal some differences [106,107], it is usually accepted that the compounds reported and described for nickel hydroxide electrode are considered in analysis of the metallic nickel electrode. Bode et al. [108], proposed the first scheme of the reactions taking place on the nickel hydroxide electrode. Bode's model is legitimately acceptable and is extensively applied for the analysis of the electrochemical processes that occur on the Ni–based electrodes.

The α-$Ni(OH)_2$ and the β-$Ni(OH)_2$ hydroxides are both semiconducting compounds (p–type) [109-112]. It has been reported that the nickel hydroxide film, electrochemically formed on a metallic Ni electrode in alkaline solution, possesses different properties than a typical semiconductor. This is due to the existence of additional energy states in the energy gap which resulted from the presence of two types

of acceptors or surface states [111]. The structure of the nickel hydroxides (α-$Ni(OH)_2$ and β-$Ni(OH)_2$) is shown in Fig. 4.1 which illustrates their lattice constants and the incorporated species (i.e. water molecule or alkali metal cations) [9,113,114]. The α-$Ni(OH)_2$ hydroxide is hydrated and contains incorporated cations while β-$Ni(OH)_2$ is not. The lattice constant and the angle between the Ni layers are also differ; the structure of the α-$Ni(OH)_2$ hydroxide is known as "turbostratic structure" because the Ni layers are not equally on top of each other and slightly twisted horizontally [113].

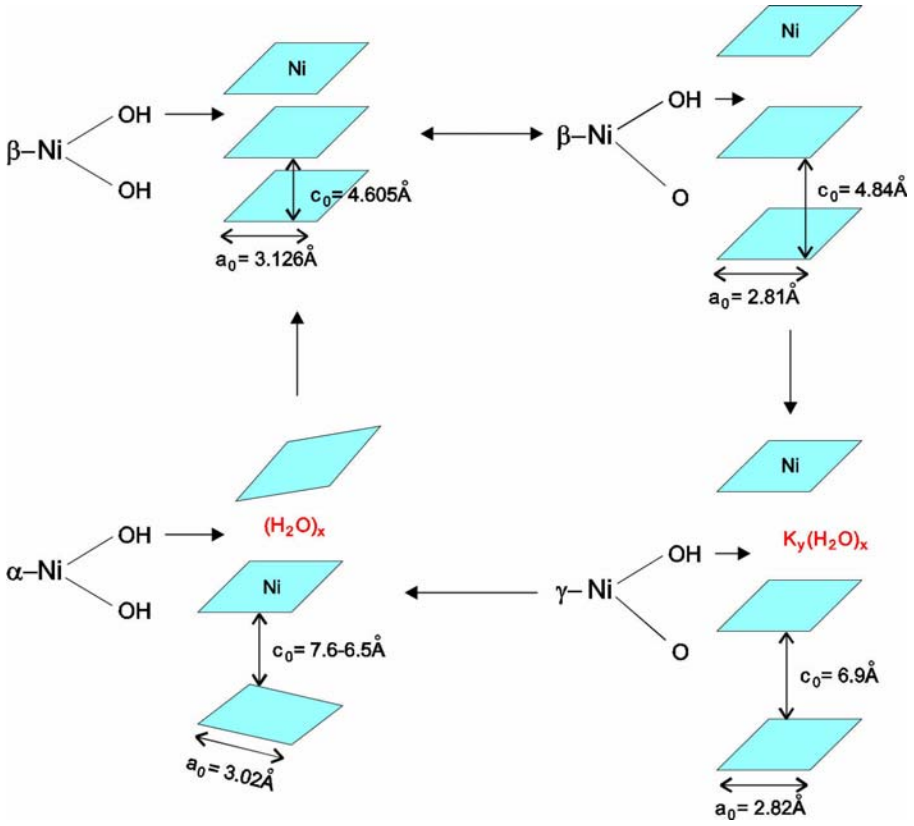

Figure 4.1 Structure of Ni–hydroxides and Ni–oxyhydroxides showing the lattice constant [9,113,114].

4.1.2 General Electrochemical Behavior of the Ni Electrode

Investigation of the electrochemical reactions of the Ni electrode in alkaline media is challenging. This is due to the fact that HER and OER currents are very close or even overlap the current of Ni oxidation and reduction [21,95,103,115,116]. Therefore, a separation of those currents is required for the qualitative analysis of the electrochemical reactions of Ni electrodes. Also, at higher potential values (E > 0.5 V), the redox couple of Ni becomes electrochemically irreversible which makes the process more complicated and challenging.

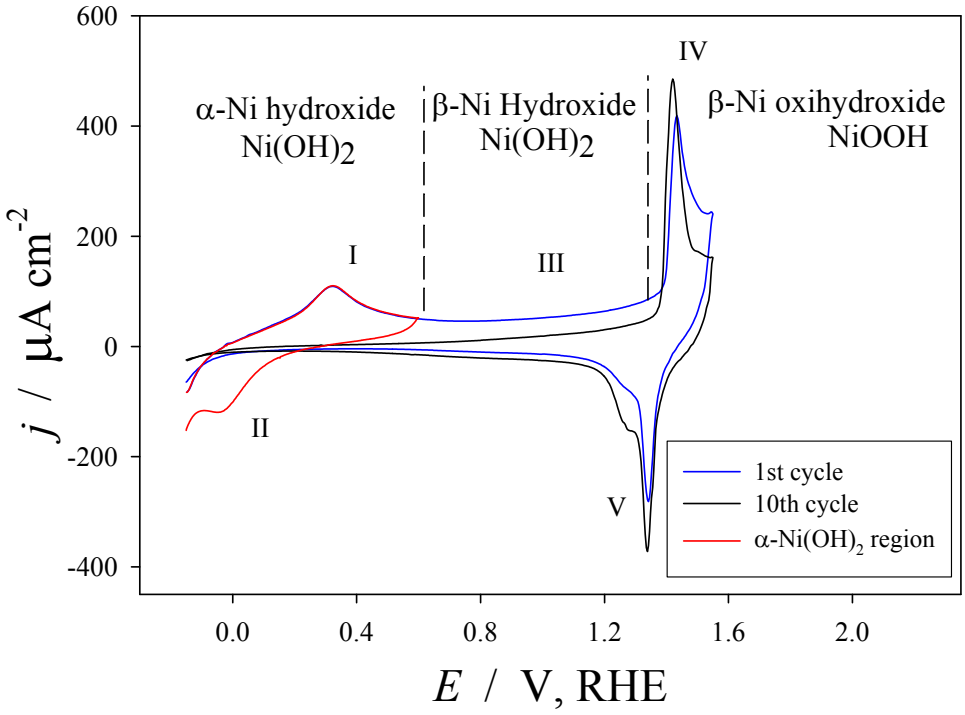

Figure 4.2. Series of CV oxide formation and reduction profiles for polished Ni electrode in 0.5 M aq. KOH solution illustrating the α-$Ni(OH)_2$, β-$Ni(OH)_2$ and NiOOH oxide regions.

Figure 4.2 shows a series of oxide formation and reduction profiles for the Ni electrode polarized in 0.5 M aq. KOH recorded at $-0.15 \leq E_p \leq 0.5$ V (α-$Ni(OH)_2$ region), and at $-0.15 \leq E_p \leq 1.5$ V (subsequent cycles; first and tenth). The assignment of the current peaks is as follows:

Peak (I): electrochemically reversible oxidation of Ni to a Ni(II) compound ($Ni + 2OH^- \rightarrow Ni(OH)_2 + 2e^-$). Although the compound is usually described as α-$Ni(OH)_2$ [10-17], formation of NiO is also reported [15,18-21]. The thickness of the α-$Ni(OH)_2$ layer formed in this potential range is well–defined and the reported values are in the range of 1 up to 6.5 MLs [13,93].

Peak (II): reduction of the compound formed in peak I (the electrode is reduced back to metallic nickel). This process is electrochemically reversible; the compounds formed on the electrode are reduced when the potential scan is reversed at a potential value less positive than 0.5 V.

Region (III): the α-$Ni(OH)_2$ undergoes an irreversible phase transition to β-$Ni(OH)_2$. In addition, oxidation of the metallic Ni at the metal–hydroxide interface directly to β-$Ni(OH)_2$ results in thickening of the β-$Ni(OH)_2$ layer. This potential range is often referred to as a passive region and when it is attained, peaks I and II diminish (see the subsequent cycles) [11,13,106,117].

Peak (IV): oxidation of β-$Ni(OH)_2$ to Ni(III) compound. Usually, NiOOH is considered the product of this process [11,118,119]. Formation of Ni(IV) compound is also reported for bulk–type nickel hydroxide electrodes [120-122].

Peak (V): reduction of NiOOH, previously formed, to β-$Ni(OH)_2$. The electrode cannot be reduced further to metallic nickel.

4.2 Platinum Electrode

The Pt electro–oxidation is extensively studied using variety of electrochemical and surface science techniques [55,123-125]. It has been reported that the initial stage of the Pt oxidation leads directly to the formation of PtO and PtO_2 [123] and does not involve OH_{ads} which is in contrast to what has been reported earlier by Conway et al. [55]. Harrington et al. [126] also reported the formation of PtO using an AC voltammetry technique. More supporting data of the formation of PtO in the initial stages were provided using CV, EQCN, and AES measurements [124,125].

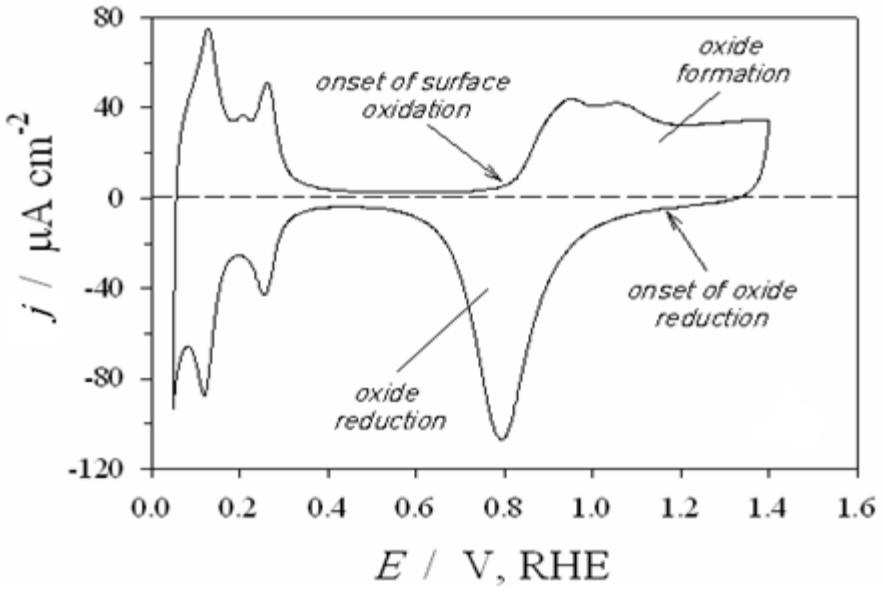

Figure 4.3 CV profile for platinum electrode in 0.5 M aqueous H_2SO_4 at v = 50 mV s^{-1} and at room temperature illustrating the hydrogen adsorption/absorption part and the oxide formation/reduction part.

Figure 4.3 shows a CV oxidation and reduction profile for Pt electrode in 0.5 M aq. H_2SO_4 solution. The potential range of 0.05 – 0.35 V corresponds to the hydrogen adsorption/desorption, while the 0.35 – 0.85 V potential range corresponds to the double layer charging. The formation of PtO oxide takes place at ca. 0.85 V, while the reduction of PtO starts at ca. 1.2 V. The growth of PtO oxide involves different processes (i.e. transfer of the electron, departure of the proton, place exchange between Pt and O, etc.) and the rate–determining step could be one of those processes. The electric field which is established across the oxide layer instigates logarithmic or inverse logarithmic growth kinetics. The logarithmic growth kinetics take place when the process is limited by the interfacial place exchange between the metal atom and the chemisorbed O, while the inverse logarithmic growth kinetics occurs when the process is limited by the escape of

the metal cation from the metal (at the metal–oxide interface) into the oxide layer [127]. The kinetic law of those mechanisms depends on the thickness of the oxide. In a previous study [37], we showed that the initial stages of the PtO formation follows two distinct kinetic laws; a logarithmic growth for PtO layer with a thickness up to 1 ML and inverse logarithmic law for PtO whose thickness is more than 1 ML. The electro–reduction of the PtO layers is not well–studied and there is no theory that describes the electro–reduction of thin oxides.

4.2.1 Structure of the Electrochemically Formed PtO Films

The PtO oxide layers consist of inner PtO layer that grows to a limiting thickness of 2 monolayers and an outer PtO_2 layer [32-36,124-126,128]. This study concerns thin PtO films only, which are formed electrochemically at well–controlled experimental procedures. The structure and the lattice constant of the electrochemically formed PtO layer were reported on the basis of X–ray diffraction (XRD) and surface X–ray scattering (SXS) [24]. The distance between a platinum atom and a platinum cation at the metal–oxide interface ($a'_{Pt-Pt^{2+}}$ = 3.444 Å) and the distance between two platinum cations ($a_{Pt^{2+}-Pt^{2+}}$ = 3.078 Å) were determined using the XRD data [129]. The value of the distance between the Pt atoms and the Pt cations is important in the determination of the kinetic parameters and the electric field established across the oxide film.

Chapter 5 – Electro–Oxidation of metallic Ni electrode to β-$Ni(OH)_2$ in the potential range of $0.7 \leq E_p \leq 1.2$ V

5.1 *Introduction*

The electrochemical behavior of a nickel electrode in alkaline media is a proper example of a classical corrosion behavior of a metal that demonstrates a well developed active ($E_p \leq 0.5$ V), passive ($0.5 < E_p < 1.3$ V), and transpassive ($E_p \geq 1.3$ V) states. Those potential regions correspond to the formation of α-$Ni(OH)_2$, β-$Ni(OH)_2$ and NiOOH hydroxide/oxide, respectively [130,131]. Thus, the former two potential regions correspond to the oxidation of metallic Ni to various Ni(II) compounds, while the latter is related to the formation of Ni compounds with a higher oxidation state, usually Ni(III) [11,19,118,132,133]. The kinetics and mechanisms of the formation of α-$Ni(OH)_2$ and NiOOH have been extensively studied using various electrochemical techniques, such as cyclic voltammetry, chronoamperometry, and electrochemical impedance spectroscopy [17,107,134-140]. The mechanistic studies of the passive region, where the formation of β-$Ni(OH)_2$ takes place, is more complicated and difficult to determine with a reasonable accuracy because the CV profile for this region reveals a featureless current plateau (see Fig. 5.1). Furthermore, the process of β-$Ni(OH)_2$ formation is electrochemically irreversible and the compound formed is very hard to reduce, at all [13,106,141,142]. This strongly complicates the kinetic studies of β-$Ni(OH)_2$ formation because the amount of the passive layer formed cannot be estimated from the charge density of their redox couple, in contrast to e.g. noble metals [37]. Thus, application of the typical electrochemical techniques that are based only on current or charge measurements have

significant limitations in determining the transferred charge in the passive region. A precise analysis of the electrochemically formed passive film requires the application of suitable non–electrochemical methods that follow the electrochemical polarization of the Ni electrode at well–defined experimental conditions.

Ex–situ ultra high vacuum (UHV) based surface chemical characterization techniques coupled with argon ion bombardment for depth profiling studies is an appropriate method allowing one to determine the thickness of thin layers, such as oxide films. X–ray photoelectron spectroscopy (XPS) is one of the methods used for monitoring the progress in the sputtering process [143]. Subsequently, by analyzing the changes in the XPS spectra and the shape of the Ni and the O bands, the end of the sputtering process and the thickness of the layer under study can be determined. The XPS experiment has been previously applied in the analysis and the discussion of the various oxidation states of the nickel electrode [144-148]. In addition, the XPS–depth profiling has been employed in the studies of Ni chemical oxidation (by gaseous O_2 or water vapor) [148], and also for the electrochemical oxidation of Ni alloys in low concentrated alkaline solutions [149]. However, until now there has been no attempt made to apply this method in the study of the metallic Ni electro–oxidation in alkaline solutions or to study the kinetics and the mechanism of the Ni electro–oxidation.

Despite the extensive studies of the active and the transpassive regions of a Ni electrode in an alkaline solution, only a few reports have been devoted to the kinetic studies of the electrochemically formed Ni passive films [150-152]. Damjanovic et al. applied cyclic voltammetry and coulometry to study the mechanism of β-$Ni(OH)_2$ formation on Ni electrode in KOH solutions at T = 298 K and for different values of pH,

namely 12, 13 and 14 [150-152]. They reported that the oxidation of Ni in the potential range where β-$Ni(OH)_2$ formation takes place follows the Mott–Cabrera model [153] with high field assisting the metal cation escape as a rate determining step. Since then, no other kinetic studies of nickel oxides/hydroxides formation in the passive region have been reported in the literature. Other studies were only concerned about the composition of the passive layer without substantial discussion of the kinetics and the mechanism of the process or the thickness of the film [11,18-20,115,132,154].

In this chapter we report new data for the kinetics studies of a metallic Ni electrode oxidized in the potential region where the formation of β-$Ni(OH)_2$ takes place in 0.5 M aqueous KOH solution at well–defined E_p, t_p, and T values. The hydroxide layers were electrochemically formed to develop the β-$Ni(OH)_2$ film with different thicknesses. An ex–situ XPS–depth profiling method was employed to determine the thickness of the film and to estimate the charge density of the electrochemically formed β-$Ni(OH)_2$ layers. The relation between the oxidized layer thickness and the oxidation parameters (E_p, t_p and T) allows us to discuss the applicability of different oxide–growth models to the formation of β-$Ni(OH)_2$ at the specific E_p, t_p and T values.

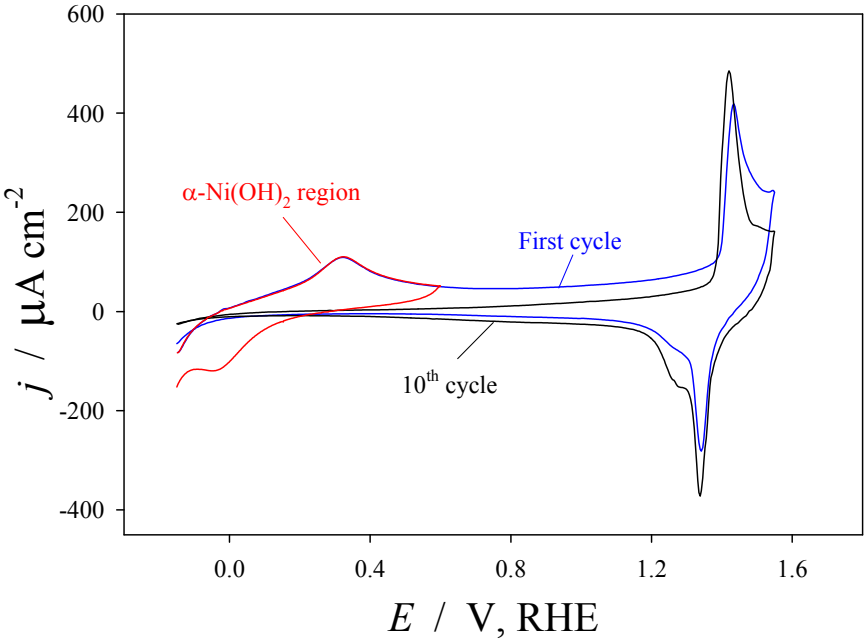

Figure 5.1. Series of CV oxide formation and reduction profiles for Ni electrode in 0.5 M aq. KOH solution illustrate the α-$Ni(OH)_2$ peaks and NiOOH region.

In Fig. 5.1, we show CV oxide formation and reduction profiles for Ni electrode recorded in 0.5 M aqueous KOH solution at v = 100 mV s^{-1}, for $-0.20 \leq E_p \leq 1.55$ V and at T = 298 K. The reversible oxidation of metallic Ni electrode takes place at a potential range of $-0.20 \leq E_p \leq 0.50$ V [21,95,115,141,155], while the irreversible oxidation (passive region) starts at ca. $E_p > 0.50$ V [11,13,132,141,155,156]. The anodic current peak observed at ca. 0.30 V and the reduction peak at ca. –0.05 V correspond to the reversible formation and reduction of Ni(II) compounds, respectively

[21,95,115,141,155]. Usually, α-$Ni(OH)_2$ is assumed to be the product of the oxidation [10-14,16,17,118,131,134] but the existence of NiO is also suggested [18-21,159].

At potentials positive to 0.50 V, and up to ca. 1.30 V, a featureless current plateau is observed that is attributed to the passive region of Ni. In this potential range, further oxidation of Ni takes place and this process is electrochemically irreversible [11,13,115,141,156]. The compound formed in this potential range (passive region) is usually described as β-$Ni(OH)_2$ [11,132,146,155]. A comparison of curves recorded for 1^{st} and subsequent cycles (Fig. 5.1) indicates that this process leads to vanishing of the redox couple peaks of α-$Ni(OH)_2$ [106,141]. Additionally, a significant decrease in the oxidation currents is observed in this potential range. Polarization of the Ni electrode in this potential range for lengthened time decreases the oxidation currents to very low values, which makes it very difficult to obtain reliable measurements. As a result, application of standard electrochemical analysis methods (i.e. peak current vs. scan rate [107,135] or reduction charge vs. polarization time [37,127,160,161]) are not considered. Thus, under such conditions, the application of a non–electrochemical technique that determines the thickness of the oxide/hydroxide layer and subsequently the charge density of the passive region is required.

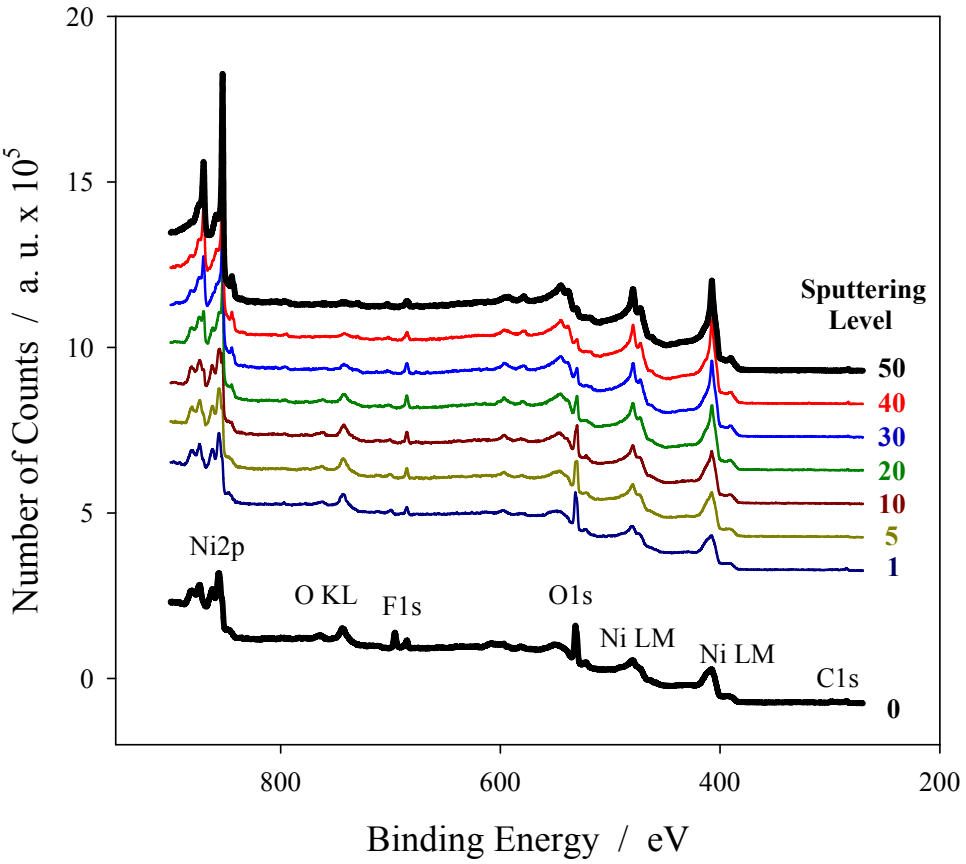

Figure 5.2. XPS survey spectra for Ni electrode in 0.5 M aq. KOH solution polarized at E_p = 1.2 V, T = 298 K and for t_p = 2700 s before starting the sputtering procedures and the subsequent cycles.

In Fig. 5.2, we show XPS survey spectra for Ni electrode polarized in 0.5 M aqueous KOH at E_p = 1.2 V, T = 298 K and for t_p = 2700 s. The spectra illustrate the changes in the electrode surface before, during and after completing the Ar^+ sputtering procedures. We observed the $Ni2p_{3/2}$ and O1s peaks at 856 and 531 eV binding energy (BE), respectively, as well as traces of carbon (C1s) and fluorine (F1s). After the first sputtering cycle, the C1s and the F1s peaks are diminished indicating that the origin of those peaks is traces of surface contamination. The presence of fluorine suggests that the

source of the F and C contamination is the Teflon sleeve and not from the air or the UHV chamber as the surface of the electrode is maintained covered and isolated from the ambient the entire time. Thus, it could be that some compounds containing C and F were liberated from the Teflon part during the degassing procedure and re–adsorbed on the electrode surface. A comparison of the intensities of the contamination peaks of C and F with main peaks of $Ni2p_{3/2}$ and O1s indicates, however, the surface contamination is practically insignificant and has no influence on the sputtering results presented in this study and on the Ni/O ratio.

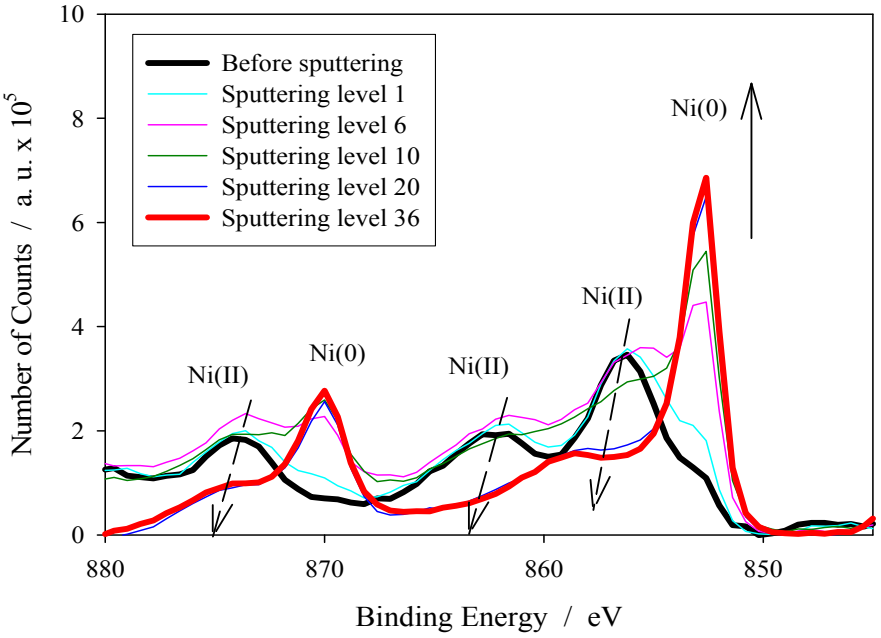

Figure 5.3. XPS spectra for the Ni2p peaks for Ni electrode recorded on the basis of Fig. 5.2 illustrating the change in the Ni2p peaks with the progress in the sputtering process.

In Fig. 5.3, we present a Ni2p high resolution spectrum for Ni electrode polarized in 0.5 M aqueous KOH at E_p = 1.2 V, T = 278 K and t_p = 7200 s after the Ar^+ sputtering procedures. The arrows in the figure indicate the change in the Ni peaks with the progress in the sputtering process. The spectra recorded before the sputtering process reveal the main $Ni2p_{3/2}$ peak at ca. 856 eV which is attributed to Ni^{2+} [145-148]. At higher binding energies (ca. 862 and 880 eV) satellite peaks are observed, such peaks are discussed elsewhere, e.g [145]. When a thin hydroxide layer is formed on the electrode surface, we observe a small shoulder at lower BE of the main Ni(II) peak in the Ni spectrum (ca. 852 eV) that corresponds to the metallic Ni electrode [145-148,162]. It is worth mentioning here that the depth of the XPS analysis reaches a value of a few monolayers [143,147,163-165]. This clearly indicates that the observed Ni(0) signal does not have to originate from unoxidized electrode surface and can originate from the bulk of the electrode. When the oxidation time becomes shorter, this peak becomes more pronounced but under our experimental conditions ($0.70 \leq E_p \leq 1.20$ V and $60 \leq t_p \leq 3600$ s) the area of this peak was very small compared to the area of the Ni(II) peak at 862 eV. We observe a gradual increase in the Ni(0) peaks along with the satellite peaks and a simultaneous decrease in the Ni(II) peaks. A shift of ca. 5 eV is observed between the Ni(II) main peak and Ni(0) main peak as the hydroxide layer is gradually removed from the surface of the electrode. After several tens of sputtering cycles (depending on the hydroxide thickness) we observe a typical Ni spectrum corresponding to a clean Ni electrode (the red curve in Fig. 5.3).

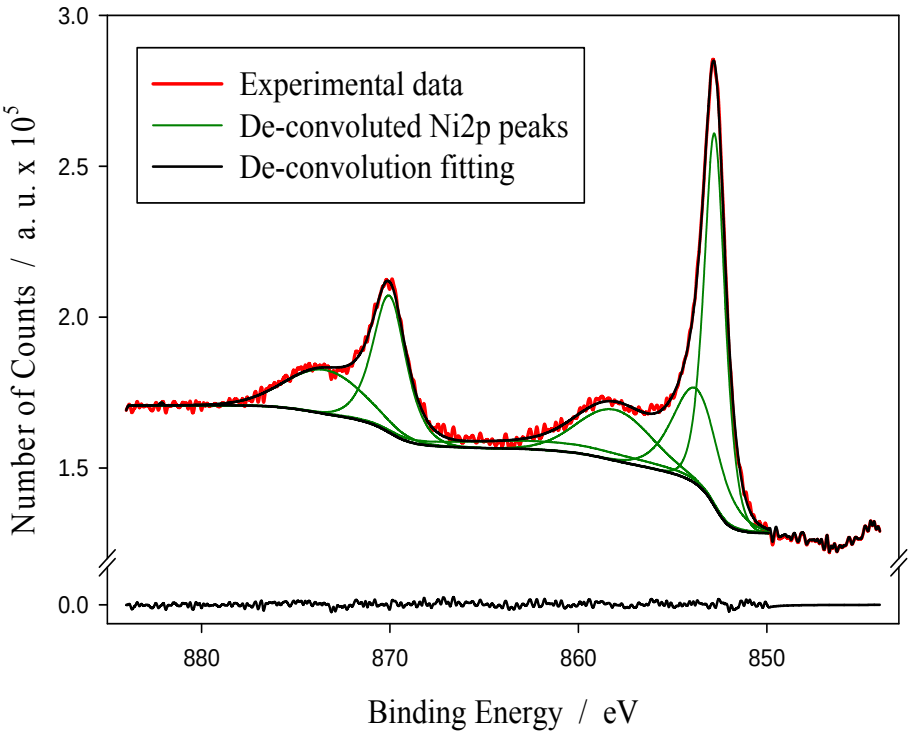

Figure 5.4. XPS spectra for Ni electrode in 0.5 M aq. KOH polarized at E_p = 1.2 V, T = 278 K and at t_p = 60 s illustrates the deconvolution of the Ni2p peaks.

In Fig. 5.4, we present a Ni2p spectrum for Ni electrode polarized in 0.5 M aqueous KOH at E_p = 1.2 V, T = 278 K and t_p = 60 s after the Ar^+ sputtering procedures. The entire Ni2p spectrum, along with its satellite peaks, was deconvoluted into 6 peaks that include $Ni2p_{3/2}$ and $Ni2p_{1/2}$ for Ni(II) and Ni(0). Although a Shirley–type background was used for the deconvolution [166,167], the same qualitatively and quantitatively results were also obtained by using a linear–type background. The black curve at the bottom of Fig. 5.4 illustrates the residuals from the curve fitting, which is equally distributed around the zero axis indicating a good quality of the fit. The deconvolution of the Ni peaks is out of the scope of this study and can be found elsewhere [166,167].

The spectra of the oxygen (O1s) reveal a significant change in the shape and position of the O1s peak during the first few sputtering cycles, see Fig 5.5. Before starting the sputtering procedure, we observe a relatively sharp oxygen peak at ca. 532 eV. According to the literature [144-146,148,159], the O1s peaks recorded for Ni samples at ca. 532 and 534 eV can be attributed to the adsorbed atomic and molecular oxygen, respectively. This peak disappears after ca. 2 sputtering cycles and a new one, at ca. 529.7 eV appears which can be attributed to negatively charged oxygen bounded to the Ni electrode [144,145]. Furthermore, the progress in the sputtering procedures does not change the position of the new oxygen peak and only induces a change in the area of this peak (the new oxygen peak is broader than the first one). Finally, this peak gradually diminishes upon the progress in the sputtering cycles.

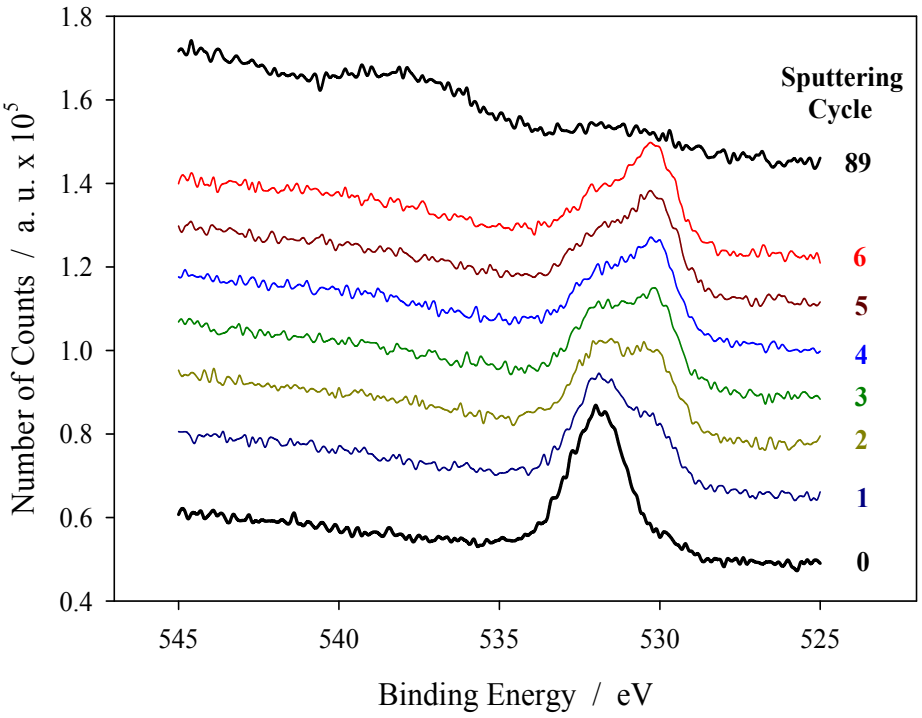

Figure 5.5. XPS spectra for Ni electrode in 0.5 M aq. KOH solution recorded on the basis on Fig. 5.2 illustrate the change in the O1s peak with the sputtering process.

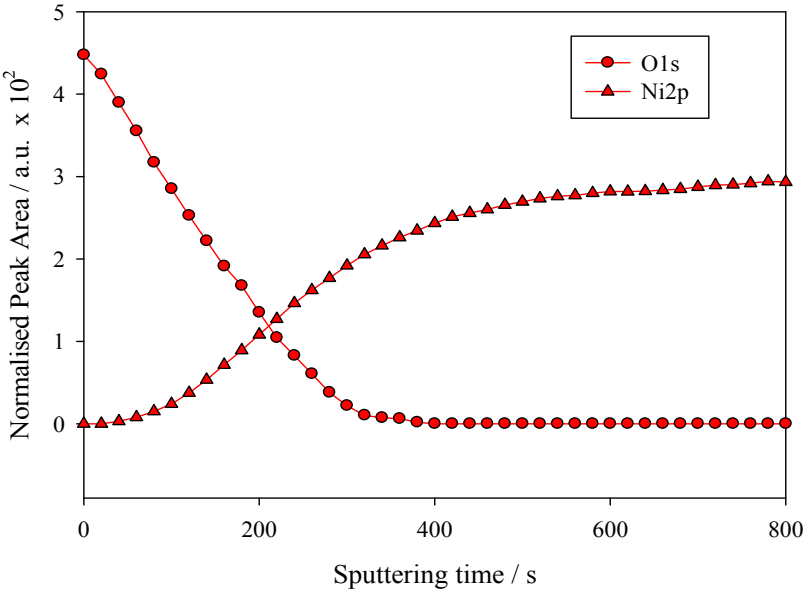

Figure 5.6a. A depth–profile plot for Ni electrode in 0.5 M aq. KOH polarized at E_p = 0.9 V, T = 298 K and at t_p = 300 s shows the change in the peak area of the Ni2p and the O1s peaks.

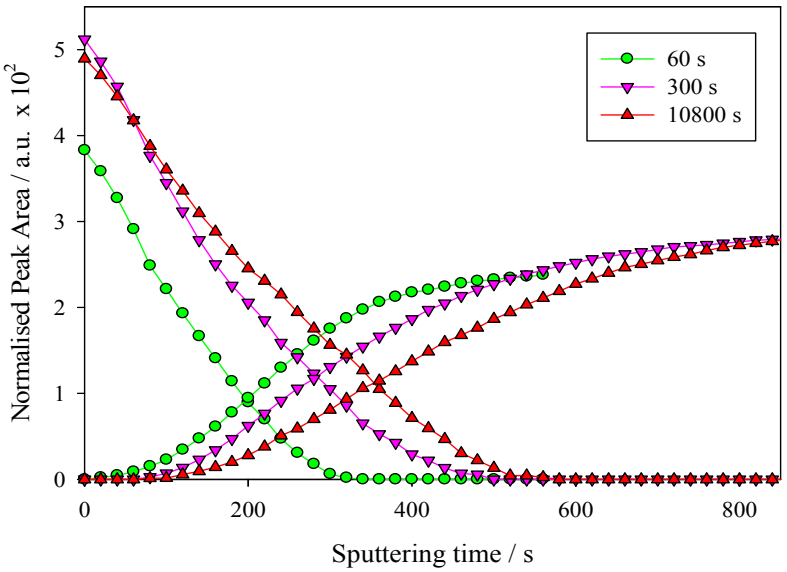

Figure 5.6b. Depth–profile plots for Ni electrode in 0.5 M aq. KOH polarized at E_p = 1.1 V, T = 298 K and at various t_p values, namely 60, 300 and 10800 s.

In Fig. 5.6a, we show a depth–profile (sputtering time) plot for $Ni2p_{3/2}$ and O1s peaks obtained for Ni electrode polarized in 0.5 M aqueous KOH at E_p = 0.9 V, T = 298 K and for t_p = 300 s. We observed that the area of the $Ni2p_{3/2}$ peak increases while the area of the O1s peak decreases as a function of the sputter time (sputter time is a function of sputter cycles). This can be explained by the gradual removal of the β-$Ni(OH)_2$ layer exposing more Ni(0) to the surface of the electrode [168]. In Fig. 5.6b, we show a series of depth–profile curves for Ni electrode polarized in 0.5 M aq. KOH at E_p = 1.1 V, T = 298 K and for three different values of t_p, namely 60, 300 and 10800 s. We observed that as the polarization time increases, the sputter time needed to remove the hydroxide layer also increases. This is due to the fact that upon the extension of the polarization time, a thicker hydroxide is formed which requires a longer exposure time to the Ar^+ beam to gradually remove it. We also observed that the $Ni2p_{3/2}$ profile is broad (the region of the ascending part of the profile) and there is not a sharp transition from Ni(II) to Ni(0). There are a few reasons that could affect the shape (broadening) of the profile such as: (i) non–homogeneity of the surface (roughness and various crystal faces exposed), (ii) non–uniformity of the Ar^+ beam (different beam intensity at the edges than the center of the sputtered area), (iii) preferential sputtering (removal of one element more than the other), etc. The broadening of the $Ni2p_{3/2}$ profile is out of the scope of this study and can be found in e.g. [146]. Therefore, the end of the sputtering process is usually selected as the point lying in the half of the maximum intensity of the $Ni2p_{3/2}$ signal [143]. Due to significant broadening of the depth profile in the region of the interface with the O1s profile, the error of the analysis is relatively high. However, as it will be shown later,

scattering of the data obtained is relatively small indicating high reliability of the analysis based on the presented depth profiles.

5.4.1 Determination of the Ta_2O_5 Oxide Thickness using the Depth–Profile Procedures as a Model Method to Estimate the β-$Ni(OH)_2$ Thickness

The depth–profile experiments were also performed on a tantalum oxide foil repetitively in order to investigate the reliability of this method in estimating the oxide thickness. In addition, a Ta_2O_5 oxide residing on a Ta foil is also used to calibrate the XPS depth–profile apparatus (i.e. to ensure that the XPS beam and the Ar^+ beam are directed at the same area of the sample, see Fig.5.7). Tantalum as a pure metal has a dark grey color, while the Ta_2O_5 oxide electrochemically formed on the Ta surface has a different color depending on the oxide thickness (i.e. a dark blue or purple color is observed for a thickness of 50 nm of Ta_2O_5). The difference in color between the pure metal (substrate) and the oxide (at the surface) is very useful in the depth–profile experiment as one can visually determine whether the oxide film is removed totally. Another characteristic feature of the Ta_2O_5 layer is that the electrochemical growth of the oxide film depends only on the applied voltage and not on the current or the concentration of the electrolyte solution [169]. Thus, a particular thickness of the Ta_2O_5 oxide film can be attained through precise experimental procedures. The relation between the thickness of the Ta_2O_5 oxide and the applied voltage is mathematically illustrated in the following equation:

$$Applied\ voltage\ (V) = Desired\ thickness(nm) \times 0.6\ V/nm \qquad (5.1).$$

In this study, the Ta foil was polarized in a dilute citric acid and connected to the positive end of the power supply (growth of Ta_2O_5 is anodic). A platinum electrode is used as a cathode that is immersed in the same electrolyte solution and connected to the negative end of the power supply. The value of the applied voltage was 30 V in order to obtain a Ta_2O_5 oxide with a thickness of 50 nm according to equation 5.1. After that, the Ta_2O_5 foil was placed on top of our Ni electrode to maintain the same sample height and position in the UHV chamber, see Fig. 5.8 for the Ta_2O_5 foil after the depth–profile experiment. The XPS depth–profile procedures were employed as explained in the experimental chapter. The sputtering ratio for a Ta using 3 kV Ar^+ beam energy at 100 μA cm^{-2} is 0.127 nm s^{-1} [170-172]. Figure 5.9 illustrates the Ta4f spectrum (Ta_2O_5 peaks at ca. 26.3 and 28.2 eV correspond to $Ta4f_{7/2}$ and $Ta4f_{5/2}$, respectively) prior to the sputtering process as well as the subsequent spectra for different sputtering cycles. The Ta_2O_5 peaks and the Ta4f peaks are in agreement with the standard Ta and Ta_2O_5 spectra reported in [173].

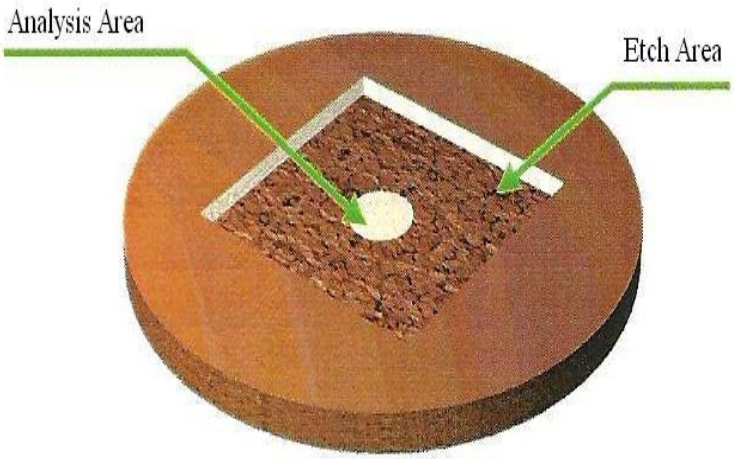

Figure 5.7. Schematic XPS sample diagram illustrates the etch and the analysis areas [170].

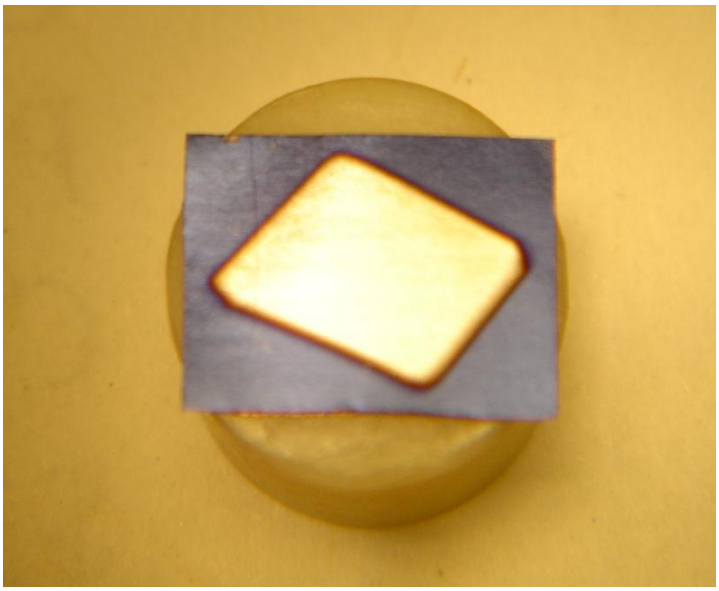

Figure 5.8. The Ta_2O_5 foil on top of the Ni electrode illustrates the etch area after the sputtering process.

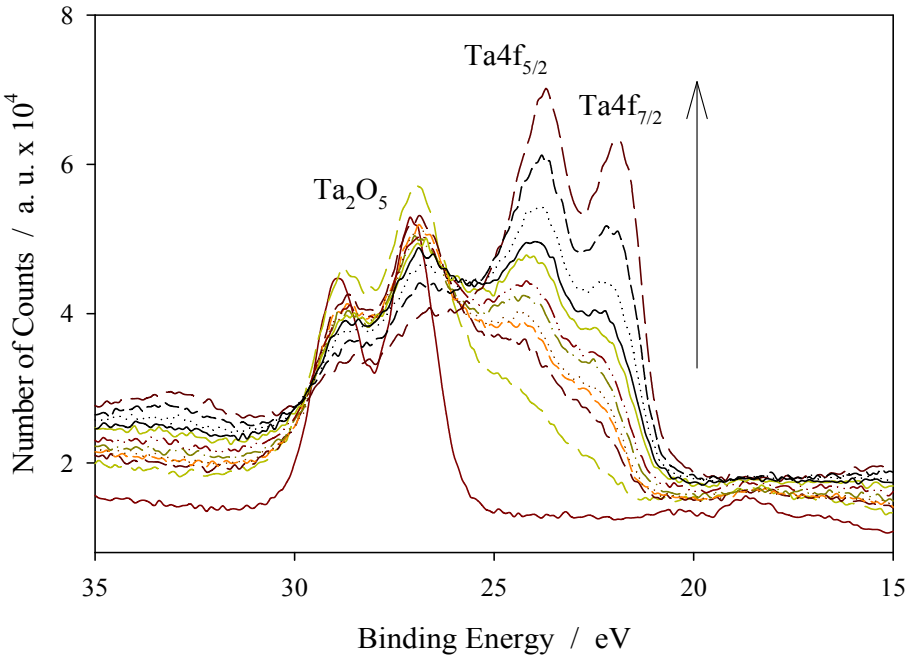

Figure 5.9. XPS spectra for the Ta_2O_5 foil depict the change in the $Ta4f_{7/2}$ and $Ta4f_{5/2}$ peaks during the sputtering process.

A depth–profile plot for the Ta_2O_5 oxide is presented in Fig. 5.10 for the Ta4f and O1s peaks. A sharp increase in the Ta profile and simultaneously a rapid decrease in the O profile indicate the removal of the oxide film exposing the substrate to the X–ray beam. The end of the sputtering point (the intersection of the two profiles) represents the time needed to remove the oxide layer [174]. Knowledge of the sputtering current, the sputtering area and the sputtering time allows us to determine the oxide thickness. The depth–profile experiments were performed for the Ta_2O_5 oxide foil prior to almost every Ni sample studied in order to achieve the same experimental conditions for the Ta_2O_5 and the Ni electrodes and to ensure the reliability of the results. The value of the Ta_2O_5 oxide thickness determined from the depth–profile method is 47.4 ± 0.5 nm. A comparison of

the obtained value of thickness with the theoretical one (i.e. 50 nm) indicates a good reliability of the depth–profile method in estimating the thickness of the oxide layer.

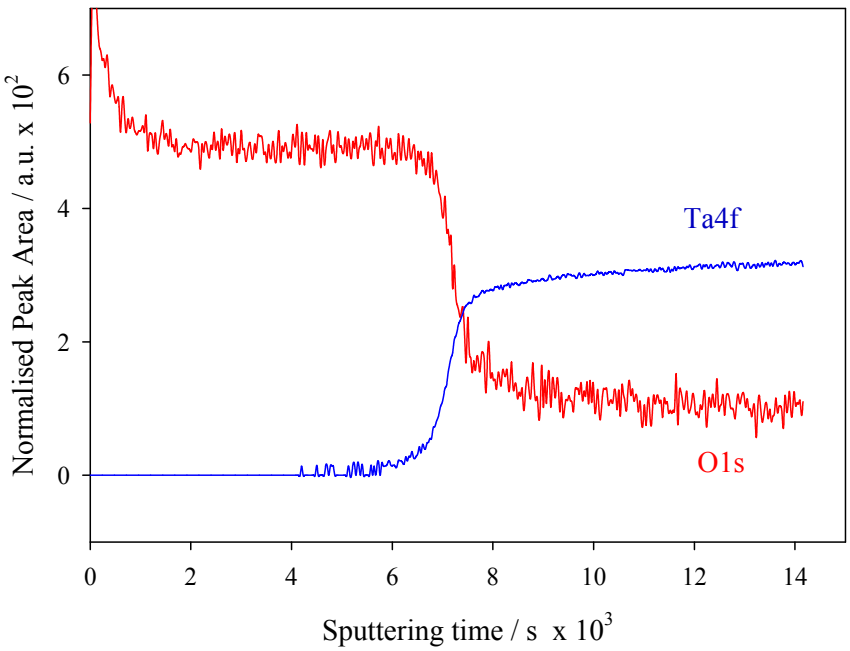

Figure 5.10. Depth–profile plot for the Ta_2O_5 oxide used to determine the time needed to remove the oxide layer.

5.5 Mechanism of Ni Electro–Oxidation in 0.5 M Aqueous KOH at 0.70 ≤ E_p ≤ 1.20 V

The thickness of the electrochemically formed β-$Ni(OH)_2$ hydroxide was determined in the same manner as that of Ta_2O_5. The etched area of the β-$Ni(OH)_2$ layer was accepted to be the same as that in the case of Ta_2O_5 by ensuring the same depth–profile setup, sample position, UHV pressure, energy of the Ar^+ beam, etc. The obtained value of the β-$Ni(OH)_2$ thickness is used in the estimation of the growth kinetics and mechanism of the passive film. This can be achieved by direct analysis of the β-$Ni(OH)_2$ layer thickness as a function of polarization conditions or by converting the thickness to a

charge density value. In the instance of converting the thickness to a charge density value, knowledge of the charge density that corresponds to the formation of one monolayer of the studied oxide/hydroxide as well as the thickness of one monolayer are required. For the β-$Ni(OH)_2$ hydroxide electrochemically formed on metallic Ni electrode, the charge density corresponding to the formation of one monolayer is ca. 478 μC cm^{-2}. In this study, we analyzed the thickness rather than the charge density of the obtained β-$Ni(OH)_2$ hydroxide as a function of the experimental conditions.

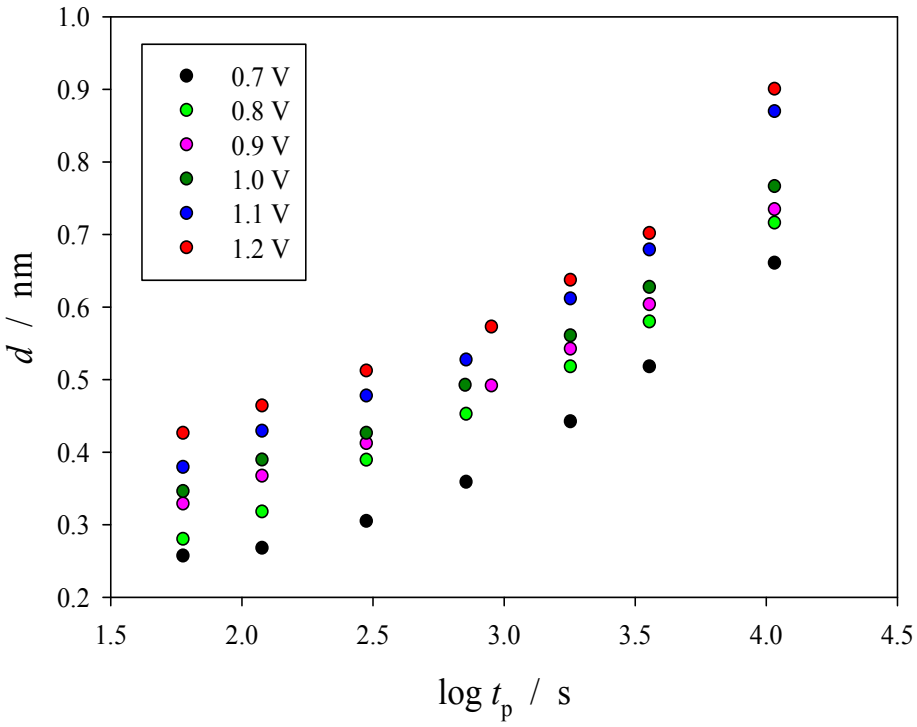

Figure 5.11. β-$Ni(OH)_2$ thickness versus log t_p relation for Ni electrode in 0.5 M aq. KOH solution recorded at $T = 298$ K, $60 \leq t_p \leq 10800$ s and $0.7 \leq E_p \leq 1.2$ V.

In Fig. 5.11, we present the thickness (d) of the electroformed β-$Ni(OH)_2$ layer as a function of log t_p for Ni electrode recorded in 0.5 M aqueous KOH at $T = 298$ K, $60 \leq t_p$

≤ 10800 s and for various polarization potential values, in the range of $0.7 \leq E_p \leq 1.2$ V. The data reveal that the thickness of the electroformed β-$Ni(OH)_2$ layer increases with the polarization time. For instance, as the polarization time increases from 60 up to 10800 s, we observed an increase in the β-$Ni(OH)_2$ layer thickness from 0.38 to 0.87 nm at a constant polarization potential (E_p = 1.1 V). Furthermore, at constant t_p, the thickness of β-$Ni(OH)_2$ layer also increases with the increase of the polarization potential values towards more positive values. We also observed a non–linear relation between d and log t_p, which implies that the growth of β-$Ni(OH)_2$ layer is non–logarithmic (discussed in the following section).

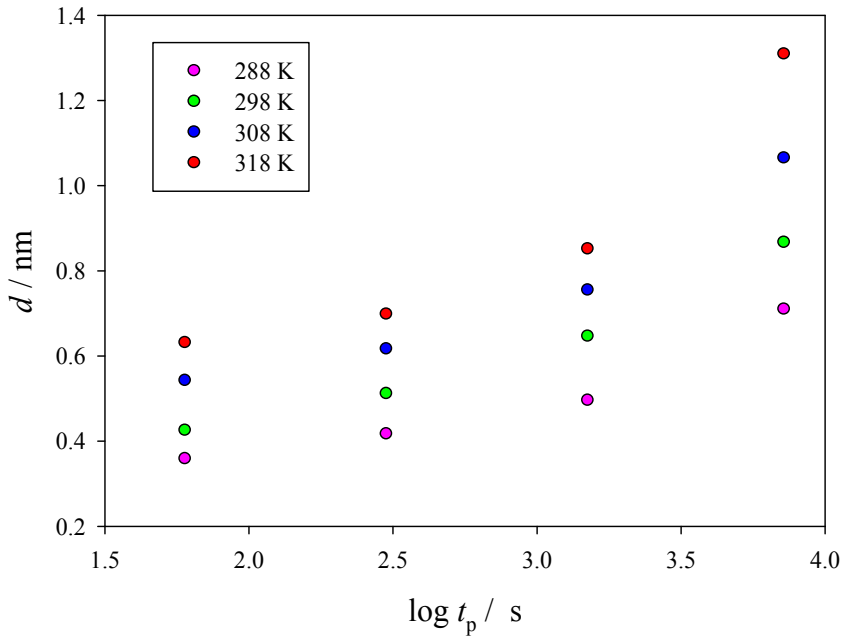

Figure 5.12. β-$Ni(OH)_2$ thickness vs. log t_p relation for Ni electrode in 0.5 M aq. KOH solution recorded at E_p = 1.2 V, $300 \leq t_p \leq 7200$ s and $288 \leq T \leq 318$ K.

In Fig. 5.12, we show the d vs. log t_p relations for Ni electrode in 0.5 M aqueous KOH recorded at E_p = 1.2 V, 300 ≤ t_p ≤ 7200 s and for various oxidation temperatures, namely 288, 298, 308 and 318 K. The data reveal that the thickness of the electrochemically formed β-Ni(OH)$_2$ layer increases as T is raised and/or t_p extended. The comprehensive set of d vs. log t_p data obtained for the range of E_p, t_p and T values, allows us to analyze the kinetics and the mechanism of Ni electro–oxidation in the potential region of β-Ni(OH)$_2$ formation. A linear relation between the reciprocal of β-Ni(OH)$_2$ thickness, d^{-1}, and log t_p is observed. Figure 5.13 illustrates this linear d^{-1} vs. log t_p relation for the Ni electrode in 0.5 M aqueous KOH obtained for 60 ≤ t_p ≤ 10800 s, T = 289 K and for 0.7 ≤ E_p ≤ 1.2V.

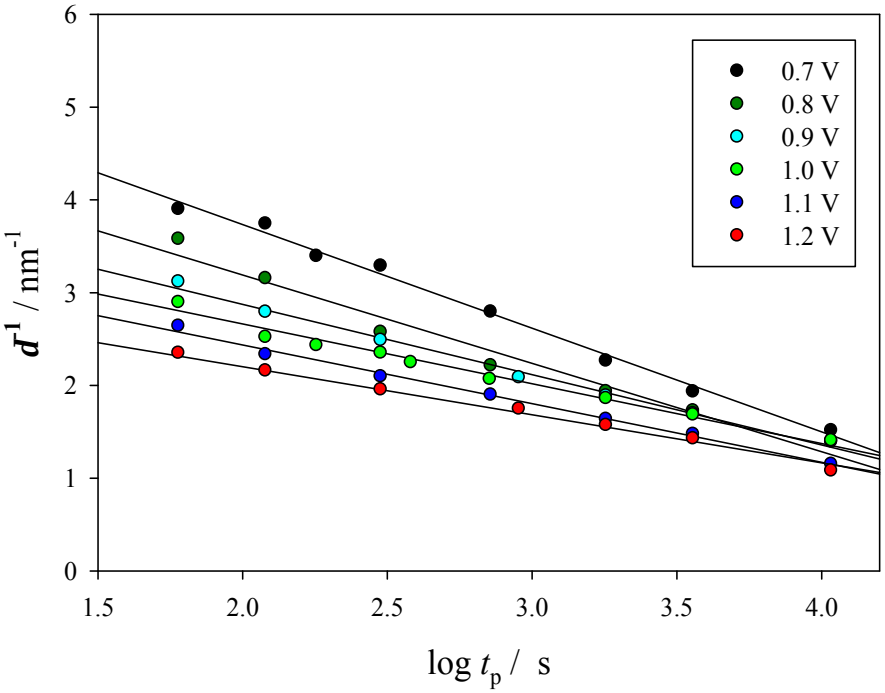

Figure 5.13. d^{-1} vs. log t_p relation for Ni electrode in 0.5 M aq. KOH solution recorded at T = 298 K, 60 ≤ t_p ≤ 10800 s and 0.7 ≤ E_p ≤ 1.2 V.

The linear d^{-1} vs. log t_p relations observed in Fig. 5.13 imply that an inverse–logarithmic law and a respective growth mechanism are applicable to the growth of the hydroxide layer under our experimental E_p, t_p and T conditions. In a previous study, we showed that the growth of α-Ni(OH)$_2$ in the potential region of $-0.2 \leq E_p \leq 0.5$ V follows logarithmic growth kinetics [175]. Thus, it should be emphasized that when a transition from one growth law to another takes place, a short non–liner region is expected. An inverse logarithmic law, i.e. a linear relation between d^{-1} vs. log t_p, is predicted by Mott–Cabrera theory [153]. This model assumes that the slowest step in the process is the escape of the metal cation from the metal into the oxide film at the metal–oxide interface. This process is assisted by a strong electric field that established across the oxide layer. The Mott–Cabrera mechanism is widely used to describe the formation of thin oxide layers (thickness above one monolayer) of many noble metals, such as Pt and Rh [37,127,160,161]. Moreover, Damjanovic et al. [150-152] reported that the inverse–logarithmic law is applicable for Ni electrodes polarized in alkaline solution. The mathematical equation quantifying this process has the following form:

$$\frac{\mathrm{d}d}{\mathrm{d}t} = N\,\Omega\,\nu_{\mathrm{ib}} \exp\left(\frac{-H}{k_B T}\right) \exp\left(\frac{q\,a'\,V}{d\,k_B T}\right) \qquad (5.2)$$

where N is the surface density of atoms, Ω is the volume of the oxide per metal atom, ν_{ib} is the vibration frequency of the surface metal atom (usually of the order of 10^{-12} s^{-1}), $H = H_i + U$, where H_i is the enthalpy of solution of the cation in the oxide and U is the activation energy barrier for the metal cation diffusion in the oxide, V / d is the electric field across the oxide, a' is the distance between the metal cation and the top of the

activation energy barrier (a' = 1.72 Å), q is the charge of metal cation and k_B is the Boltzmann constant. Rearranging Eq. 5.2 gives:

$$\frac{1}{d} = \frac{1}{d_1}\ln\left(\frac{d_1\, u}{d_L^2}\right) - \frac{1}{d_1}\ln t_p \qquad (5.3)$$

where $d_1 = q\ a'\ V\ /\ k_B\ T$, $u = N\ \Omega\ \nu_{ib}$ exp $(-H\ /\ k_B\ T)$, and d_L is the limiting oxide thickness. The slope of d^{-1} vs. log t_p plot is the simplest parameter to discuss due to the fact that it does not contain any parameter that is hard to quantify (i.e. H, Ω and ν_{ib}) as in the intercept in equation 5.3. The slope of d^{-1} vs. log t_p allows us to determine the potential drop across the interface and subsequently the electric field strength (see table 5.1).

Another confirmation of the inverse–logarithmic process is obtained through the fitting of our experimental results into the thin–oxide layer theories by determining the X_o and X_1 parameters, which represent a particular oxide thickness and have the following forms [35,54,153]:

$$X_o = \left(\frac{\kappa k_B T}{8\,\pi\, n_{ion}\, q^2}\right)^{1/2} \quad \text{and} \quad X_1 = \frac{q\ a\ V}{K_B T} \qquad (5.4)$$

where κ is the dielectric constant of the film, n_{ion} is the number of metal ions per unit volume, q is the charge of the metal cation, V is the potential across the oxide, a is the distance between the metal cations in the film (or the distance between the metal atom and the metal cation in the inner metal–oxide interface), k_B is the Boltzmann's constant

and T is the temperature. The Mott–Cabrera theory predicts that, when a film of chemisorbed species is present on the metal surface, a tunneling of the electrons from the metal to the chemisorbed O–containing species will take place. Consequently, a strong electric field develops across the metal–oxide interface which is accountable for the escape of the metal cation from the metal to the oxide at the inner metal–oxide interface. The growth of very thin oxides is known to be logarithmic or inverse–logarithmic in time. The applicability of these kinetic laws can be verified by comparing d to X_o and X_1. Thus determination of X_o and X_1 is important to differentiate between the two mechanisms. The applicability of specific thin–oxide growth kinetics can be examined by comparing the experimentally obtained oxide thickness (d) to the X_o and X_1 parameters according to the following cases [35,54]:

a- In the case of thick oxide films $d >> X_o$, the growth kinetics are controlled by the transfer of the metal cation from one interstice site in the film to another.

b- In the case of thin oxide film $d << X_o$, electrons are transferred to the oxide film and a strong electric field (the electric field strength is $E = V/d$) develops. The strong electric field leads either to the escape of the metal cation from the metal surface into the oxide or to the movement of the cation in the oxide film as a rate determining step. If the obtained oxide thickness (d) is smaller than X_o but greater than X_1, then the migration of the metal cation is proportional to the electric field and the rate determining step is the movement of the metal cation in the oxide film. In the case when the value of d is smaller than both X_o and X_1, then the electric field is strong and the escape of the metal cation is no longer proportional

to it and the rate determining step is the escape of the metal cation from the metal into the oxide.

The calculated X_1 value for the Ni hydroxide equals 325 Å (by taking a = 3.1 Å and V = 1 V). The determination of the X_o value is more complicated since it contains the κ and n parameters which are difficult to evaluate. In our case, the obtained oxide thickness d is smaller than X_1 and since X_1 is always smaller than X_o, then our oxide thickness d is smaller than both the X_1 and X_o parameters. Under such condition, the rate of the metal cation escape from the metal surface into the metal–oxide interface is the rate determining step. Thus, the growth kinetics can be determined on the basis of the inverse–logarithmic theory of Mott–Cabrera [35,54].

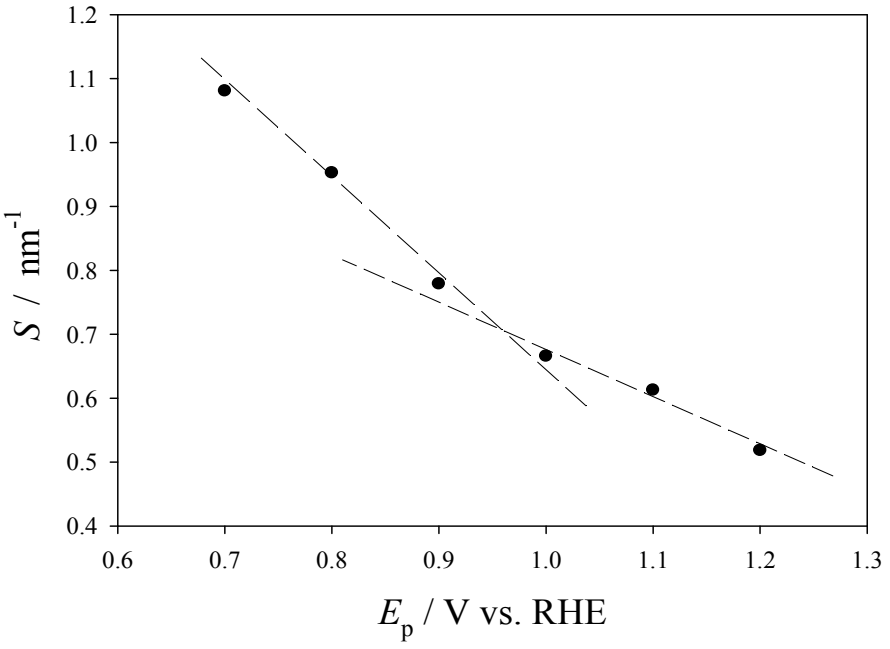

Figure 5.14a. Slope of Mott–Cabrera equation (Eq. 5.3) vs. E_p calculated on the basis of Fig. 5.13.

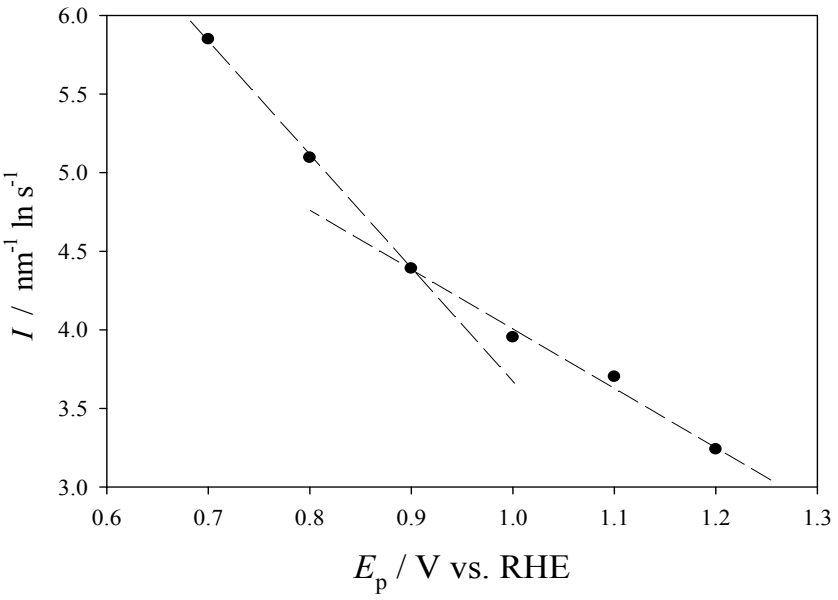

Figure 5.14b. Intercept of Mott–Cabrera equation (Eq. 5.3) vs. E_p calculated on the basis of Fig. 5.13.

In Fig. 5.14, we show the influence of the oxidation potential on (a) the slope of Mott–Cabrera equation (*S*) and (b) the intercept for the same equation (*I*). We observed that at higher oxidation potential values, the slope of Eq. 5.3 becomes smaller and simultaneously the intercept value also decreases. Thus, the polarization potential affects the slope and the intercept in a similar manner. The fact that the slope of Eq. 5.3 decreases as E_p increase can be explained as a result of the increase in the potential drop (*V*) across the oxide film with the increase in E_p values, see Table 5.1. In addition, the oxide thickness (*d*) also increases with E_p, therefore the electric field established across the oxide ($E = V/d$) is almost constant for the range of E_p values applied, see Table 5.1. This is understandable if we assume that the nickel oxides/hydroxides have semiconducting properties, usually of a p–type [111,136,158,176,177]. Thus, due to the concentration of the charge carriers, which is lower than in the case of conductors, the

potential drop established across the oxide–electrolyte and the metal–oxide interfaces resulted in formation of an electric field across the oxide film. We also observed that the slope and the intercept of Mott–Cabrera equation (Figs. 5.14a and 5.14b) changes with the applied potential. There are two differentiated slopes in Figs 5.14a and 5.14b that could be attributed to the changes in the value of the potential drop across the oxide (V) as the oxidation proceeds.

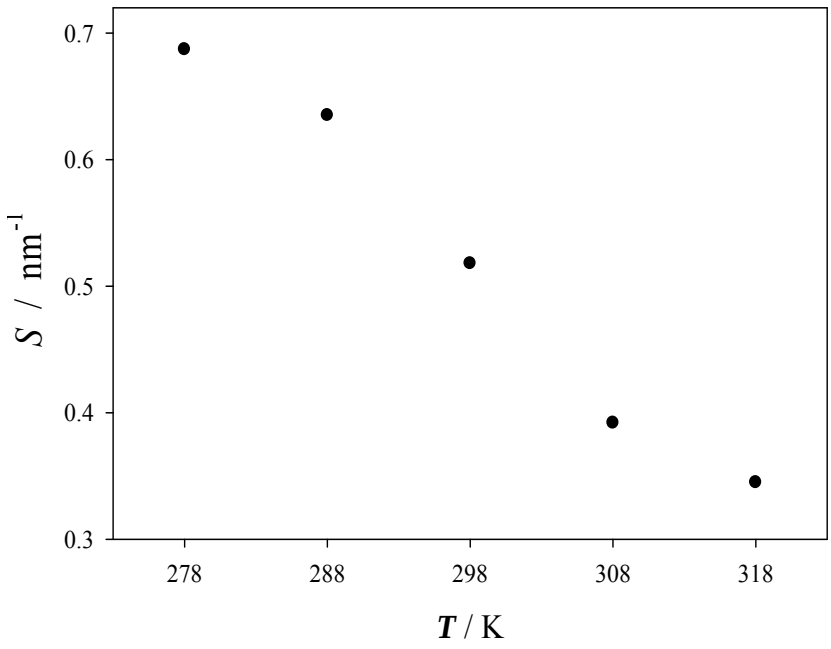

Figure 5.15a. Slope of Mott–Cabrera equation (Eq. 5.3) vs. T for Ni electrode in 0.5 M aq. KOH solution recorded at E_p = 1.2 V, t_p = 300 s and for 278 ≤ T ≤ 318 K.

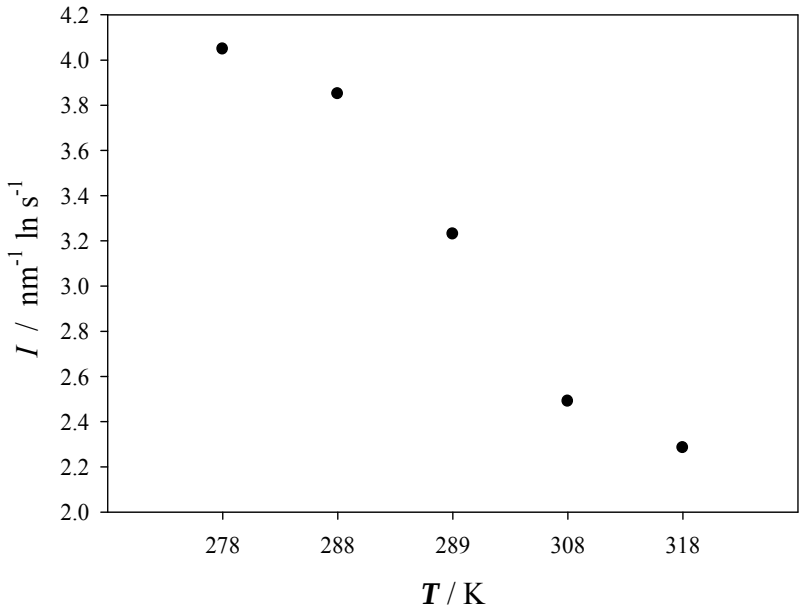

Figure 5.15b. Intercept of Mott–Cabrera equation (Eq. 5.3) vs. T for Ni electrode in 0.5 M aq. KOH solution recorded at E_p = 1.2 V, t_p = 300 s and for 278 ≤ T ≤ 318 K.

Figures 5.15a and 5.15b illustrate the temperature influence on the (a) slope and (b) intercept of Mott–Cabrera equation obtained for Ni electrode at E_p = 1.2 V, t_p = 300 s and 278 ≤ T ≤ 318 K. We note that the value of the slope decreases and the intercept becomes smaller with the increase in T values. The temperature affects the potential drop across the oxide film and it has been reported that the higher the T values the greater the drop in the potential across the oxide [37,160]. Furthermore, the temperature also affects the thickness of the oxide layer; the oxide becomes thicker at higher values of T. Thus, this behavior explains the constant electric field in this T range. The same effect was also observed for noble metal electrodes in which the potential drop across the oxide increases with T while the overall electric field is practically temperature independent due to simultaneous increase of d [37,160].

Explanation of the decrease of the intercept with the potential is more complicated since this term contains several components which may be affected by the oxidation potential such as V, d_L or H. Contribution from V can be eliminated by combining the intercept and the slope of Eq. 5.3 according to the following equations:

$$I = Intercept = \frac{1}{d_1}\ln\left(\frac{d_1\,u}{d_L^2}\right) \quad and \quad S = Slope = \frac{1}{d_1} \tag{5.5}.$$

Introducing the slope (S) into the intercept (I) equation gives:

$$I = S\ln\left(\frac{u}{S\,d_L^2}\right) \tag{5.6}$$

$$I = S\left(\ln\frac{u}{d_L^2} - \ln S\right) \tag{5.7}.$$

Taking the $(\ln\frac{u}{d_L^2}) = W$ (where W independed of V) and rearranging Eq. 5.7 gives:

$$I = S\,(W - \ln S) \tag{5.8}$$

$$W = \frac{I}{S} + \ln S \tag{5.9}$$

where W is a function of the intercept and the slope of Mott–Cabrera equation (Eq. 5.3) independent of V. Based on the results presented in Fig. 5.13 and by using Eq. 5.9, we determined the value of W at various E_p, t_p and T. In Fig. 5.16, we show the relation

between W and the applied potential recorded for Ni electrode at $0.7 \leq E_p \leq 1.2$ V. We know that $W = \ln \frac{u}{d_L^2}$, where $u = N\ \Omega\ v_{ib}\ exp^{\frac{-H}{k_B T}}$, thus we can write:

$$W = \ln \frac{N\ \Omega\ v_{ib}\ exp^{\frac{-H}{k_B T}}}{d_L^2} \quad (5.10).$$

Rearranging Eq. 5.10 gives:

$$W = \frac{-H}{k_B T} + \ln \frac{N\ \Omega\ v_{ib}}{d_L^2} \quad (5.11).$$

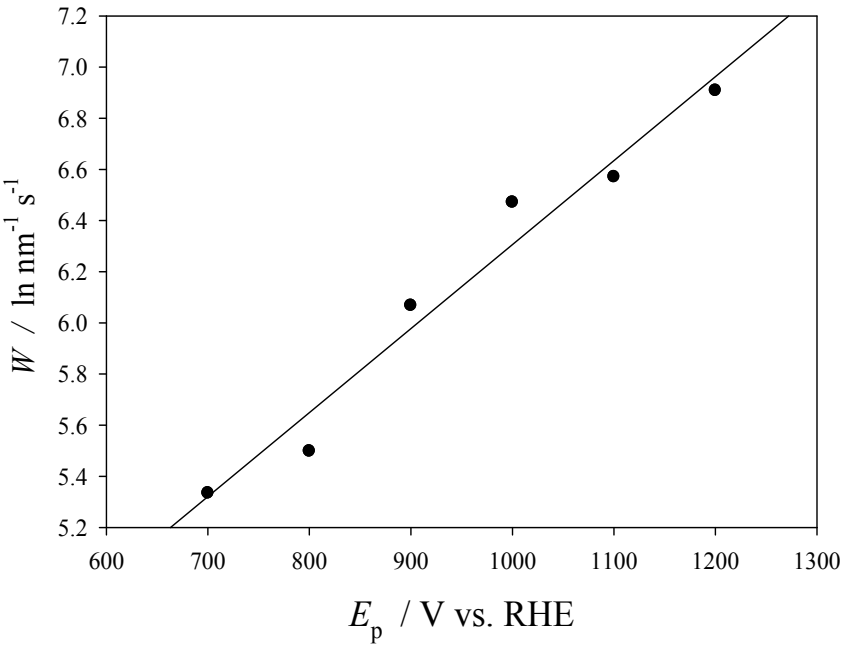

Figure 5.16. W vs. E_p relation for Ni electrode in 0.5 M aq. KOH solution recorded at T = 298 K and at $0.7 \leq E_p \leq 1.2$ V.

One can note the increase in the W values at higher E_p values. From Eq. 5.11, the parameters that could change the value of W are the H ($H = H_i + U$) and/or the limiting oxide thickness d_L. As the value of the limiting thickness should not decrease with an increase in E_p, thus it follows from Eq. 5.11 that the main factor governing the increase in the W value is the influence of the potential on the H value. Furthermore, it is reasonable to assume that the activation barrier (U) should not increase with the oxidation potential as the driving force of the process (i.e. the electric field) increases continuously with E_p [178]. Thus, the only reasonable explanation of the increase in the H value is the increase in the enthalpy of solution H_i ($H = H_i + U$). According to Hess's law, the enthalpy of solution of cation in the oxide could be considered as a difference between the enthalpy of Ni oxide/hydroxide formation and the enthalpy of the substrates (i.e. nickel and oxygen ions). The Ni and O ions are charged or form dipoles (i.e. Ni-O or Ni-OH bonds), therefore, their enthalpy of formation will be affected by the electric field applied. This, in turn, results in a temperature dependence of the overall enthalpy of the solution, H_i. For the analysis of the intercept, we also applied Eq. 5.3 and parameter W as a function of T^{-1}. This is plotted in Fig. 5.17 for the Ni electrode polarized at $E_p = 1.2$ V for $t_p = 300$ s and $278 \leq T \leq 318$ K.

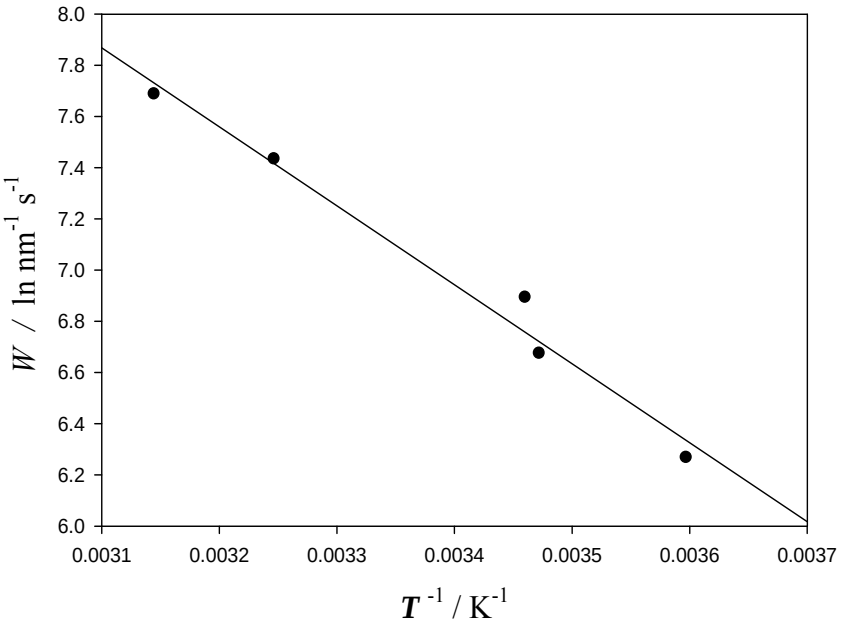

Figure 5.17. W vs. T^{-1} relation for Ni electrode in 0.5 M aq. KOH recorded at E_p = 1.2 V, t_p = 300 s and at 278 ≤ T ≤ 318 K.

As follows from Fig. 5.17, W is a linear function of T^{-1} and the intercept must then be independent of T (in this T range), otherwise the linearity will not be obtained. In this T range, the value of N, Ω and ν_{ib} are constant, thus the value of the limiting thickness can be determined from the intercept by knowing the values of N, Ω and ν_{ib}. This is a new method in estimating the d_L using these results.

The slope of Eq. 5.11 allows us to calculate the value of H which contains the enthalpy of solution of the cation in the oxide and the activation energy of the cation hopping (Eq. 5.2). These two parameters cannot be calculated separately on the basis of our data only. For the oxidation potential of 1.2 V, the H value is determined to be 26.5 kJ mol^{-1}. There are no equivalent data in the literature, especially for $Ni(OH)_2$, which can be compared to our results of H and we can only compare our results with different systems. Furthermore, there are no data in the literature about the activation energy

barrier (U) for $Ni(OH)_2$; otherwise the heat of the solution (H_i) could be determined. The obtained H value is significantly smaller than the enthalpy of formation of Ni oxides during thermal oxidation with O_2, when no external electric field is applied, which is in the range of 240 – 220 kJ mol^{-1} at T = 298 K [179-182]. Additionally, it is smaller than the activation energy of the Ni cations transport in the Ni oxide that is in the range of 185 – 280 kJ mol^{-1} at 540 – 1700 °C [182-185]. The enthalpy of ionization of the Ni and O during the NiO formation is in the range of thousands of kJ mol^{-1} [181]. The obtained value of H does not contain the activation energy of the Ni cation or the enthalpy of O_2 adsorption/dissociation. Thus, the obtained H value is substantially smaller than that of formation of NiO in reaction with O_2. Another explanation for the smaller value of H than the activation energy is that the transport of the Ni cation in the strong electric field that is established across the oxide could significantly lower the activation energy barrier [182-185]. The data obtained were treated using the Mott–Cabrera model and we determined the potential drop across the oxide film at various E_p values. Then, the value of the potential drop were divided by the oxide thickness in order to determine the strength of the electric field (E) that established across the oxide, see table 5.1. Our results reveal that the strength of the electric field is consistently in the range of 0.015 – 0.197 × 10^9 V m^{-1} as expected form the Mott–Cabrera theory [153]. The potential drop across the interface depends on the experimental conditions, however the electric field remains constant because an increase of V is assisted by an increase of the thickness, thus leading to the same field strength for different E_p values.

Table 5.1. Kinetics parameter for the oxide growth on Ni electrode at $0.7 \leq E_p \leq 1.2$ V and $T = 298$ K derived on the basis of Mott–Cabrera theory [153].

Oxidation Potential, E_p , (V) RHE	Potential drop across the oxide, (V)	Electric field established across the oxide, 10^9 (Vm^{-1})
0.70	0.014 – 0.057	0.015 – 0.167
0.80	0.025 – 0.059	0.025 – 0.210
0.90	0.027 – 0.061	0.037 – 0.187
1.00	0.026 – 0.091	0.040 – 0.197
1.10	0.029 – 0.094	0.039 – 0.178
1.20	0.034 – 0.071	0.038 – 0.168

5.6 Conclusions

Oxidation of Ni electrode in an alkaline solution in a potential range of $0.7 \leq E_p \leq 1.2$ V vs. RHE was studied by means of CV and XPS depth–profiling techniques. The kinetics of the Ni oxidation was determined on the basis of d^{-1} vs. log t_p relations. A linear relation between d^{-1} and log t_p is observed which indicates that the oxidation growth proceeds according to the Mott–Cabrera model. The value of the slope of Mott–Cabrera equation decreases with the increase in the oxidation potential, which indicates

an increase in the electric field across the oxidized film. The thickness of the oxidized layer increases with the increase in oxidation time and/or temperature values.

Chapter 6 – Electro–Oxidation of β-$Ni(OH)_2$ that resides on metallic Ni electrode to NiOOH oxide

6.1 Introduction

Nickel is one of the elements that are most often used to construct different types of electrodes for a variety of industrial applications. It is utilized in its metallic form, as well as a component of various alloys and compounds. The latter includes oxygen containing Ni(II) and Ni(III) compounds most often applied in alkaline solutions (different forms of $Ni(OH)_2$ and NiOOH, see Fig. 4.1). Nickel hydroxide electrodes are usually obtained through the precipitation of $Ni(OH)_2$ species from solutions containing a mixture of Ni salts [186]. Bode et al. proposed a scheme for the $Ni(OH)_2$ electrode that serves as a background in the analysis of those electrodes in alkaline solution [108]. This scheme includes reversible and irreversible reactions of the $Ni(OH)_2$/NiOOH redox couple, the reactions that take place at the anode in alkaline batteries [187,188]. Usually, the reaction scheme for $Ni(OH)_2$ electrodes is also applied to metallic nickel with the assumption that the structure and composition of Ni(II) and Ni(III) compounds, formed on both types of electrodes, are similar. This, however, is not fully justified since many authors report differences between electrochemical processes taking place on metallic Ni and $Ni(OH)_2$ electrodes, as well as differences in the structure of the compounds formed [15,18-21,106,189]. The latter concerns mainly the possible formation of NiO with or without a layer of $Ni(OH)_2$ [15,18-21,118,154,158]. Conversely, some authors directly confirmed the existence of $Ni(OH)_2$ on metallic Ni electrode on the basis of atomic force microscopy (AFM), scanning tunneling microscopy (STM), soft X–ray spectroscopy

(SXS), X–ray scattering, ellipsometry, photon emission microscopy (PEM), Raman spectroscopy, UV–visible and IR spectroscopy [10,11,13,17,118,119,137,158].

The oxidation mechanism of Ni hydroxide in alkaline solution was reported mainly for $Ni(OH)_2$ electrodes; the process is usually assumed to be accompanied by transport (diffusion) of a proton in the solid phase [190,191]. This process is also reported to be accompanied by transport of alkali metal cations and/or water into or from the electrode surface [106,192-203]. These alkali metal cations act as counter ions in non–stoichiometric Ni compounds [199,203]. The cyclic voltammetry (CV) and CA data of Zhang et al. [107] shows that the proton diffusion process is the rate determining step (r.d.s.) in the overall electrode process. Barral et al. [136] also reported that the r.d.s is proton diffusion during the oxidation of Ni(II) to Ni(III) using electrochemical impedance spectroscopy (EIS). Conversely, Arvia et al. [13,139,140] proposed a complex model containing two charge transfer steps, one of them with a proton transfer, accompanied by one or two chemical reactions. Arvia et al. model suggests that the diffusion of the proton is not the rate determining step. However, the proposal made by Arvia et al. has not been confirmed by other authors.

If proton diffusion is assumed to be the r.d.s., then the diffusion coefficient (D) of hydrogen in $Ni(OH)_2$/NiOOH phases can be determined. A variety of measurement methods have been applied so far to determine the value of D for Ni and $Ni(OH)_2$ electrodes such as CV curve fitting or peak current analysis as a function of scan rate [107,135,204-210], current transient analysis [107,209,211-216], EIS [111,136,176,190], potential transient methods [117,217-219], charging curves with active material utilization analysis [220-222], and spectroscopic methods [107]. The reported values of D

vary depending on the electrode material and the preparation methods. In the case of metallic Ni electrodes, the reported D values are in the range of 10^{-8} – 10^{-12} cm^2 s^{-1}, while for $Ni(OH)_2$ electrodes the D values are in the range of 10^{-7} – 10^{-13} cm^2 s^{-1} [107,136,176,223]. Apart from other factors, the D values depend on the presence of additives, such as Co, Zn, Al, etc. [111,117,208-221,224,225]. The reported values of D could be compared with the diffusion coefficients of oxygen and hydrogen in nickel. The D values for oxygen and metal vacancies in $Ni(OH)_2$ film were reported to be on the order of 10^{-20} – 10^{-21} cm^2 s^{-1} [227]. The range of D values for oxygen is significantly smaller than the proton diffusion coefficient reported above for $Ni(OH)_2$/NiOOH redox couple. Alternatively, the reported D values for hydrogen in nickel is on the order of 10^{-6} – 10^{-7} cm^2 s^{-1} and strongly depends on the amount of absorbed hydrogen and on the structure of nickel [227-230]. These values are closer to the ones reported for $Ni(OH)_2$ and Ni electrodes, which supports the proposal that the species which diffuses during the oxidation of the $Ni(OH)_2$/NiOOH redox couple is the proton rather than oxygen containing species. For nickel hydroxide electrodes, it was found that the proton diffusion process depends on the size of $Ni(OH)_2$ grains [117], crystallographic form of $Ni(OH)_2$ [211], oxidation state of Ni(II) [190,207,219-222] and degree of conversion of $Ni(OH)_2$ to NiOOH, usually referred to as the state of charge (*SOC*) [220-222]. The reported activation energy values for the proton diffusion in $Ni(OH)_2$ electrodes are in the range of 9 – 21 kJ mol^{-1} [216,219,223].

In this study, we report new experimental results and theoretical analysis for the oxidation and reduction of the $Ni(OH)_2$ surface compound that resides on a metallic Ni electrode. We applied CV and CA techniques under well–defined polarization potential

(E_p), polarization time (t_p) and temperature (T) conditions, namely $1.5 \leq E_p \leq 1.6$ V, $0 \leq t_p \leq 3600$ s and $278 \leq T \leq 348$ K.

6.2 Results and Discussion

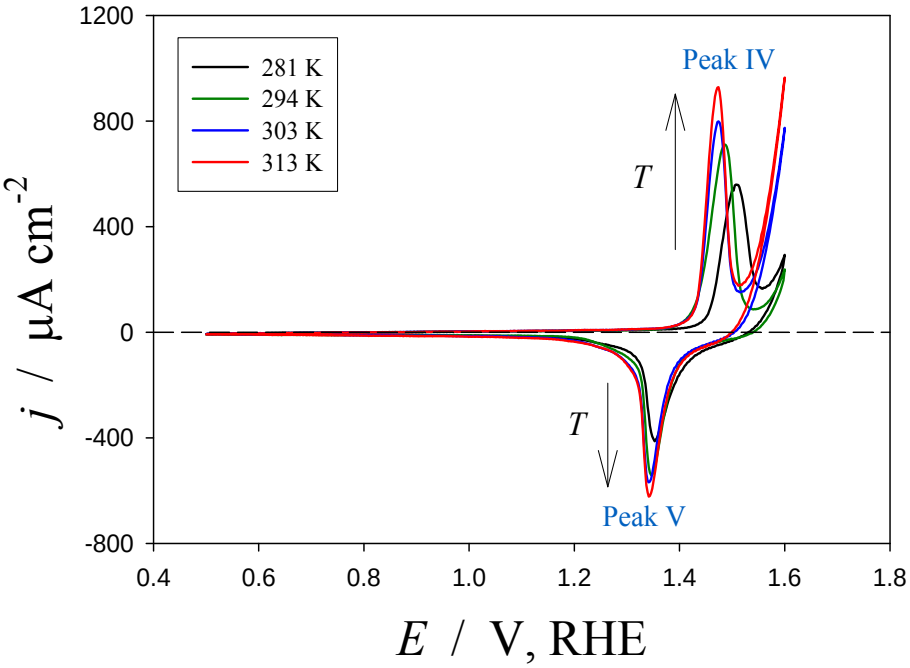

Figure 6.1a. Series of CV oxide formation and reduction profiles for Ni electrode in 0.5 M aq. KOH recorded at T = 289, 299, 304, and 313 K, for E_p = 1.6 V and v = 100 mV s^{-1}.

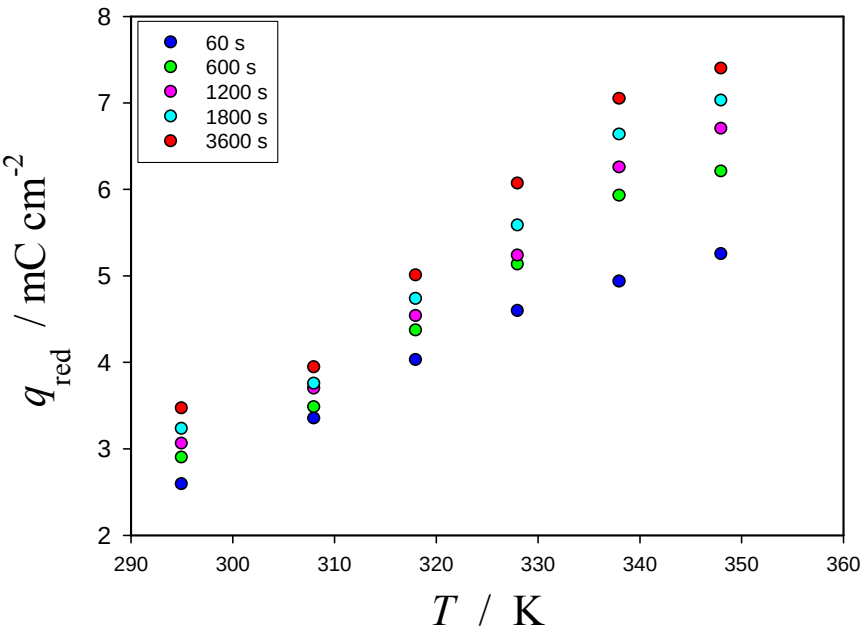

Figure 6.1b. q_{red} vs. T relation for Ni electrode recorded at E_p = 1.50 V and v = 50 mV s^{-1} for different polarization times, t_p, namely 60, 600, 1200, 1800, and 3600 s.

In Fig. 6.1a, we present a series of CV oxide formation and reduction profiles for Ni electrode in 0.5 M aq. KOH recorded for the following experimental conditions: 0.5 ≤ E_p ≤ 1.55 V, 293 ≤ T ≤ 348 K and v = 100 mV s^{-1}. We observe that an increase in temperature increases the charge density of the anodic and cathodic peaks (peaks IV and V). This process is accompanied by a shift of both peaks towards less–positive potential values, but the shift for the cathodic peak is significantly smaller than for the anodic one. A negative shift in potential of both the anodic and cathodic peaks has already been reported for the $Ni(OH)_2$ electrode [140], but the shift was similar for the two peaks. Slightly different results reported elsewhere [231] show that increasing the temperature shifts the anodic peak towards more positive potential with only a small increase in the charge of the cathodic peak. The results shown in Fig. 6.1b illustrate the relation between

the charge density of the reduction peak (q_{red}) and T for Ni electrode recorded at E_p = 1.50 V, v = 50 mV s^{-1} and for different t_p values, namely 60, 600, 1200, 1800, and 3600 s. We observe that as T is increased gradually from 293 to 348 K, q_{red} increases from 3.47 to 7.40 mC cm^{-2}, corresponding to a two–fold increase in the oxide thickness. In addition, the oxide charge density increases upon extension of polarization time, we observe that q_{red} increases from 5.25 to 7.40 mC cm^{-2} as the value of t_p increases from 60 to 3600 s.

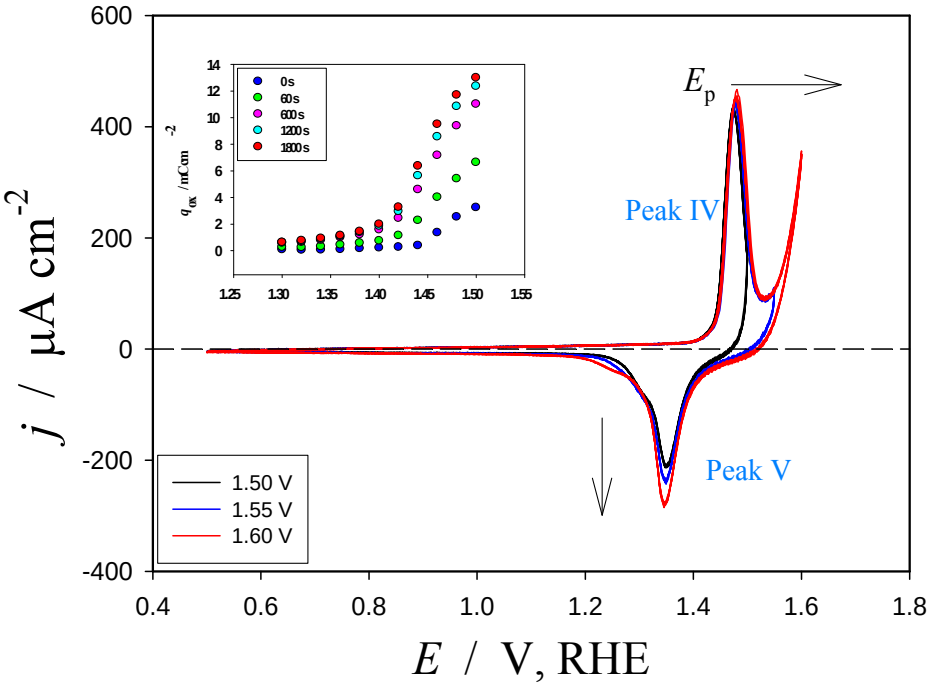

Figure 6.2. Series of CV oxide–reduction profiles for Ni electrode in 0.5 M aq. KOH recorded at E_p = 1.5, 1.55, and 1.6 V for T = 277 K, and v = 100 mV s^{-1}. q_{ox} vs. E_p relation is presented in the inset.

Figure 6.2 shows a series of CV oxide formation and reduction profiles for the Ni electrode in 0.5 M aq. KOH recorded at T = 277 K, v = 100 mV s^{-1} and for three different values of E_p, namely 1.50, 1.55, and 1.60 V. An increase in the area of the reduction peak

is observed with the extension of the polarization potential towards more positive values. Thus, as the potential increases, the oxide layer formed on Ni electrode becomes thicker. The potential of the peak V is not shifted as a result of the increase in the polarization potential. In the inset of Fig. 6.2, we show the q_{red} vs. E_p relation for different polarization times in the $0 \leq t_p \leq 1800$ s range. We observe that the q_{ox} increases with the extension of the polarization potential towards higher values. The same effect is also observed as the value of t_p increases indicating that the oxide formed has become thicker as E_p and/or t_p increases. A wave or poorly–defined peak starts to develop at a potential lower than that of the peak V (such a wave is also observed for low scan rates measurements). The wave was discussed in [13,140] and attributed to the reduction of various forms of NiOOH. Electrochemical quartz–crystal microbalance (EQCM) data shows that this potential wave is accompanied by a mass change [106]. The nature of this potential wave is beyond the scope of this discussion. Here we wish to focus only on the analysis of the main anodic and cathodic peaks.

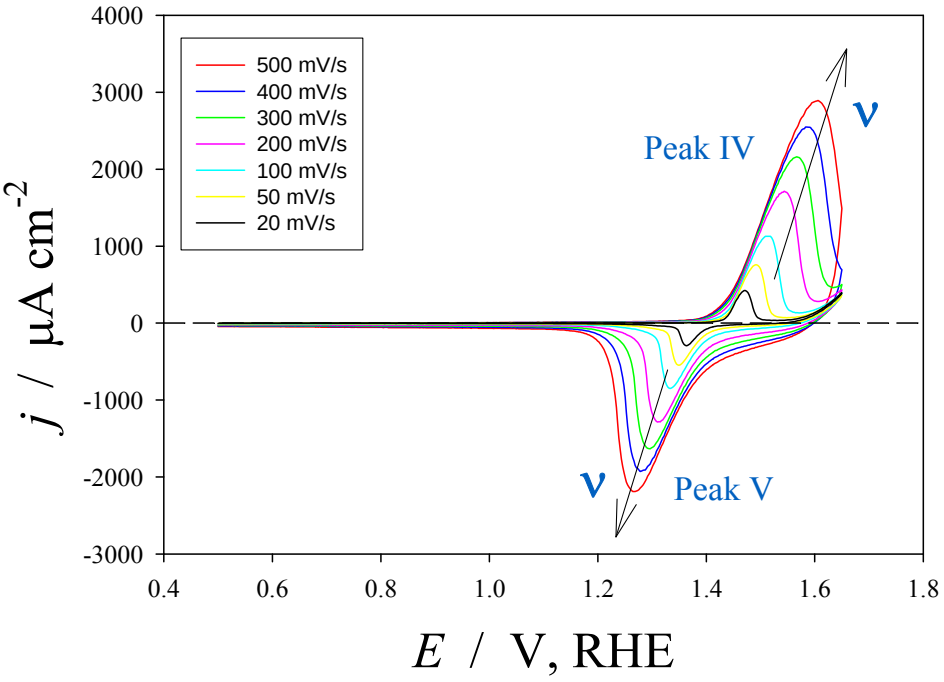

Figure 6.3. Series of CV oxide–reduction profiles for Ni electrode in 0.5 M aq. KOH recorded at $20 \leq \nu \leq 500$ mV s^{-1} for $T = 294$ K, and $E_p = 1.65$ V.

Figure 6.3 shows a series of CV oxide formation and reduction profiles for the Ni electrode in 0.5 M aq. KOH recorded at $E_p = 1.65$ V, $T = 294$ K and at $20 \leq \nu \leq 500$ mV s^{-1}. The increase in ν shifts the anodic peak (IV) towards more positive potential values, while the cathodic peak (V) is shifted in the opposite direction, leading to an increase in the separation between the two peaks. It is known that for irreversible oxidation and reduction processes, the separation of the anodic and cathodic peaks increases with the increase in the scan rate according to Randles–Sevcik equation (Eq. 6.1 in the following section) [107]. The influence of scan rate on the peak potential for Ni and $Ni(OH)_2$ electrodes has been reported elsewhere [140,205]. We observe that the scan rate does not change the shape of the anodic peak IV and induces only a potential shift. The data presented in Figs. 6.1, 6.2 and 6.3 shows that the current due to the oxygen evolution

reaction (OER) is practically zero and does not obscure the shape and the charge density of the peak V. Thus, the influence of OER on the reduction current of NiOOH is negligible.

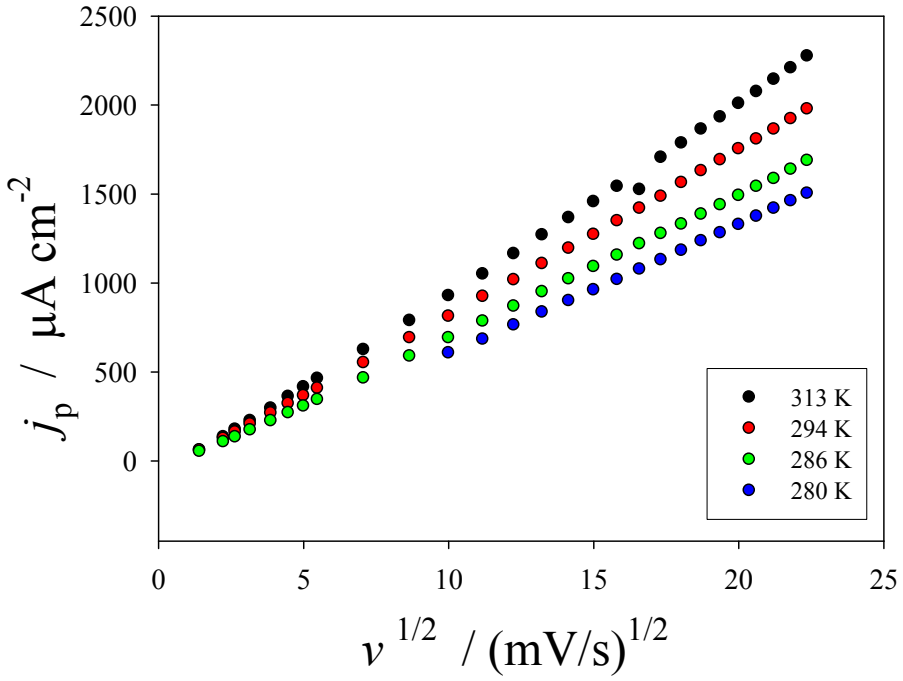

Figure 6.4a. Anodic peak current, j_p vs. $v^{1/2}$ plots for NiOOH reduction in 0.5 M aq. KOH recorded at E_p = 1.6 V, and at different T values, namely 280, 286, 294, and 313 K.

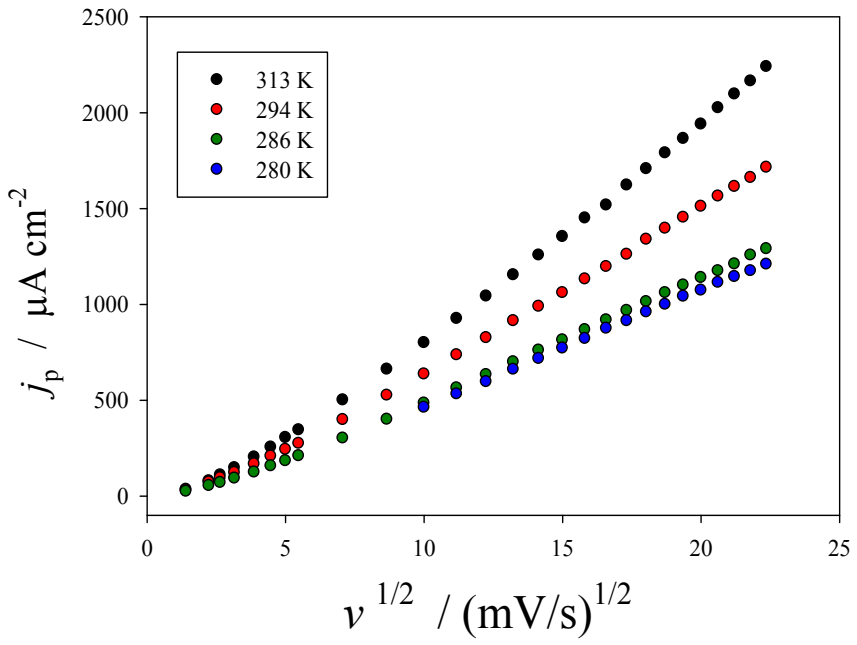

Figure 6.4b. Cathodic peak current, j_p vs. $v^{1/2}$ plots for NiOOH reduction at the same parameters presented in Fig. 5a.

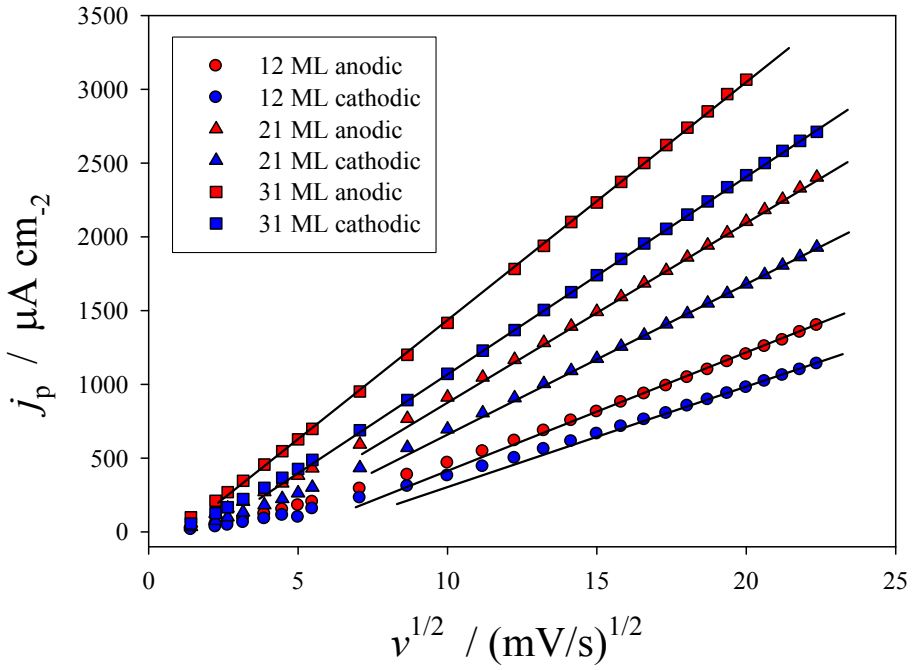

Figure 6.4c. j_p vs. $v^{1/2}$ plots for NiOOH anodic and cathodic currents in 0.5 M aq. KOH recorded for different thickness, namely 12, 21, and 31 ML at E_p = 1.6 V, T = 294 K, and v from 5 up to 500 mV s^{-1}.

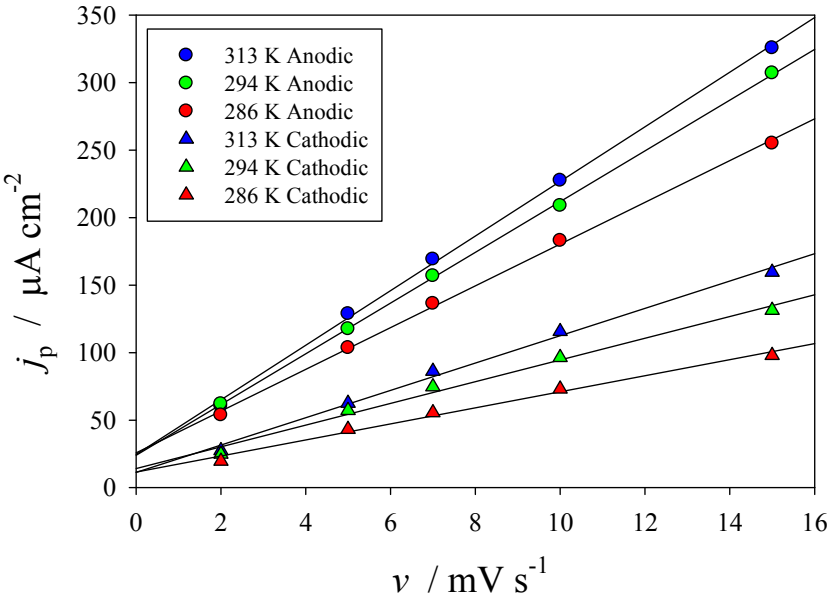

Figure 6.4d. j_p vs. v plots for NiOOH anodic and cathodic currents in 0.5 M aq. KOH recorded at E_p = 1.6 V, and at different T values, namely 286, 294, and 313 K.

Figure 6.4a shows j_p vs. $v^{1/2}$ relations for the peak IV (growth of NiOOH oxide) for the Ni electrode in 0.5 M aq. KOH recorded at $280 \leq T \leq 313$ K, $5 \leq v \leq 500$ mV s^{-1} and E_p = 1.6 V. In Fig. 6.4b, we show j_p vs. $v^{1/2}$ relations for the peak V at the same parameters. We observe a linear j_p vs. $v^{1/2}$ dependence that becomes well–defined at higher scan rates, c.a. $\geq$ 75 mV s^{-1}. The linear relation is observed for the entire range of T and for different thickness of the oxide layers. This linear dependence has been previously reported for metallic Ni electrodes, $Ni(OH)_2$ electrodes, doped $Ni(OH)_2$ electrodes and Ni alloys [107,204-208,210]. In the case of the cathodic process, the linear region starts at slightly higher values of v than the anodic peak. Furthermore, the slope of j_p vs. $v^{1/2}$ relation is smaller for the cathodic process than for the anodic one. For both peaks, we observe that the slope of the j_p vs. $v^{1/2}$ relations increases with increase of T and an extrapolation of the linear region does not pass through the origin. When the absolute value of j_p is plotted,

the intersection with the current density axis is always negative. The non–zero intersection of the j_p vs. $v^{1/2}$ relations with the current density axis is also reported for Ni electrodes, Ni-Cu alloys and $Ni(OH)_2$, but has not been discussed in any of these contributions [107,204,206,208]. A similar effect was also observed for other systems, e.g. $Co(OH)_2$ electrodes [232]. The data presented in Fig. 6.4c show the j_p vs. $v^{1/2}$ relations for the anodic and cathodic peaks for Ni electrode in 0.5 aq. M KOH recorded at E_p = 1.6 V, T = 294 K, $5 \geq v \geq 500$ mV s^{-1} and for different oxide thicknesses (d), namely 12, 21, and 31 monolayers (ML). The increase in the oxide thickness is achieved through continuous CV cycling of the electrode in the potential range of Ni(III) formation and reduction [140]. An increase of the oxide thickness improves the linearity; i.e. the linear region becomes wider as d increases. This behavior resembles the one expected by the semi–infinite diffusion model. Figure 6.4d illustrates the j_p vs. v relation for NiOOH anodic and cathodic currents in 0.5 M aq. KOH recorded at E_p = 1.6 V, and at different T values, namely 286, 294, and 313 K. A linear relation is observed between j_p and v for low scan rate values as expected according to the finite–length diffusion model. These models are discussed in detail in a later section. Figure 6.5 shows the result of increasing the oxide thickness on the slope of the j_p vs. $v^{1/2}$ relations. A departure from linearity is observed at a thickness of ca. 30 ML that could be attributed to the limitation of the proton diffusion in thicker hydroxide/oxide layers.

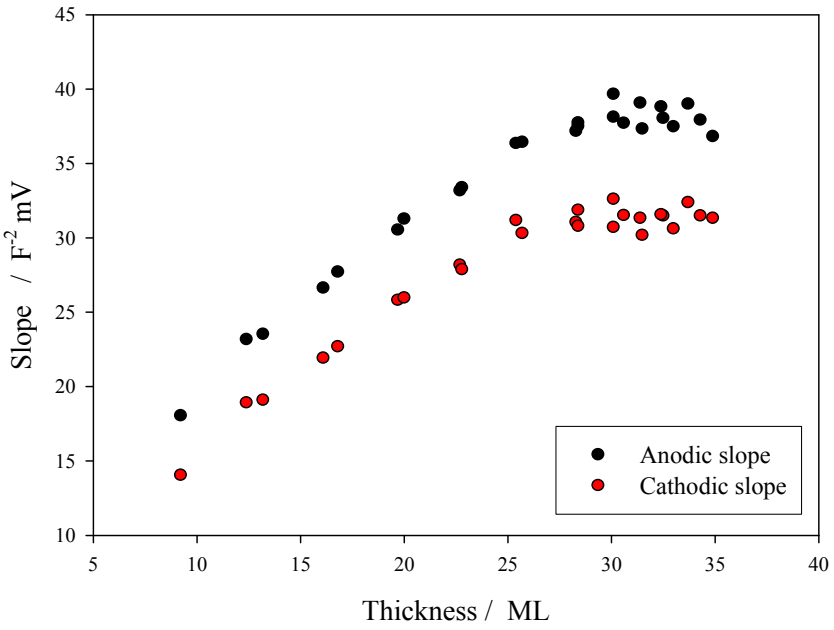

Figure 6.5. Influence of the Ni oxide thickness on the slope of the j_p vs. $v^{1/2}$ relation (anodic and cathodic) calculated on the basis of Fig 6.4c.

6.3 Chronoamperometry Analysis

The data presented in Fig. 6.6 show a series of CA profiles for the Ni electrode in 0.5 M aq. KOH recorded at E_p = 1.5 V and 278 ≤ T ≤ 308 K. The inset of Fig. 6.6 shows CA curves recorded at T = 293 K and for two different values of E_p, namely 1.48 and 1.50 V. As expected, the value of j_p increases as T is increased.

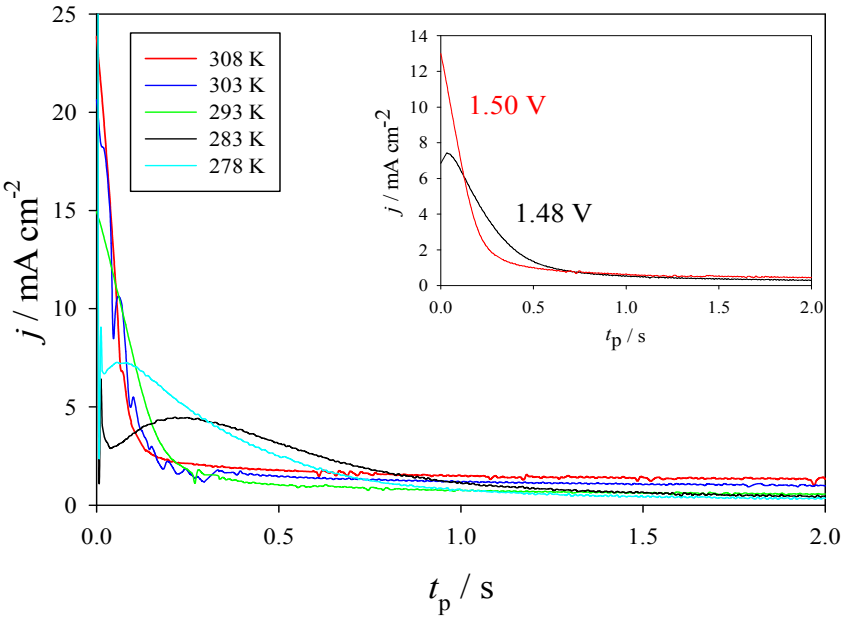

Figure 6.6. $j - t_p$ relation for the Ni electrode in 0.5 M aq. KOH recorded at E_p = 1.5 V, 0 $\leq t_p \leq$ 2 s and 278 $\leq T \leq$ 308 K. The inset shows the j vs. t_p relation at T = 298 K for two values of E_p, 1.48 and 1.50 V.

We observe a current density peak which could be attributed to the nucleation–and–growth process [233]. This peak is observed only for low temperatures and for lower potential values. The latter condition can be attributed to the influence of the electrode potential on the number of nuclei formed, an effect which is widely observed in many nucleation processes [233,234]. This nucleation peak appears only if the electrode has previous been reduced at sufficiently less positive potentials (below 0.5 V). The rising part of the peak is ascribed to the formation and growth of nuclei, while the descending part is attributed to the growth of the nuclei through a diffusion–limiting process. We also observed a linear region in the CA curves at different values of E_p and T, which suggests that this process is limited by diffusion of the reacting species [233]. A finite–length

diffusion model can be applied to explain the linearity of j_p vs. t_p relation using Randles–Sevcik equation [107,235]:

$$j = 4nFADC_b d^{-1} \exp\left(\frac{-\pi^2 D t_p}{d^2}\right) \quad (6.1)$$

where n is the number of electrons transferred in the process, F is Faraday's constant, A is the geometric surface area of the electrode, D is the diffusion coefficient, C_b is the bulk concentration of the diffusing species, and d is the thickness of the oxide layer. The data presented in Fig. 6.7 show the ln j_p vs. t_p relation for the Ni electrode in 0.5 M aq. KOH recorded at t_p = 2 s, E_p = 1.5 V and 278 ≤ T ≤ 308 K. At larger t_p values, a departure from the linearity is observed indicating that the simple model of Randles–Sevcik equation cannot explain the entire diffusion process [107,223]. It is reasonable to assume that this departure from linearity after a short time indicates the existence of at least two processes of Ni(II) oxidation: a fast process for a very short time represented by the fast current density decay (linear ln j_p vs. t_p region), followed by a slow process represented by the slow current density decay (departure from linearity).

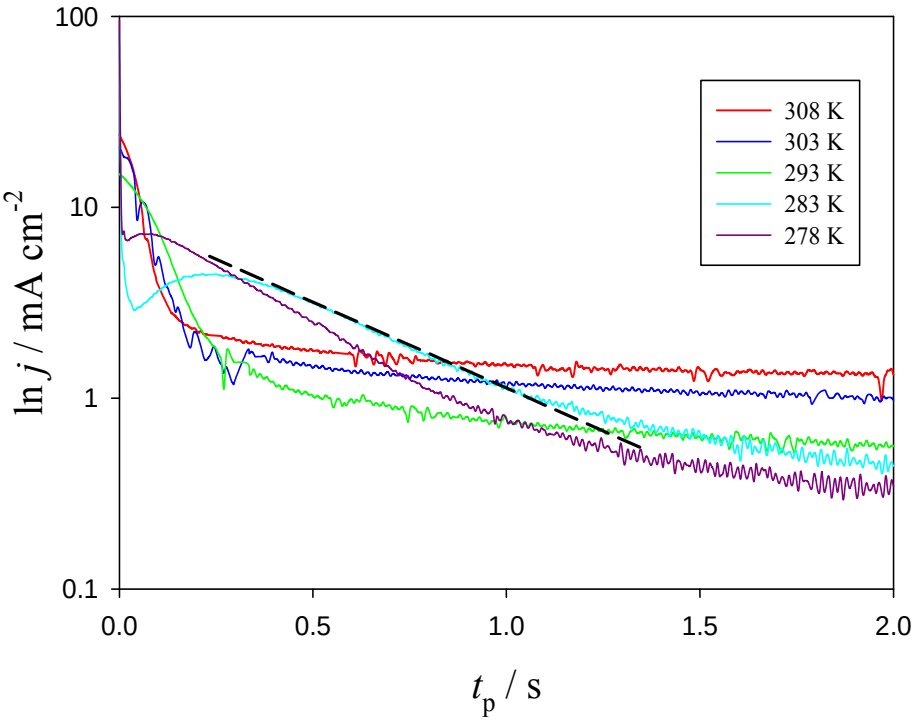

Figure 6.7. Semi–logarithmic $I - t_p$ relation for Ni(II) oxidation showing a linear decay recorded at $E_p = 1.5$ V, $0 \leq t_p \leq 2$ s, and for various temperatures, namely $T = 278$, 283, 293, 303 and 308 K.

6.4 Peak Current vs. Scan Rate Relation

The data presented in Figs. 6.3 and 6.4 indicate that the β-$Ni(OH)_2$/NiOOH redox couple is electrochemically irreversible and follows the Randles–Sevcik equation. Additionally, oxidation of β-$Ni(OH)_2$ and the subsequent reduction of NiOOH is a diffusion–controlled process. The results recorded in quiescent solution are consistent with those obtained for N_2 stirred solutions. Thus, we can assume that the rate determining diffusion process takes place inside the solid phase (i.e. Ni(II) and/or NiOOH) and not in the solution. The lack of influence of solution mixing on the oxidation of NiCu alloys was reported in [204]. The smaller slope of j_p vs. $v^{1/2}$ relation

was reported for the cathodic process and attributed to the dependence of the diffusion on the electrode composition (*SOC* effect) [204,207]. Asymmetry of D values for the formation and reduction of NiOOH was also reported for $Ni(OH)_2$ electrodes with $D_{NiOOH} > D_{Ni(OH)_2}$ [190,219-222]. It is assumed that the oxidation of $Ni(OH)_2$ and the reduction of NiOOH takes place at the oxide–electrolyte interface and grows toward the bulk of the electrode [190,225]. In this case, different values of D are expected for the diffusion of the proton in the pure $Ni(OH)_2$ and NiOOH phases. When a mixture of the two phases exists, the diffusion coefficient value is then a function of the NiOOH/$Ni(OH)_2$ ratio [150,225]. According to Eq. 6.1, for cathodic processes, a smaller slope suggests a smaller value of D for protons diffusing in the NiOOH oxide (during the reduction of NiOOH). The reported values of D are smaller for the NiOOH discharge by two orders of magnitude [221].

The departure from linearity and the non–zero intercept with the current density axis (see Figs. 6.4) requires further discussion. The non–linear region of the j_p vs. $v^{1/2}$ relation at low scan rates can be analyzed using the finite–diffusion model. In this model, a linear relation between j_p and v is predicted [236]. Aoki et al. [237] developed a general theory for the j_p vs. v relation for a broad range of potential scan rate values. This theory has been applied to study the intercalation process and charge transfer in polymer layers [238-240]. According to this model, the linear relation depends on the thickness of the diffusion layer (d) and the scan rate (v); at higher values of v and/or d, a semi–infinite diffusion model is expected. Thus, for higher values of d^2v, a linear relation between j_p and $v^{1/2}$ is expected, while at lower d^2v values, a linear relation between j_p and v is

expected, see Figs. 6.4. For high scan rates and irreversible processes, the semi–infinite diffusion model is described by the following equation [235,237]:

$$j_{\mathrm{p}} = 5.155 \times 10^{6} n A T^{-1/2}\, C_b\, (\alpha n_{\alpha} D)^{1/2} v^{1/2} \qquad (6.2)$$

where n is the total number of electrons exchanged in the process, n_{α} is the number of electrons passed in r.d.s., A is the electrode surface area, D is the diffusion coefficient and C_b is the bulk concentration of the diffusing species. Although the formation of Ni_2O_3 during the oxidation of $Ni(OH)_2$ has been reported, it is usually assumed that $n_{\alpha} = n = 1$ for the oxidation of $Ni(OH)_2$ at ambient temperature [241]. Moreover, the theory of finite–length diffusion indicates that the increase in v and/or d creates conditions of semi–infinite diffusion [237]. In general, the thicker the oxide/hydroxide layer, the wider the linear range of the j_{p} vs. $v^{1/2}$ relation. However, this theory predicts that the j_{p} vs. $v^{1/2}$ linear region must cross the current density axis at the origin. From the results displayed in Figs. 6.4, the intersection with the current axis is non zero and is weakly affected by the thickness of NiOOH oxide. If we assume that an increase in NiOOH layer thickness mirrors the increase in the overall Ni(II) thickness [242], we can conclude that the intersection is practically thickness independent. The non–zero intercept of j_{p} vs. $v^{1/2}$ relation, which is positive for j_{anodic} and negative for j_{cathodic}, was attributed to the influence of electrode surface roughness [243]. Kulesza et al. attributed the non–zero intercept to the drop in potential due to the migration of the charged species or the limitation in charge propagation [244]. In addition, theory of microelectrodes also predicts a non–zero intercept of the j_{p} vs. $v^{1/2}$ relation [245]. However, those theories are

not applicable in our case as we obtained only a negative value for the intercept for both the anodic and the cathodic current densities. Similar behavior to these negative intercept has been reported for both currents in the literature for nickel based electrodes [107,204,206,208]. Thus, this effect cannot be attributed to the experimental data scatter. The possible cause for the non–zero intercept could be attributed to one or a combination of the following: (i) hydrogen trapping, (ii) influence of the electric field or (iii) an effect of the oxide composition. In our case, the latter is most likely the reason of the non–zero intersection. Therefore, in the following section, only the effect of the oxide composition is discussed while the first two cases are discussed in the Appendix.

6.4.1 Effect of the Oxide Composition

It is well known that the D values are different for $Ni(OH)_2$ than for NiOOH layers, and the total diffusion coefficient (effective diffusion) is a function of $D_{Ni(OH)2}$ and D_{NiOOH} values [190,207,219-222]. Influence of the state of charge on the value of the effective (measured) H^+ diffusion coefficient can be described by the following equation [190,212,217,246]:

$$D_{eff} = D_1 \left[SOC + \left(\frac{D_2}{D_1}\right)^{1/2} (1 - SOC) \right]^2 \qquad (6.3)$$

where D_1 and D_2 are the diffusion coefficient of H^+ in NiOOH and $Ni(OH)_2$, respectively. This equation is evaluated with an assumption of parallel diffusion of H^+ in the two media (D_1 and D_2). From the equation, an increase in the value of D_{eff} with the progress

of $Ni(OH)_2$ oxidation to NiOOH is expected. In previous sections of this study, we determined the D values on the basis of j_p vs. $v^{1/2}$ relationships (Eq. 6.1). Such determined D values are for a constant diffusion coefficient which does not change with the progress in oxidation. This is in contrast to Eq. 6.3 which shows that the D_{eff} changes continuously with progress in oxidation (small values of D_{eff} when only $Ni(OH)_2$ layer exist on the electrode surface and slightly increases as the NiOOH formation takes place). The analysis of the influence of *SOC* on the D values obtained from the CV experiments requires the introduction of a parameter that describes the ratio of $Ni(OH)_2$ and NiOOH at the apex of the oxidation peak (where the concentration of the diffusing species equals zero). The *SOC* is defined here as a $M_{NiOOH}/M_{Ni(OH)_2}$ ratio, where M_{NiOOH} and $M_{Ni(OH)_2}$ are the amounts of NiOOH and $Ni(OH)_2$ layers present at the electrode surface, respectively. The amount of NiOOH electrochemically formed is determined by the charge transferred till the top of the oxidation peak (q_{ox1}). Knowledge of the $Ni(OH)_2$ layer thickness is required, however this thickness is constant during a single experiment. This is due to the fact that the oxidation rate of Ni is expected to decrease significantly for a thicker Ni(II) layer [150]. Thus, for relatively thick Ni(II) layers (31 MLs, see Fig 6.4c), knowledge of the $M_{Ni(OH)_2}$ thickness is trivial. In this case, changes in q_{ox1} mirrors the changes in *SOC* ($SOC = q_{ox1}/q_{Ni(II)}$).

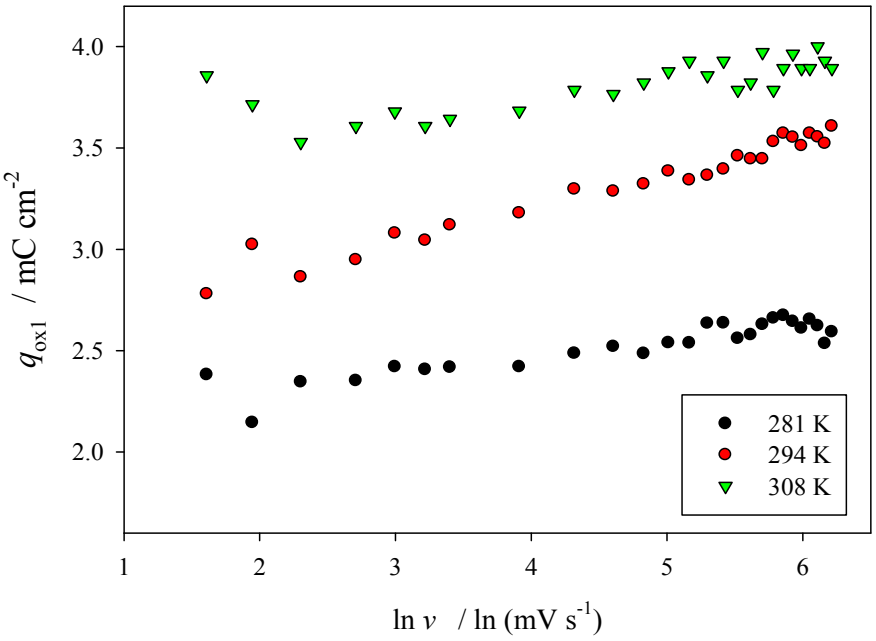

Figure 6.8. q_{ox1} vs. ln v relations for Ni electrode in 0.5 M aq. KOH recorded at various temperatures, namely T = 281, 294, and 308 K.

Figure 6.8 shows the relationship between q_{ox1} and ln v for the Ni electrodes in 0.5 M aq. KOH recorded at different T values, namely 281, 294 and 308 K. We observe an increase in q_{ox1} (reflects an increase in *SOC*) as the scan rate increases. According to Eq. 6.3, different values of *SOC* imply different values of D_{eff}. Thus, a small value of D_{eff} is expected before the NiOOH layer is established and a higher value of D_{eff} is expected as the formation of NiOOH takes place (the thicker the NiOOH layer, the higher the value of D_{eff}). The obtained values of D from Eq. 6.1 are not equal to D_{eff}, and a *SOC* parameter must be introduced to Eq. 6.1 in order to calculate the D_{eff}. It is important to note that the linear region in Fig. 6.8 is obtained for high values of v (the linear region of j_p vs. $v^{1/2}$ relation is also obtained for high v values, see Fig. 6.4). For a linear change of the *SOC* (directly proportional to q_{ox1}) with scan rates, the following equation is applied:

$$SOC = a + b \ln v \tag{6.4}$$

where a and b are empirical parameters. The relation between q_{ox1} and ln v can be obtained by multiplying *SOC* by $q_{Ni(II)}$. This equation is applicable when the q_{ox1} vs. ln v relation is linear (Fig. 6.8). Determination of *SOC* is possible only when the thickness of the $Ni(OH)_2$ layer is known, otherwise the parameters a and b remain unknown. Further discussion of Eq. 6.4 was made with the assumption that a linear relation between D_{eff} and *SOC* at the peak maximum exists. This is due to the fact that *SOC* value increases with the scan rates (Eq. 6.4). Thus, introducing Eq. 6.4 into Eq. 6.3, we can replace *SOC* with v and obtain a relation describing the influence of v on the measured D values:

$$D = D_1 [i + j \ln v]^2 \tag{6.5}$$

where $i = [a + (D_2/D_1)^{1/2}(1 - a)]$ and $j = b[1 - (D_2/D_1)^{1/2}]$. The D_1 and D_2 in this equation are D_{eff} for both processes, as discussed earlier. This equation is applicable to a range of v values where a linear q_{ox1} vs. ln v relation exists. Introducing Eq. 6.5 into Eq. 6.2 results in the following equation:

$$j_p = mD_1^{1/2} iv^{1/2} + mD_1^{1/2} jv^{1/2} \ln v \tag{6.6}$$

where $m = 5.155\text{x}10^6 nAT^{-1/2}C_b(\alpha n_\alpha)^{1/2}$. Equation 6.6 can be simplified by dividing both sides by $v^{1/2}$ and the final form of this relation is given by the following equation:

$$\frac{j_p}{v^{1/2}} = mD_1^{1/2} i + mD_1^{1/2}\, j \ln v = p + q \ln v \qquad (6.7).$$

Equation 6.5 indicates a linear relation between $j_p/v^{1/2}$ and ln v with a non–zero intercept which depends on *SOC*. The data in Fig. 6.9 show such determined $j_p/v^{1/2}$ vs. ln v relations for a nickel electrode in 0.5 M aq. KOH.

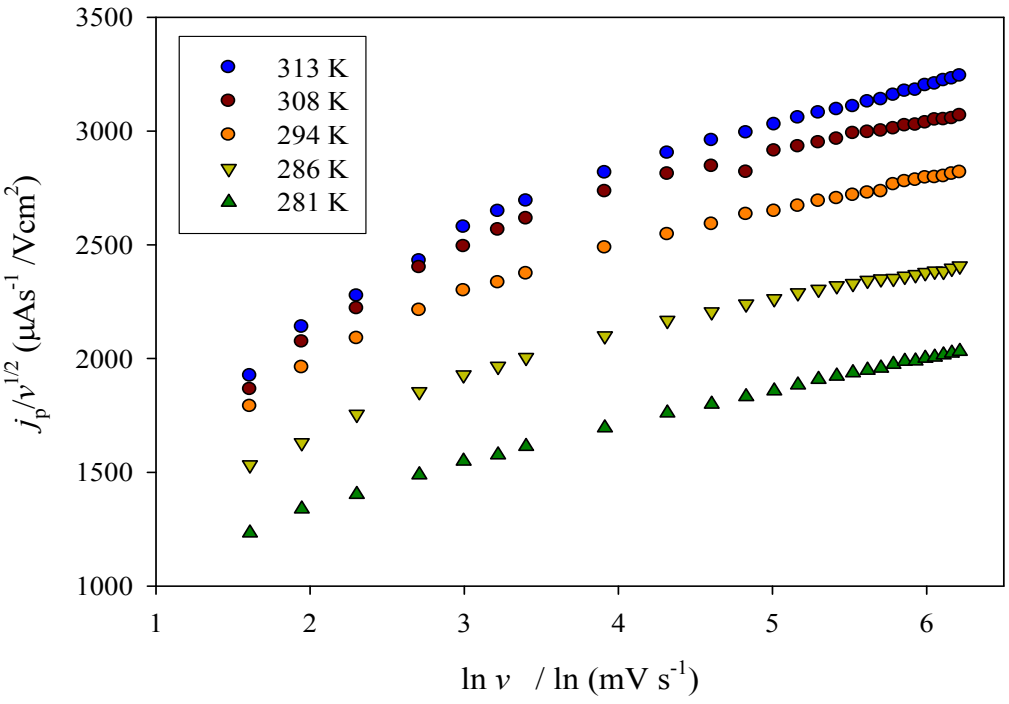

Figure 6.9. j_p / v relation as a function of ln v for Ni electrode in 0.5 M aq. KOH recorded at various temperatures, namely T = 281, 286, 294, 308 and 313 K (on the basis of Figs. 6.4, 6.8 and Eq. 6.4).

A linear relation between $j_p/v^{1/2}$ and ln v is observed for high values of v confirming the validity of the above discussed assumptions. This linear part begins at similar values of v (ln v = 3 ± 0.5 mV s^{-1}), and the linear regions of q_{ox1} vs. ln v and j_p vs.

$v^{1/2}$ as shown in Figs. 6.4 and 6.8, respectively. For thicker Ni(II)/Ni(III) layers, the linear region of the $j_p/v^{1/2}$ vs. ln v relation extends to almost the entire range of scan rates studied. This corresponds to an extension of the linear part of j_p vs. $v^{1/2}$ dependence on the thickness of Ni(II)/Ni(III) layer (see Fig. 6.4). Combining "*p*" and "*q*" values, it is possible to calculate the D_2/D_1 ratio and subsequently, each of these values separately. In order to accomplish this, however, the values of *a* and *b* must be known which requires detailed knowledge of the thickness of the $Ni(OH)_2$ layer for calculation of *SOC*. Although the thickness of the $Ni(OH)_2$ layer and the D_2/D_1 ratio cannot be determined from Fig. 6.9, the linearity in this relation qualitatively confirms the approach discussed in this study and indicates that introducing the term *SOC* in the cyclic voltammetry analysis is required. Further evaluation of equations used for peak current vs. scan rate analysis is required, especially for the explanation of the non–zero intercept observed in Fig. 6.4.

6.5 Influence of the Temperature on the CV Profiles

The slope of j_p vs. $v^{1/2}$ relation is temperature dependent (see Fig. 6.4), this dependence results not only from the term T^{-1} in Eq. 6.2, but is also due to the temperature dependence of *D* according to the following Arrhenius–like equation:

$$D = D_o \exp\left(\frac{-E_a}{RT}\right) \tag{6.8}$$

where E_a is the activation energy of diffusion and D_o is a constant (D at infinite temperature). In this case, the slope will increase with increasing temperature. Since we observe an increase in the slope of the j_p vs. $v^{1/2}$ plots with temperature in Fig. 6.4, we conclude that the dominant factor of the temperature dependence is the T parameter in Eq. 6.8 and not the $T^{-1/2}$ term in Eq. 6.2.

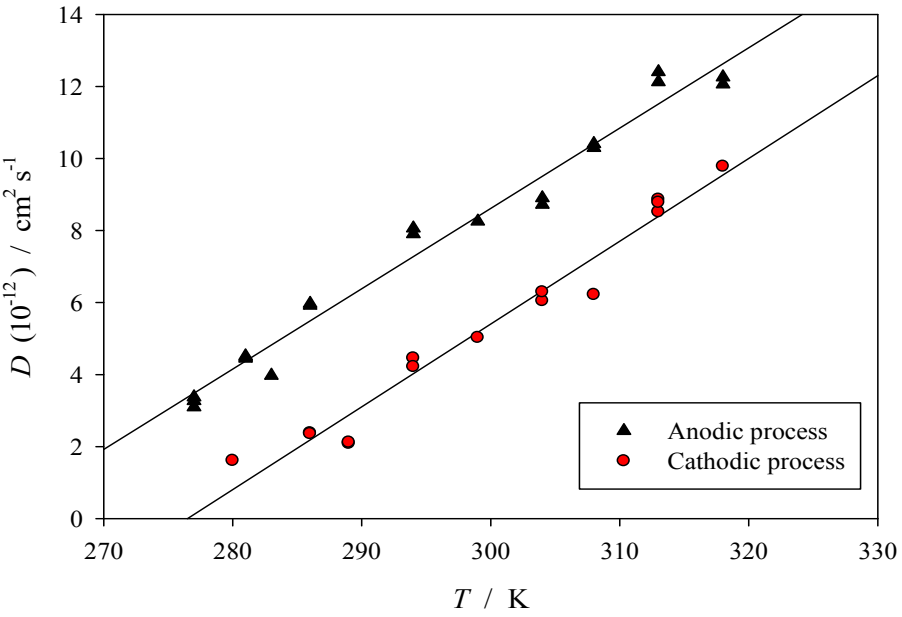

Figure 6.10. Diffusion coefficient, D, as a function of temperature for anodic and cathodic peaks calculated from Eq. 6.2.

Figure 6.10 shows the D vs. T relationship (calculated from Eq. 6.2) for anodic and the cathodic processes. At room temperature, such determined values of D are 8.1 ± 0.5 x 10^{-12} and 4.3 ± 0.2 x 10^{-12} cm^2 s^{-1}, for the anodic and cathodic processes, respectively. As it was mentioned earlier, the reported values of the diffusion coefficient for Ni and $Ni(OH)_2$ electrodes cover a wide range, namely from 10^{-7} to 10^{-13} cm^2 s^{-1}, with $D_{NiOOH} > D_{Ni(OH)2}$. The D values obtained in this study are smaller than those

reported for $Ni(OH)_2$ electrodes (including $Ni(OH)_2$ with added Co, Al, etc.) [21,111,136,190,205,213,219-221] and are also smaller than in the case of metallic Ni electrodes [136,176]. On the other hand, our *D* values are higher than those reported for $Ni(OH)_2$ electrodes [107,117,206,208,209,211,214,215,224] and comparable to those measured using CA, CV and spectroscopic methods for metallic Ni electrodes [107].

The discrepancy in *D* values could result from (i) differences in structure of NiOOH formed, (ii) different values for concentration used in Eq. 6.2 (calculated from different values of $Ni(OH)_2$ density) or (iii) different thickness of $Ni(OH)_2$/NiOOH layers. The densities of α-$Ni(OH)_2$ and β-$Ni(OH)_2$ differ, therefore different values of C_b could be introduced into Eq. 6.2. When the density of α-$Ni(OH)_2$ is used, the values of *D* calculated are ca. 3 times higher than when they are calculated using the density of β-$Ni(OH)_2$. This, however, will not affect the values of activation energy obtained as long as the proton concentration and $Ni(OH)_2$ density are considered temperature independent in the *T* range of interest.

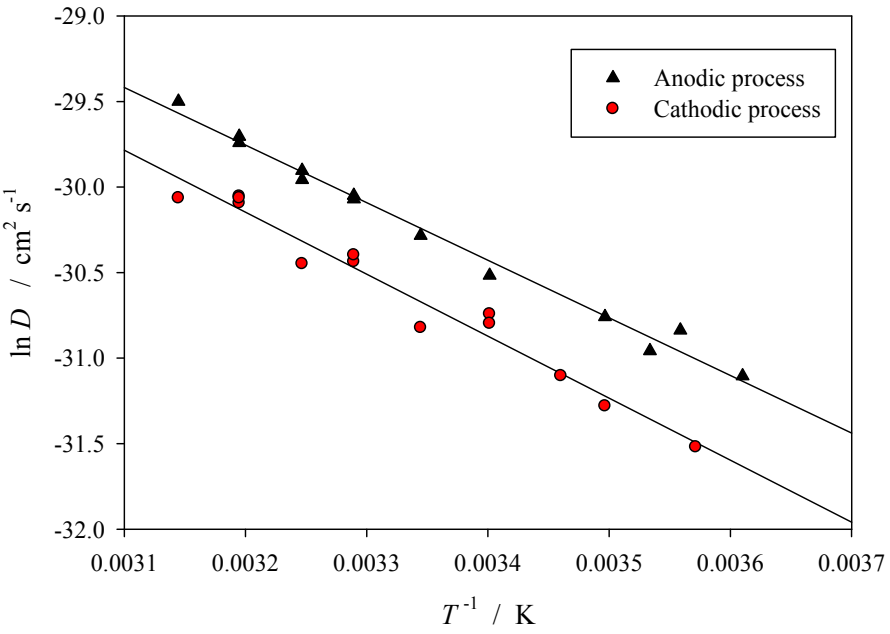

Figure 6.11. Arrhenius–like ln D vs. T^{-1} relation for the diffusion coefficient values presented in Fig. 13.

In Fig. 6.11, we present the Arrhenius–like ln D vs. T^{-1} relationship for Ni electrodes in 0.5 M aq. KOH recorded at $277 \leq T \leq 313$ K for the anodic and the cathodic processes. A linear relation between ln D and T^{-1} is observed for the anodic and the cathodic processes. This linearity indicates that the activation energy and the pre–exponential factor, in Eq. 6.8, could be considered temperature independent in this temperature range. Such obtained E_a values are 23 ± 2 and 26 ± 2 kJ mol^{-1} for the anodic and the cathodic processes, respectively. The difference between these values lies within the accepted experimental error range indicating that E_a could be considered the same for the oxidation of β-Ni(OH) and the reduction of NiOOH. There is no literature data for E_a of the proton diffusion in $Ni(OH)_2$/NiOOH oxides formed on metallic Ni electrodes. The only data available is for nickel hydroxide electrodes, which have D values slightly

smaller than those obtained in this study. The reported values of E_a are 7.8 – 19 kJ mol^{-1} for Co–doped Ni hydroxide, 9.2 – 20.9 kJ mol^{-1} for $Ni(OH)_2$ oxidation, and 13.4 kJ mol^{-1} for the reduction of NiOOH electrode [117,216,219]. The range of the activation energy values obtained in this study is very small compared to the reported E_a values (23 – 26 kJ mol^{-1}). The small difference in E_a values for the anodic and cathodic processes suggests that the activation energy value for the β-$Ni(OH)_2$ oxidation is the same as that for the NiOOH reduction. Thus, the difference in D values, for the cathodic and the anodic process, must be due to a difference in the value of the pre–exponential factor in Eq. 6.8 or a difference in the concentration of the proton used in the calculation of Eq. 6.2.

Comparison of our results for smooth, metallic Ni electrodes to the literature data for $Ni(OH)_2$ electrodes suggests that the compactness of the $Ni(OH)_2$ structure seems to play a significant role in the proton diffusion process. The values of activation energy obtained in this study for metallic Ni electrodes are slightly higher than those reported in the literature for $Ni(OH)_2$ electrodes. If we assume a less compact structure with more defects in the $Ni(OH)_2$ layer (i.e. containing incorporated anions during the deposition), it is likely that the diffusion of the proton would be further inhibited than in a more compact structure of $Ni(OH)_2$/NiOOH formed on solid, smooth metallic Ni electrodes.

6.6 Chronoamperometric analysis

Chronoamperometric curves were analyzed on the basis of the finite–length diffusion model by applying several parallel diffusion pathways according to the following equation [235]:

$$I_{para} = \sum_{i=l}^{N} I_{\text{oi}} \exp(-\tau_i t) + I_{\text{ox}} \qquad (6.9)$$

where I_{para} is the number of the parallel processes, I_{ox} is the oxygen evolution current (time independent), I_{oi} and τ are the pre–exponential and the exponential terms from Eq. 6.1 ($I_{\text{ox}} = 4nFADC_b d^{-1}, \tau = \left(\frac{-\pi^2 D t_p}{d^2}\right)$). The above equation is a sum of parallel currents, each one is represented by Eq. 6.1. The best non–linear least square (NLS) fitting is obtained for three parallel processes (E_{a} is the same for all). The data in Fig. 6.12 present an example of the NLS fits of Eq. 6.9 with the CA profiles for Ni electrode in 0.5 M KOH recorded at E_{p} = 1.5 V and T = 288 K. The inset of Fig. 6.12 shows CA profiles at the same parameters but at T = 303 K.

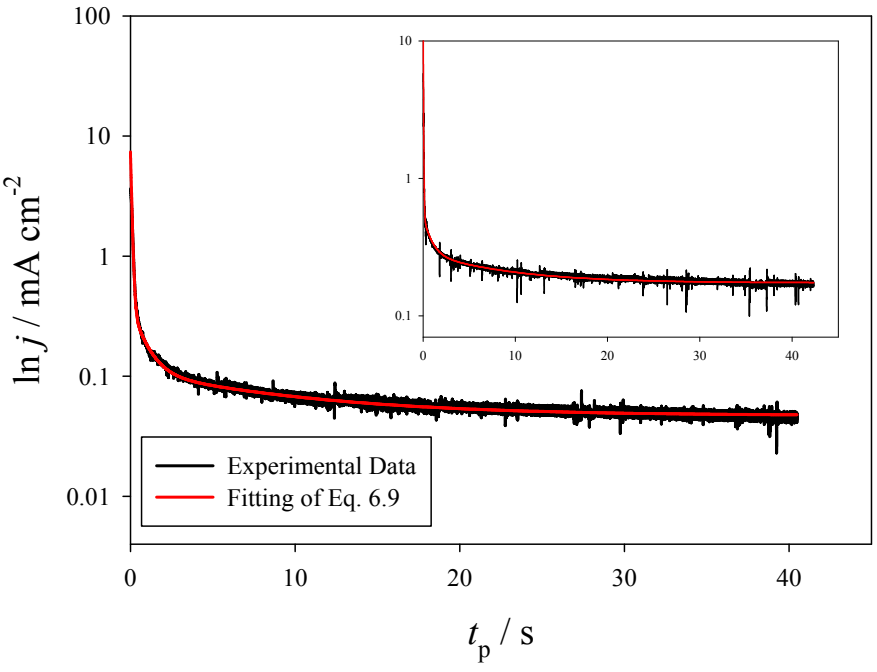

Figure 6.12. ln j vs. t_{p} relation for Ni electrode in 0.5 M aq. KOH showing the NLLS fits (red line) to Eq. 6.9 recorded at E_{p} = 1.5 V and at T = 288 K. The inset shows the same relation at T = 303 K.

The NLLS fit of Eq. 6.9 fits the data for relatively short oxidation times as well as for longer oxidation times (up to a few tens of seconds). The three parallel diffusion processes detected on the basis of CA curve–fitting are denoted here as D_1, D_2, and D_3. In Figs. 6.13 and 6.14, we present the relation of D vs. T and ln D vs. T^{-1} for the three diffusion processes.

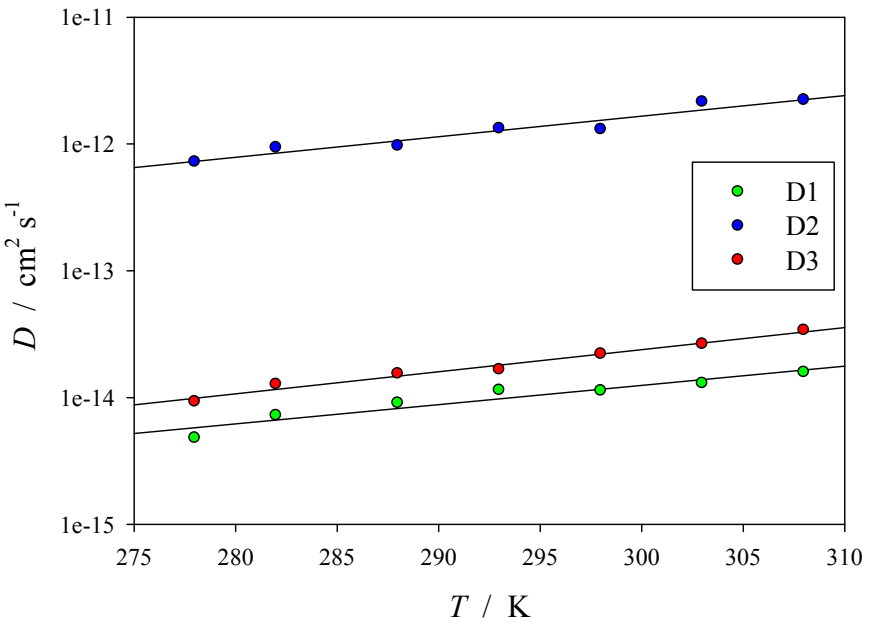

Figure 6.13. Diffusion coefficients (D) as a function of temperature obtained by fitting of CA curves in Fig. 15 for three parallel processes of Ni(II) oxidation, namely $D1$, $D2$, and $D3$.

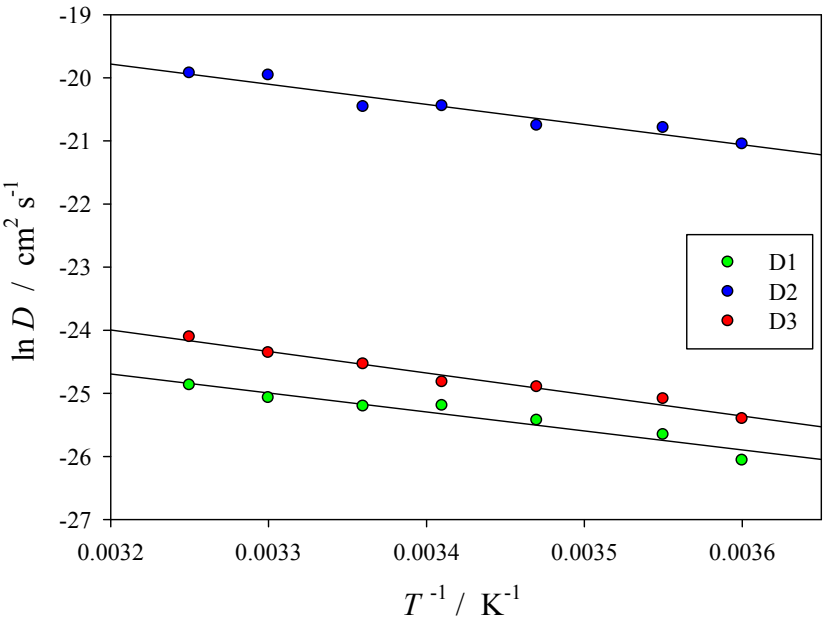

Figure 6.14. Arrhenius–like ln D vs. T^{-1} relation for diffusion coefficient processes presented on Fig. 6.10.

The highest values of D obtained are in the range of 10^{-12} – 10^{-13} cm^2 s^{-1} and are comparable to the D values obtained from the CV experiments (Fig. 6.10). For the other two processes, the obtained D values are significantly smaller and in the range of 10^{-14} – 10^{-15} cm^2 s^{-1}. Although the values of D_1 and D_3 are close and apparently can be treated as one process, separation of these two processes gives an enhanced fit to Eq. 6.9. This is due to the fact that the pre–exponential and exponential factors in Eq. 6.1 and 6.9 depend not only on the D values, but also on the thickness of the diffusion layer which varies significantly for both processes. The D_2 can be attributed to the proton diffusion through NiOOH while D_1 and D_3 are associated with the diffusion through $Ni(OH)_2$ compounds, most likely $Ni(OH)_2$. The fact that proton transport through the Ni(II) phase is described by two different values of D can be attributed to the contribution of NiO in the Ni(II)

layer, therefore the latter can be treated as a mixture of $Ni(OH)_2$ and NiO. A good linearity of ln D vs. T^{-1} plots allows us to calculate the activation energy on the basis of Eq. 6.8. Such obtained E_a values are 25 ± 3, 26 ± 3 and 28 ± 2 kJ mol^{-1} for D_1, D_2 and D_3, respectively. The model presented in this section requires both phases, Ni(II) and Ni(III), to be in contact with the electrolyte solution. The Ni(II)–electrolyte and Ni(III)–electrolyte interfaces participate in proton exchange between the electrolyte and the electrode so further transport of H^+ takes place in the bulk of the Ni(II) and Ni(III) phases. Jain et al. determined the ratio between Ni(II) and Ni(III) phases for $Ni(OH)_2$ by the electrode potential [247]. The same method can be applied for the oxidation of the metallic Ni electrode ensuring coexistence of both phases in contact with the electrolyte.

When the crystallographic structure of the metal and the oxidation products (i.e. oxide/hydroxide) differs significantly, the oxidation mechanism must include phase transition or atom rearrangement processes in order to build the new lattice structure of the oxide/hydroxide. It is likely that this phase transition or rearrangement is the r.d.s. However, crystallographic structures of $Ni(OH)_2$ and NiOOH are similar; the main difference between these two structures is the number of H atoms (assuming undisturbed stoichiometry of compounds formed on Ni electrode) [9]. Therefore, one can assume that the kinetics of the $Ni(OH)_2 \leftrightarrow$ NiOOH redox couple does not require a significant atom rearrangement and its rate could be determined by the diffusion of protons in NiOOH and $Ni(OH)_2$ phases. Since we did not observe a significant difference between the results obtained in quiescent and N_2 stirred solutions, we can conclude that the rate determining

diffusion process takes place in the electrode material, i.e. the oxide/hydroxide layer and not in the solution.

6.7 Conclusions

Oxidation of the Ni(II) layer formed on metallic Ni electrodes is controlled by a diffusion process inside the oxidized layer. Analysis of the j_p vs. $v^{1/2}$ relations suggests the applicability of Randles–Sevcik model. A finite–length diffusion model explains the departure from linearity of these curves at low scan rate values. A non–zero intercept of the j_p vs. $v^{1/2}$ plots could be the result of multiple diffusion processes in two different phases. The effective diffusion coefficient obtained from the j_p vs. $v^{1/2}$ relations is ca. 10^{-12} cm^2 s^{-1} at room temperature and the activation energy values are in the range of 23 – 26 kJ mol^{-1}. The influence of hydrogen trapping phenomena and electro–migration on the overall H^+ transport is insignificant. Chronoamperometry profiles for the Ni(II) oxidation are best analyzed as a sum of three parallel diffusion processes, each one is described by exponential relations between the current density and the time. The diffusion processes are treated according to the model of finite–length diffusion which allows us to estimate D and E_a for the processes. The diffusion coefficient values of D_2 are comparable to those calculated from cyclic voltammetry experiments at various potential scan rates. The other D values (D_1 and D_3) are significantly smaller. The values of the activation energy of the three processes are comparable to the E_a values calculated from cyclic voltammetry experiments, which confirms the accuracy of the method applied.

Chapter 7 – Electro–reduction of pre–formed PtO at well–defined experimental conditions

The growth kinetic and mechanism of the surface oxides on Pt electrode is a widely studied system. This is due to the fact that Pt is extensively used as a catalyst in many chemical and electrochemical technologies and also serves as a model system for the oxide growth at non–noble metals. The electro–oxidation of Pt electrode and the subsequent electro–reduction of the oxides are important because they affect the kinetics of interfacial electron transfer. The initial stages of the oxide growth and the subsequent reduction can be studied in detail using different electrochemical and surface science techniques [49-64]. The electro–reduction of PtO oxides in acidic solution has never been a subject of systematic research, except in the presence of dissolved hydrogen, and the reduction mechanism is not understood at all. As the reduction mechanism is unknown and has never been a subject of research, it is difficult to determine the exact reduction kinetics. Thus, this study presents the first comprehensive set of data for the PtO oxide reduction that can bring about new understanding of the process and create favorable conditions for the eventual development of an oxide–reduction theory.

7.1 Electrochemical Procedures for the Electro–Reduction of PtO Oxide

The PtO electro–reduction was studied in detail by the application of cyclic voltammetry according to the following steps:

(i) Prior to the electro–reduction study, the PtO oxide was electrochemically formed by the application of well–controlled polarization conditions (E_p = 1.5 V and t_p = 10000 s), which lead to the formation of a thin oxide layer of well–known composition and thickness. The value of the reproducible charge density (q_{ox}) was 896 μC cm^{-2} and corresponded to ca. 2 ML of PtO. The same E_p and t_p values were employed to ensure the same oxide thickness, thus the same charge density for each set of experiments. This charge density serves as a reference value for the subsequent oxide reduction study.

(ii) Step one is repeated (to ensure that the value of q_{ox} is 896 μC cm^{-2}), followed by a subsequent reduction of the oxide by the application of a negative–going sweep that started at 1.5 V and held/stopped at various pre–selected reduction potential values, $0.66 \leq E_r \leq 0.94$ V (with an interval of 0.02 V).

(iii) For each reduction potential value, the negative potential scan was held for various reduction times, $1 \leq t_r \leq 10000$ s, then the negative–going sweep was continued to 0.05 V. Any remaining amount of PtO was reduced upon completion of the CV scan.

(iv) Repetition of steps i, ii and iii at different temperature values, $283 \leq T \leq 323$ K.

7.2 Determination of the Charge Density

The charge density of the unreduced or remaining PtO oxide that resides on the electrode surface was precisely determined from the subsequent CV profile after the

partial oxide reduction at E_r. The qualitative determination of the remaining (unreduced) charge density (q_{rm}) allows us to determine the amount of the reduced oxide (q_{red}) by subtracting q_{rm} from the total charge density ($q_{ox} = q_{rm} + q_{red}$). Figure 7.1 shows a CV oxide reduction profile (cathodic scan) for Pt electrode in 0.5 M aq. H_2SO_4 solution recorded at E_p = 1.5 V, T = 298 K, v = 50 mV s^{-1} and at t_p = 10000 s. The CV oxide reduction profile reveals one peak only (OC1 peak) which corresponds to the reduction of PtO and confirms that the pre–formed oxide film consists only of PtO. The CV profile shown in Fig. 7.1 was recorded several times to ensure the reproducibility of the result and was used to determine the total charge density prior to the electro–reduction experiments. It serves as a reference CV profile at each specific temperature for the electro–reduction experiments performed for different values of E_r and t_r.

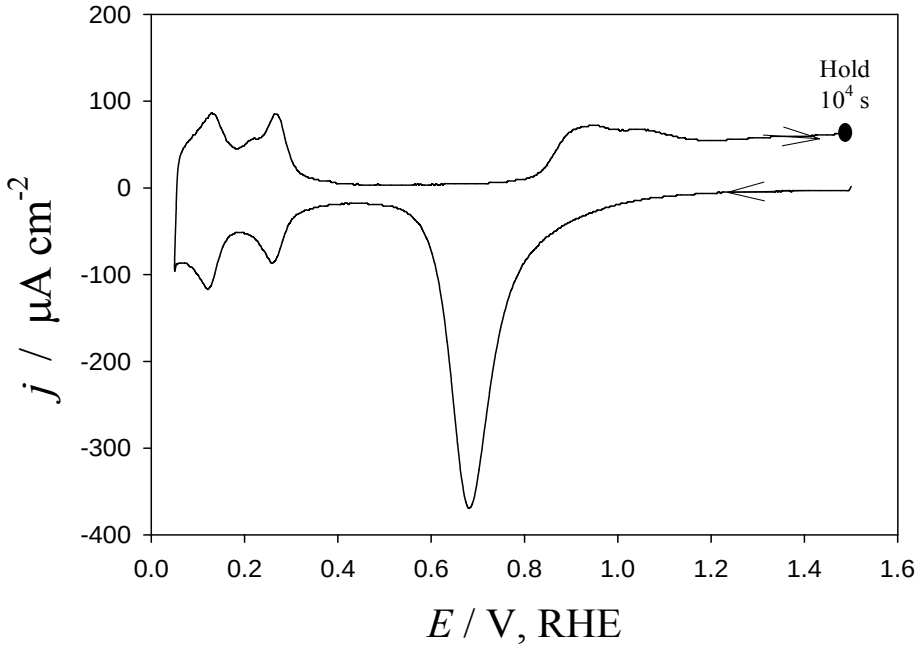

Figure 7.1. CV oxide formation and reduction profile for Pt electrode in 0.5 M aq. H_2SO_4 recorded at E_p = 1.5 V, v = 50 mV s^{-1}, T = 298 K and for t_p = 10000 s.

In Figure 7.2, we show a series of CV oxide–reduction profiles for Pt electrode in 0.5 M aq. H_2SO_4 solution recorded at E_r = 0.94 V, T = 298 K, v = 50 mV s^{-1} and for various reduction times, namely 1, 10, 10^2, 10^3 and 10^4 s. It should be emphasized that when the potential scan is held at a given E_r value, the current falls to a small but non–zero value, which indicates that the reduction of the oxide is still occurring. Comparing the charge density of the remaining oxide with the value for the pre–formed oxide, q_{ox} (Fig. 7.1) allows us to determine the amount of the oxide reduced at each set of E_r and t_r values. We observe that the charge density of the remaining PtO slightly decreases with the increase in the reduction time (see Fig. 7.3). In the case of E_r = 0.94 V and T = 298 K, an increase in the reduction time from 1 to 10^4 s reduces the remaining charge density from 889 to 802 μC cm^{-2}. Another important observation is that the half–width of the reduction peak becomes smaller upon the increase in the reduction time.

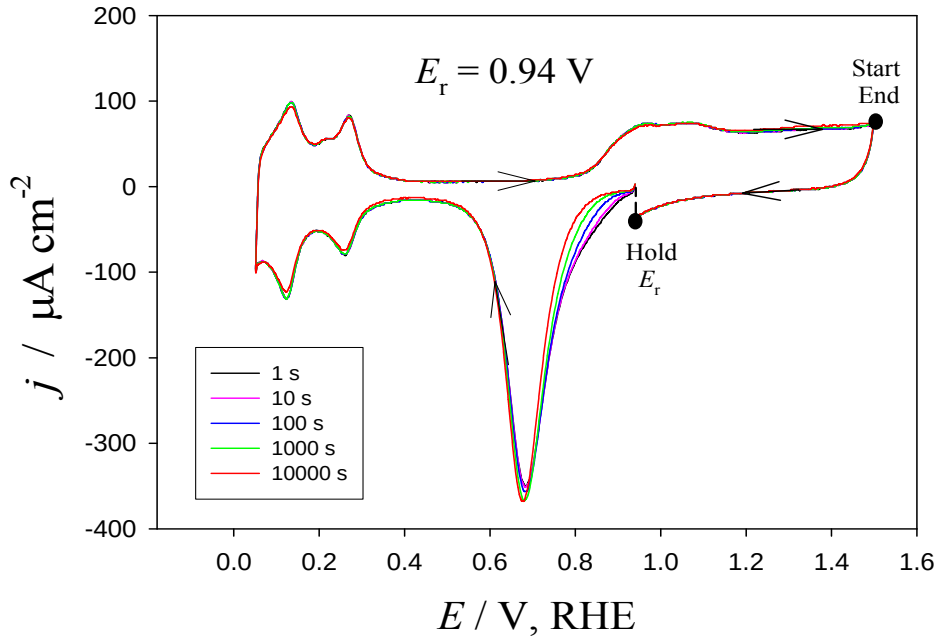

Figure 7.2. Series of CV oxide–reduction profiles for Pt electrode in 0.5 M aq. H_2SO_4 recorded at E_r = 0.94 V, v = 50 mV s^{-1}, T = 298 K, and at $1 \leq t_r \leq 10000$ s.

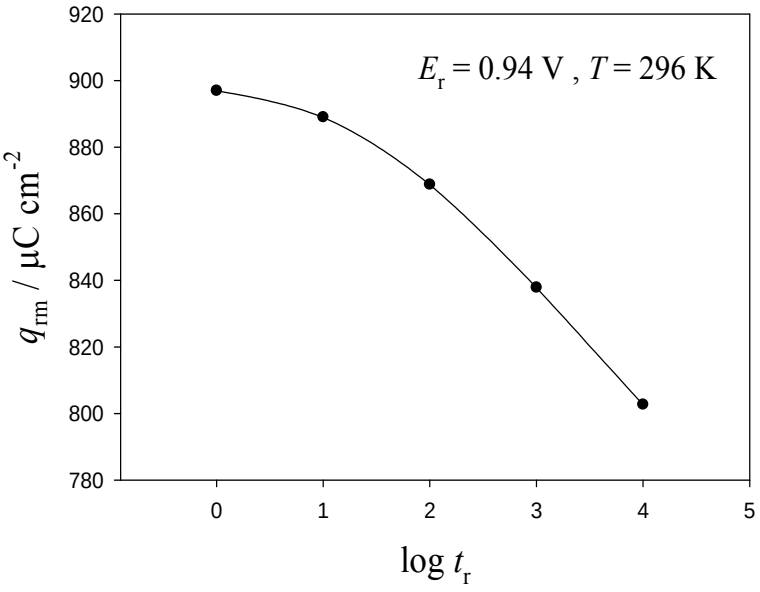

Figure 7.3. q_{rm} vs. log t_r relation for Pt electrode calculated on the basis of Fig. 2.

Figures 7.4a, b, c and d show four series of CV oxide–reduction profiles for Pt electrode in 0.5 M aq. H_2SO_4 solution recorded at E_r = (a) 0.90 V, (b) 0.86 V, (c) 0.82 V and (d) 0.78 V which are representative of the overall behavior. For a given t_r, we observe that the amount of the remaining oxide decreases as E_r becomes less–positive. Furthermore, for a given E_r, the amount of the remaining oxide decreases as t_r is extended. An extension of the reduction time from 1 to 10, 100, 1000 and 1000 s reduces the amount of q_{rm} as follows: (a) from 844 to 631 μC cm^{-2} for E_r = 0.90 V, (b) from 781 to 293 μC cm^{-2} for E_r = 0.86 V, (c) from 672 to 32.8 μC cm^{-2} for E_r = 0.82 V and (c) from 518 to 1.79 μC cm^{-2} for E_r = 0.78 V.

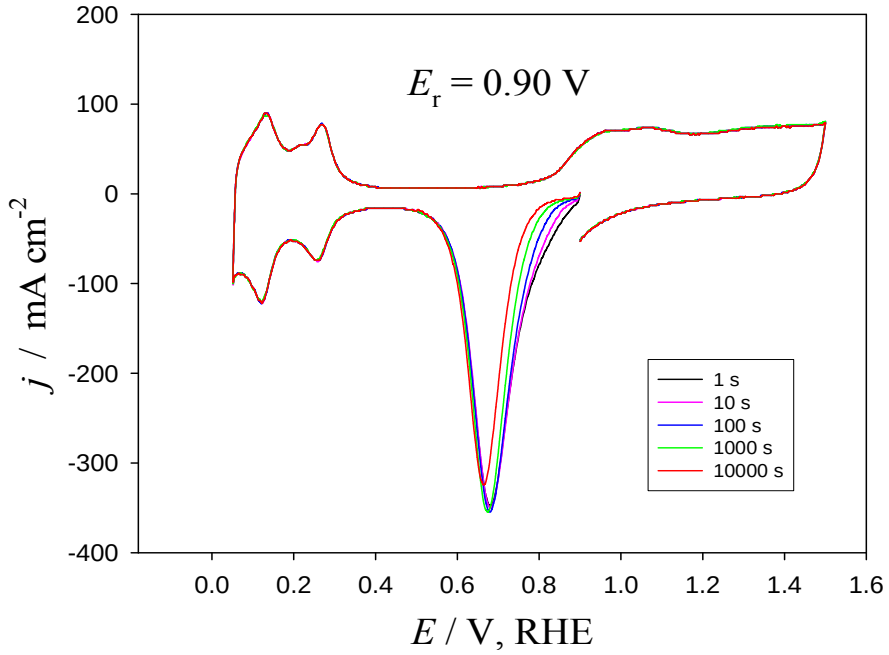

Figure 7.4a. Series of CV oxide–reduction profiles for Pt electrode in 0.5 M aq. H_2SO_4 recorded at E_r = 0.90 V, v = 50 mV s^{-1}, T = 298 K, and at $1 \leq t_r \leq 10000$ s.

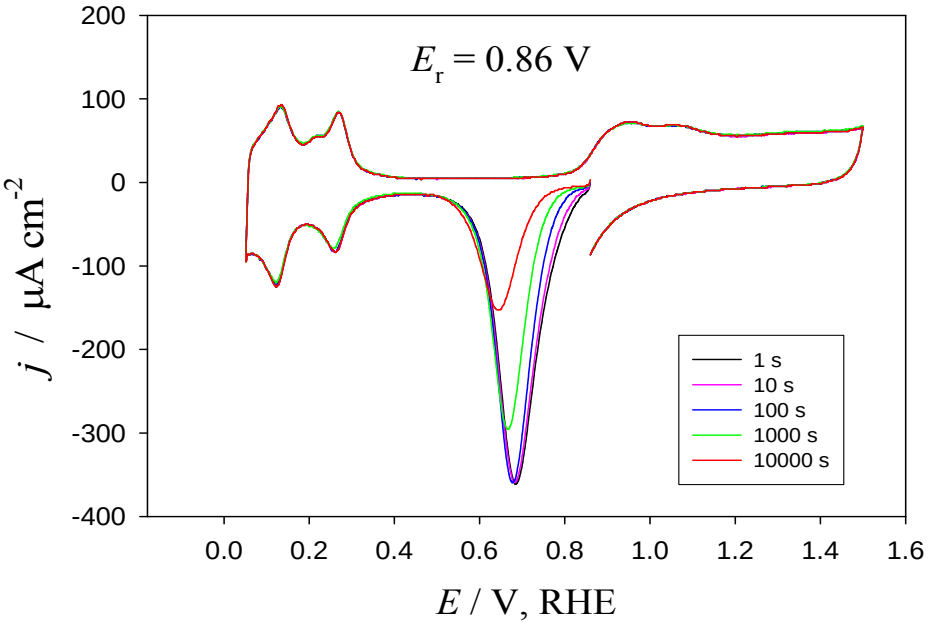

Figure 7.4b. Series of CV oxide–reduction profiles for Pt electrode in 0.5 M aq. H_2SO_4 recorded at E_r = 0.86 V, v = 50 mV s^{-1}, T = 298 K, and at $1 \leq t_r \leq 10000$ s.

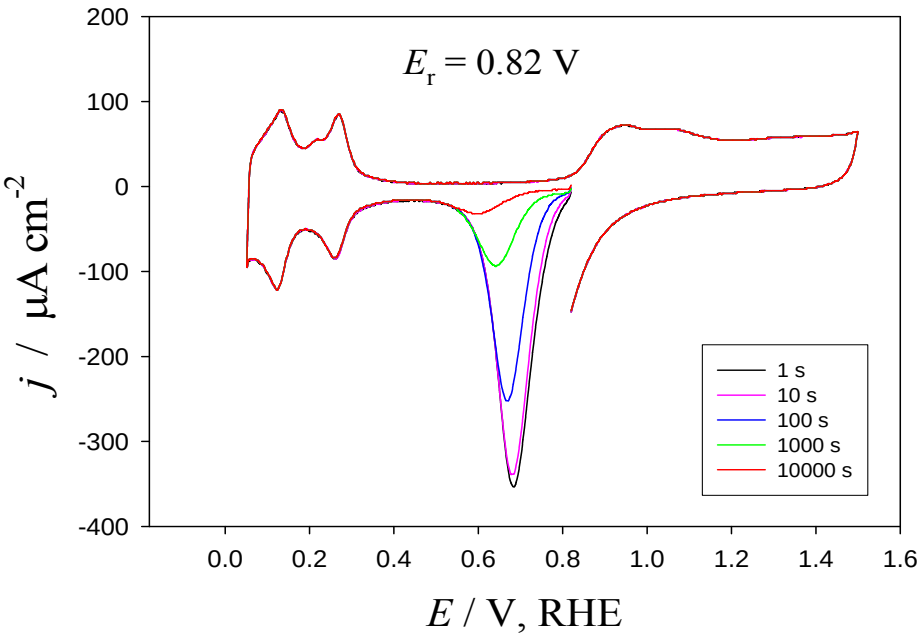

Figure 7.4c. Series of CV oxide–reduction profiles for Pt electrode in 0.5 M aq. H_2SO_4 recorded at $E_r = 0.82$ V, $v = 50$ mV s^{-1}, $T = 298$ K, and at $1 \leq t_r \leq 10000$ s.

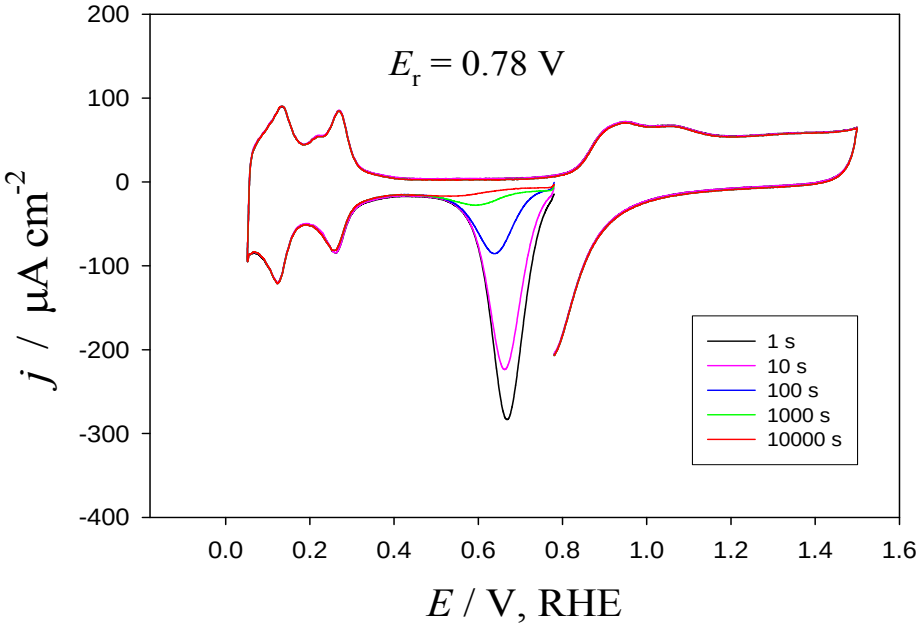

Figure 7.4d. Series of CV oxide–reduction profiles for Pt electrode in 0.5 M aq. H_2SO_4 recorded at $E_r = 0.78$ V, $v = 50$ mV s^{-1}, $T = 298$ K, and at $1 \leq t_r \leq 10000$ s.

Because the electrochemical growth of monolayer oxides on noble metals is logarithmic or inverse–logarithmic in time, it is logical to evaluate whether the electrochemical reduction of oxides is also logarithmic or inverse–logarithmic in time. The q_{rm} vs. log t_r relations, presented in Fig. 7.5, were determined on the basis of the CV oxide–reduction profiles for PtO at the E_r and t_r values reported above. From Fig. 7.5, it follows that the amount of q_{rm} decreases quickly with time at less positive E_r values. Furthermore, by comparing the results obtained at two different values of t_r (i.e. t_r = 10 and t_r = 100 s), it follows that the q_{rm} also decreases rapidly as a function of E_r for higher t_r values.

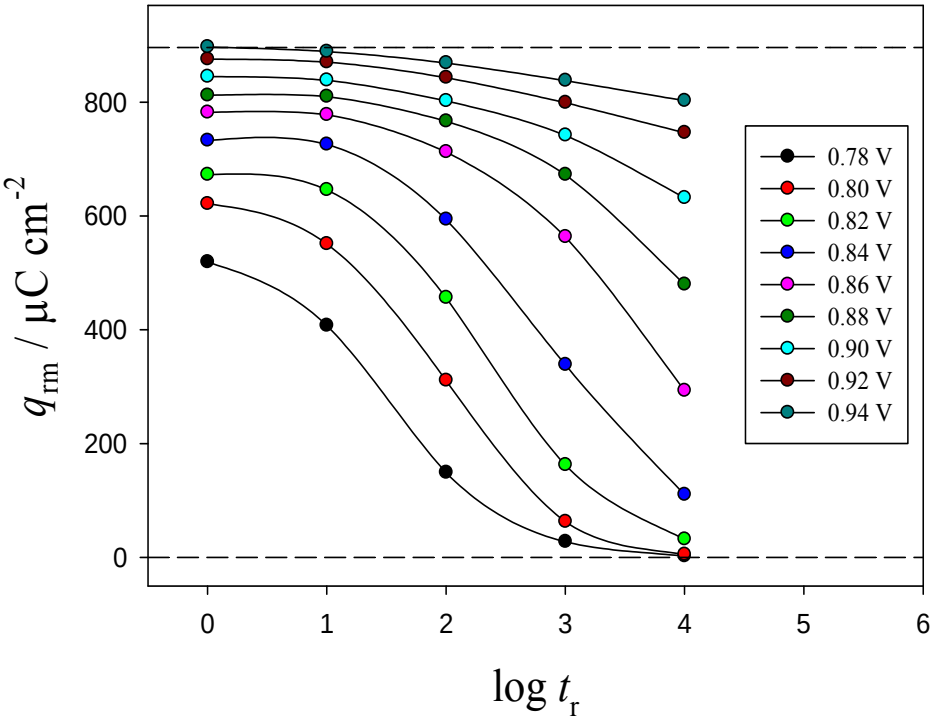

Figure 7.5. q_{rm} versus lot t_r relation for Pt electrode in 0.5 M aq. H_2SO_4 recorded at T = 298 K, 0.78 ≤ E_r ≤ 0.94 V and at 1 ≤ t_r ≤ 10000 s.

7.3 Electro–Reduction of the PtO at Different Temperatures

In a similar manner, the electro–reduction of the PtO oxides was studied at different temperatures in order to investigate the impact of T on the oxide reduction. The electro–reduction of a thin layer of PtO was studied at lower temperature value (283 K) and at higher T values, namely 308 and 323 K. For each set of electro–reduction experiment at constant T value, a reference CV profile was recorded prior to each experiment as described in section 7.1. Figures 7.6a and 7.6b show reference CV profiles for PtO pre–formed in 0.5 M aq. H_2SO_4 recorded at E_p = 1.5 V and $t_p = 10^4$ s for T = 283 K (a) and T = 323 K (b), respectively; the scan rate is 50 mV s^{-1} in both cases.

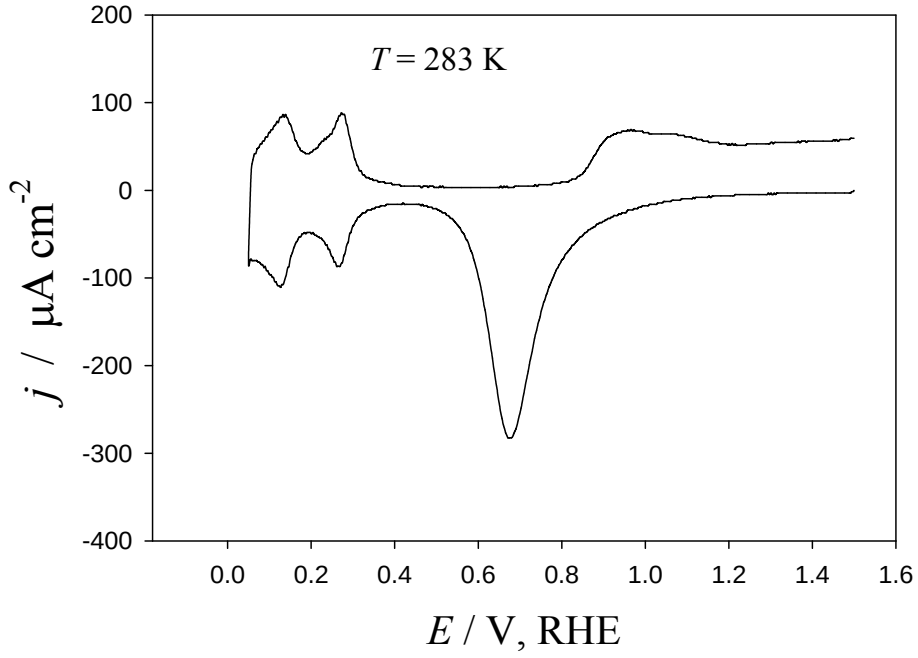

Figure 7.6a. CV oxide formation and reduction profile for Pt electrode in 0.5 M aq. H_2SO_4 recorded at E_p = 1.5 V, v = 50 mV s^{-1}, T = 283 K and for t_p = 10000 s.

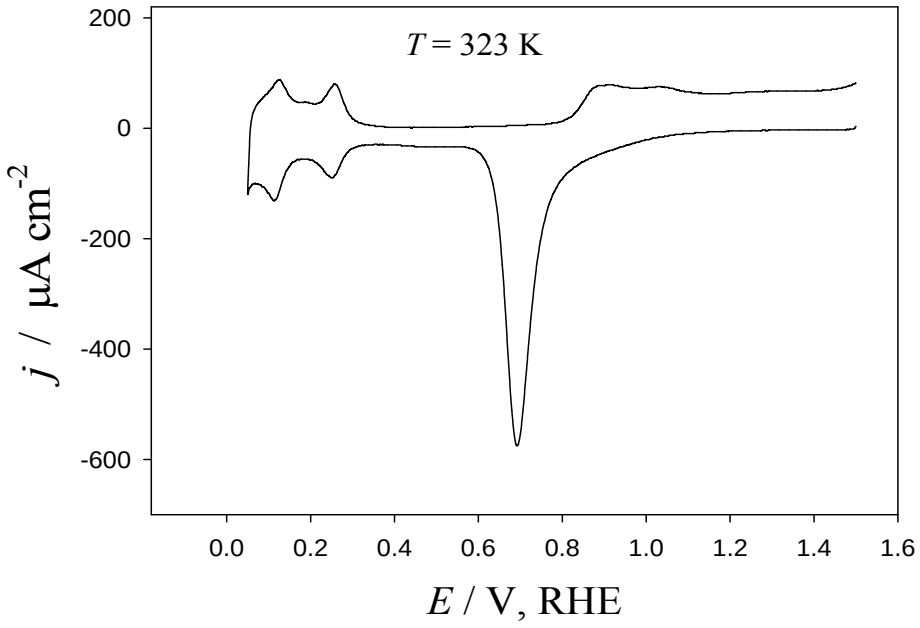

Figure 7.6b. CV oxide formation and reduction profile for Pt electrode in 0.5 M aq. H_2SO_4 recorded at E_p = 1.5 V, v = 50 mV s^{-1}, T = 323 K and for t_p = 10000 s.

Figures 7.7a, b and c show three series of CV profiles for T = 283, 308 and 323 K, respectively. In each case, E_r = 0.8 V and each serie of CV profiles corresponds to t_r = 1, 10, 100 and 1000 s. We observe that the reduction peak (i.e. the remaining charge density) decreases upon the extension of t_r and this decrease is more pronounced for higher T values. This indicates that a greater amount of the oxide is reduced at higher temperature value while other parameters (i.e. t_r and E_r) are constant. A small shift in the potential of the reduction peak is also observed for the entire range of E_r, t_r and T values.

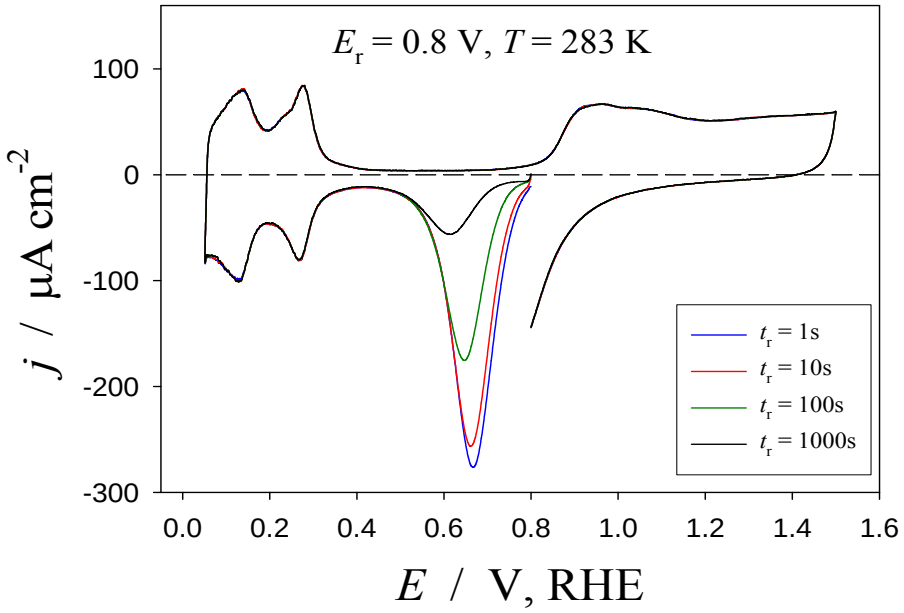

Figure 7.7a. Series of CV oxide–reduction profiles for Pt electrode in 0.5 M aq. H_2SO_4 recorded at $E_r = 0.80$ V, $v = 50$ mV s^{-1}, $T = 283$ K, and at $1 \leq t_r \leq 1000$ s.

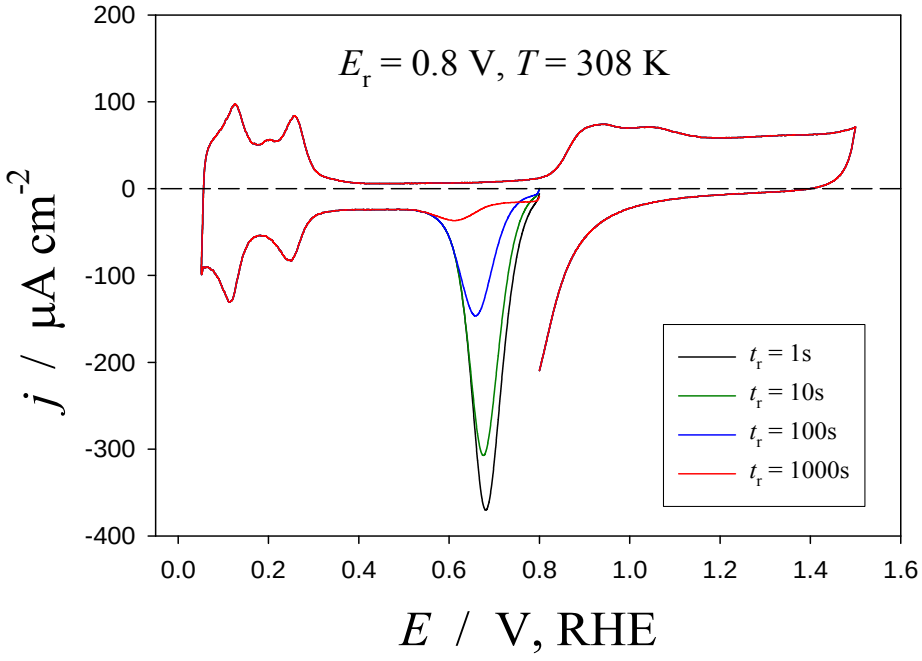

Figure 7.7b. Series of CV oxide–reduction profiles for Pt electrode in 0.5 M aq. H_2SO_4 recorded at $E_r = 0.80$ V, $v = 50$ mV s^{-1}, $T = 308$ K, and at $1 \leq t_r \leq 1000$ s.

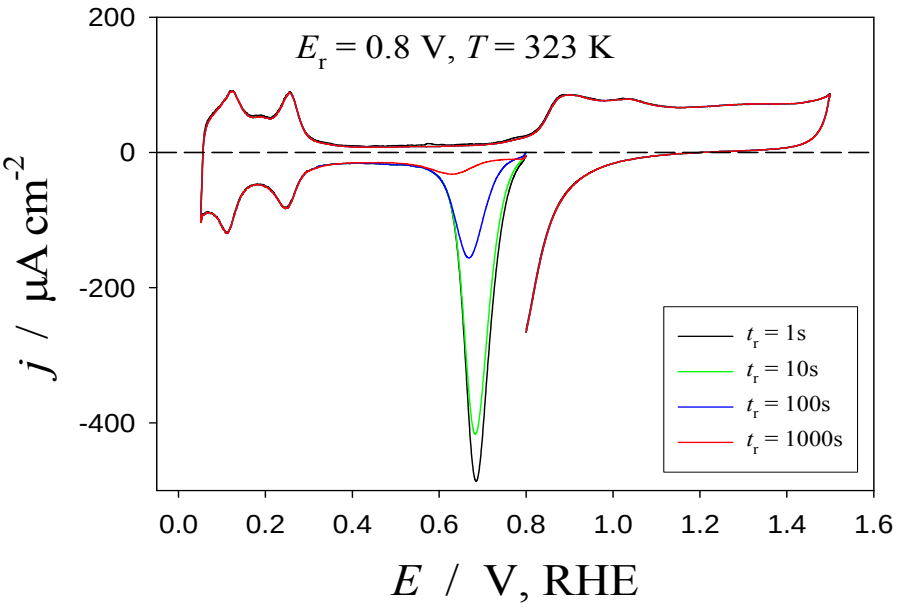

Figure 7.7c. Series of CV oxide–reduction profiles for Pt electrode in 0.5 M aq. H_2SO_4 recorded at $E_r = 0.80$ V, $v = 50$ mV s^{-1}, $T = 323$ K, and at $1 \leq t_r \leq 1000$ s.

Shibata et al. [40] reported that the rate of the PtO reduction, in the presence of dissolved hydrogen, is rapidly increased when the surface coverage of the oxide is 0.6 and proposed that the oxide reduction proceeds according to the following steps:

$$H_2 \longrightarrow 2H^+ + 2e^- \qquad (7.1)$$

$$Pt\text{–}O + 2H^+ + 2e^- \longrightarrow Pt + H_2O \qquad (7.2).$$

Conway et al. [55] proposed a two–step mechanism for the reduction of PtO in aq. H_2SO_4 solution that involves the formation of PtOH according to the following equations:

$$PtO + H^+ + e^- \longrightarrow PtOH \quad (7.3)$$

$$PtOH + H^+ + e^- \longrightarrow Pt + H_2O \quad (7.4).$$

Arvia et al. [41] also proposed a two–step mechanism for the PtO reduction in molten alkaline solution ($NaHSO_4$-$KHSO_4$ and $KHSO_4$ melts) and supports the proposal of PtOH formation. The first step of Arvia's et al. reduction mechanism is the same as in Conway's mechanism (Eq. 7.3), while the second step is as follow:

$$PtOH + PtOH \longrightarrow Pt + PtO + H_2O \quad (7.5).$$

As mentioned earlier, there is no theory in the literature that explains the oxide reduction of noble metals, thus we present a qualitative discussion of the result without the application of any theoretical method. The charge density is a main parameter in the discussion and the analysis of any oxide growth kinetics [37]. Therefore, we analyzed the relation between the charge density of the remaining and the reduced oxide as a function of E_r and t_r for various temperature values. The data presented in Fig. 7.8a and b illustrate the relation between the reduced amount of PtO (after subtracting the remaining charge density from the total q_{ox}) and E_r for two different t_r values, namely (a) 10 s and (b) 1000 s. These results are representative of the overall trend.

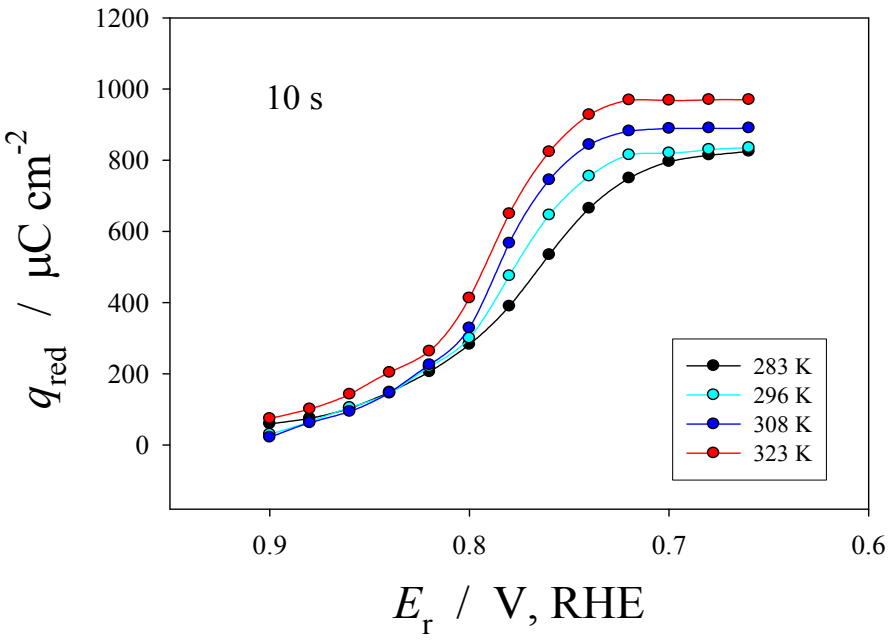

Figure 7.8a. q_{red} versus E_r relation for Pt electrode in 0.5 M aq. H_2SO_4 recorded at t_r = 10 s, 283 ≤ T ≤ 323 K and at 0.76 ≤ E_r ≤ 0.90 V.

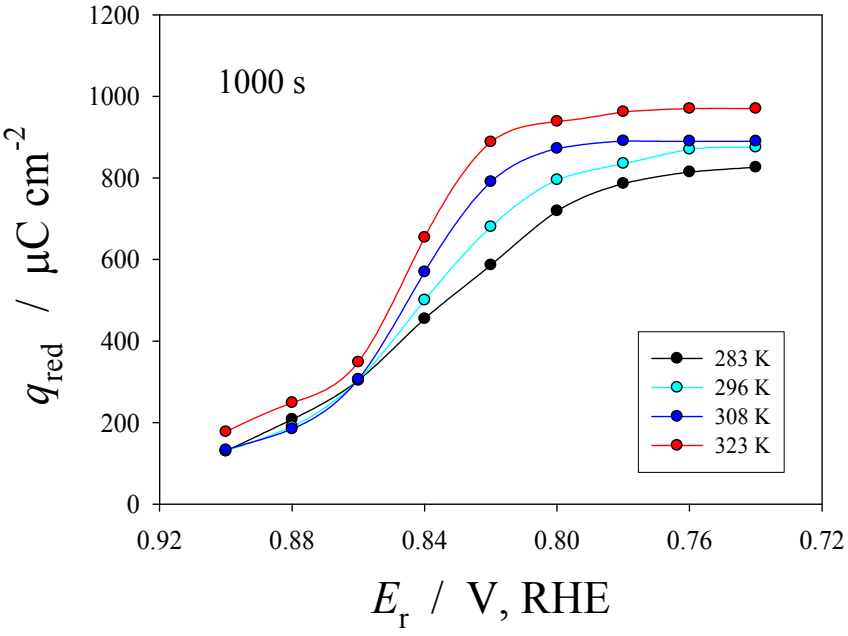

Figure 7.8b. q_{red} versus E_r relation for Pt electrode in 0.5 M aq. H_2SO_4 recorded at t_r = 1000 s, 283 ≤ T ≤ 323 K and at 0.76 ≤ E_r ≤ 0.90 V.

The E_r scale (the x–axis) in Fig. 7.8 is reversed in order to depict the changes in the amount of q_{red} as a function of E_r during the negative–going scan. The amount of the reduced oxide is greater when E_r has less positive values. Moreover, at constant E_r value, the PtO oxide is reduced more at higher temperature values. From the comparison of Fig. 7.8a and 7.8b, it follows that the amount of PtO reduced increases with the extension of t_r. The ratio between the charge density of the reduced PtO amount and the total charge density of the pre–formed oxide, q_{red}/q_{tot} is presented in Figure 7.9a as a function of E_r. In a similar manner, the ratio between the charge density of the remaining PtO (q_{rm}) on the electrode surface and q_{tot} is illustrated in Fig. 7.9b as a function of E_r.

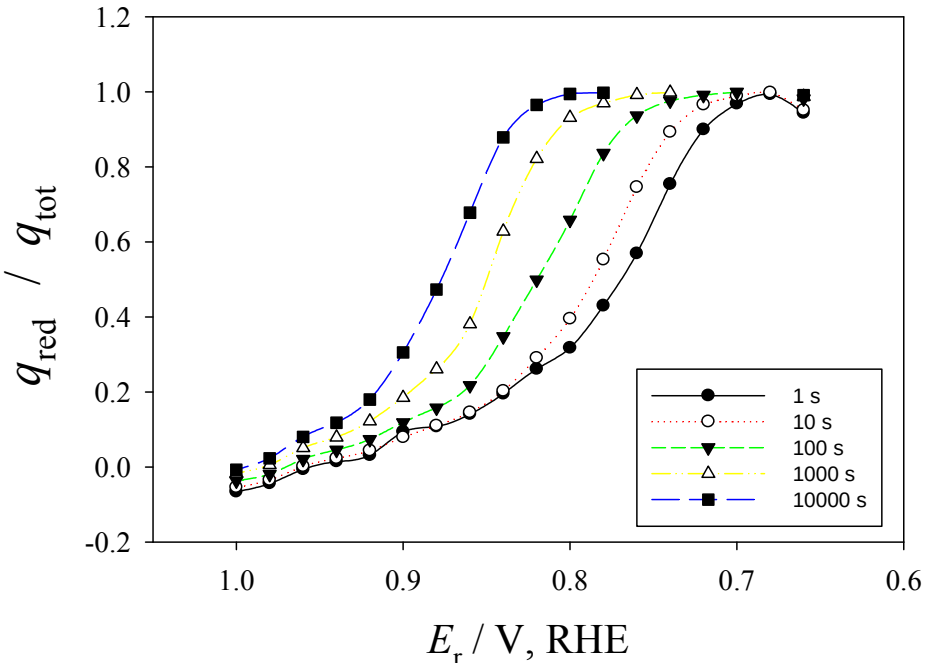

Figure 7.9a. q_{red}/q_{tot} vs. E_r relation for Pt electrode in 0.5 M aq. H_2SO_4 recorded at T = 298 K, $1 \leq t_r \leq 10000$ s and at $0.66 \leq E_r \leq 1.0$ V.

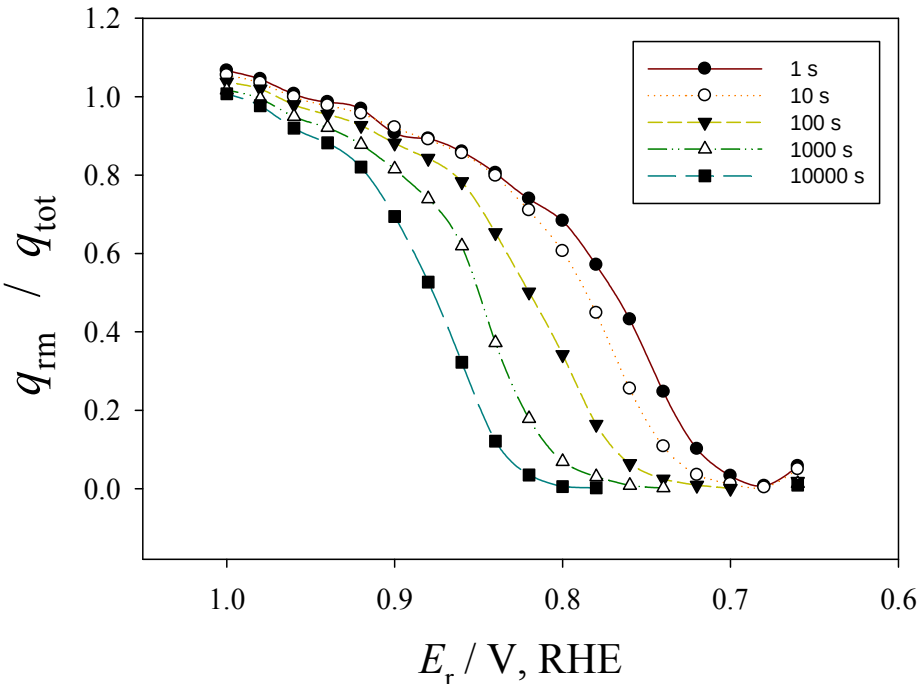

Figure 7.9a. q_{rm}/q_{tot} vs. E_r relation for Pt electrode in 0.5 M aq. H_2SO_4 recorded at T = 298 K, $1 \leq t_r \leq 10000$ s and at $0.66 \leq E_r \leq 1.0$ V.

The formation of PtO is slow and long t_p is required to form 2 MLs of PtO; each monolayer follows a different growth mechanism. The first ML follows a logarithmic growth kinetic, while the second ML follows inverse–logarithmic growth kinetics [37]. In the case of logarithmic growth mechanism, the rate determining step is the interfacial place exchange between the O_{chem} and the top–most Pt atoms, whereas in the case of inverse–logarithmic growth law the r.d.s. is the escape of the Pt cation (Pt^{2+}) from the metal into the oxide at the inner metal/oxide interface. The 2 MLs of PtO can be reduced within several seconds in a single negative–going potential scan; the PtO electro–reduction resembles a desorption isotherm, but the process is not a simple electro–desorption. The result shown in Figs. 7.10a and b are 3–D presentation for the charge

density of the remaining PtO as a function of E_r and log t_r recorded in 0.5 M aq. H_2SO_4 solution at (a) 298 K and (b) 323 K.

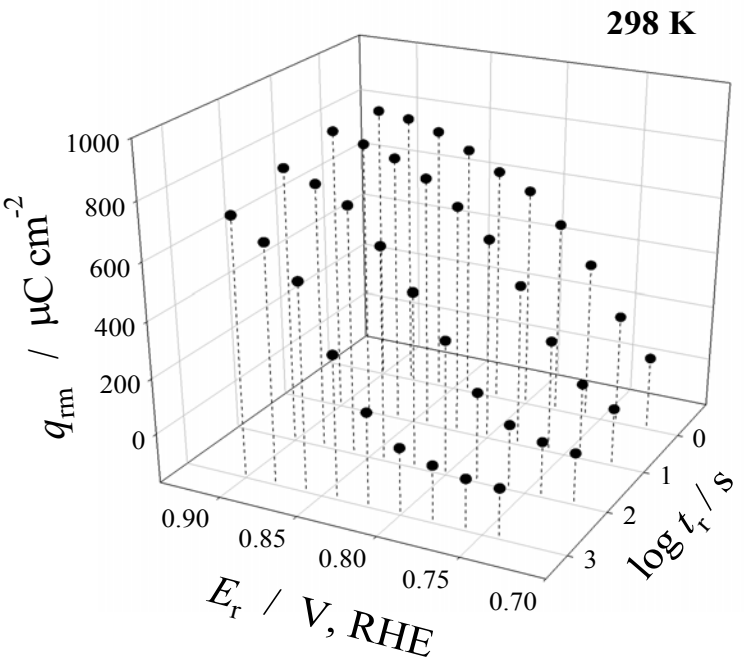

Figure 7.10a. 3–D plot for q_{red} versus E_r and log t_r for Pt electrode in 0.5 M aq. H_2SO_4 solution recorded at $0.76 \leq E_p \leq 0.9$ V, $1 \leq t_p \leq 1000$ s and at $T = 298$ K.

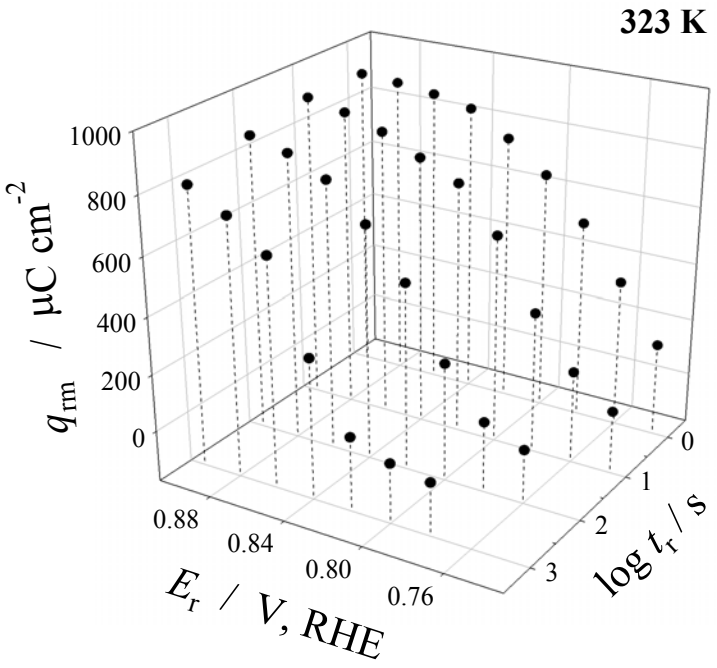

Figure 7.10b. 3–D plot for q_{red} versus E_r and log t_r for Pt electrode in 0.5 M aq. H_2SO_4 solution recorded at $0.76 \leq E_p \leq 0.9$ V, $1 \leq t_p \leq 1000$ s and at $T = 323$ K.

7.4 Conclusion

The well–controlled polarization conditions of E_p and t_p lead to the formation of a thin PtO oxide; the CV profile reveals one reduction peak that corresponds to the formation of PtO. The growth mechanism and kinetics are well known for Pt electrode but there is no theory for the electro–reduction of PtO or any other oxide. We observe that the case of PtO layers comprising ca. 2 ML of PtO, the reduction of the oxide requires much less time once ca. 1 ML of the PtO has been reduced (ca. 1 ML of PtO remains). We do not want to refer to it as a reduction rate because at the present time there are no theories that treat electrochemical reduction of metal oxide. The amount of

the reduced PtO increases upon the extension of t_r. In general, for higher values of t_r and/or lower E_r values, the amount of the reduced oxide is greater and consequently smaller amount of the remaining PtO oxide.

Chapter 8 – Conclusions

Anodic polarization of Ni electrode in an alkaline solution to Ni(II) and subsequently to Ni(III) was studied in detail by means CV, CA and XPS depth–profiling techniques. For the oxidation of Ni to β-$Ni(OH)_2$, a linear relation between the reciprocal of the hydroxide thickness and the logarithm of the polarization time is observed. This linear relation suggests that the growth of β-$Ni(OH)_2$ follows the inverse–logarithmic growth kinetics of Mott–Cabrera. In addition, the thickness of the β-$Ni(OH)_2$ hydroxide layer is smaller than the value of X_o and X_1 parameters. This also suggest that the β-$Ni(OH)_2$ growth might follow inverse–logarithmic growth. The value of the electric field across the oxide film increases at higher polarization potential values. The β-$Ni(OH)_2$ film thickness increases with the increase in the polarization potential and/or polarization time and/or temperature values.

On the other hand, the electrochemical oxidation of Ni(II) to NiOOH proceeds according a diffusion–controlled mechanism. As expected for the diffusion process a linear relation between the peak current (j_p) and the square root of the scan rate ($v^{1/2}$) is observed. According to the semi–finite diffusion model, the relation between j_p and $v^{1/2}$ should be linear in the entire range of scan rate and should pass through the zero point. The j_p vs. $v^{1/2}$ relation obtained in this study was observed to depart from linearity for low scan rates and this behavior was explained on the basis of the finite–length diffusion model. Our results show that the non–zero intercept of the j_p vs. $v^{1/2}$ plots is a result of different diffusion processes occurring in two different phases. The effective diffusion coefficient for the anodic and cathodic processes at T = 298 K are of $8.1 \pm 0.2 \times 10^{-12}$

and $4.3 \pm 0.2 \times 10^{-12}$ cm^2 s^{-1}, respectively. Such determined values of the activation energy for the anodic and cathodic diffusion processes are 23 ± 2 and 26 ± 2 kJ mol^{-1}, respectively. Our results show that the effect of the hydrogen trapping and the electro–migration on the overall H^+ transport is insignificant. The chronoamperometry profiles are best fitted for three parallel diffusion processes; each one is described by an exponential relation between the current density and the time. The diffusion coefficient values obtained from the CA experiments are comparable to those calculated from the CV experiments at various potential scan rates. The value of the activation energy obtained from the CA measurements are comparable to the E_a values calculated from cyclic voltammetry experiments, which confirms the applicability the accuracy of the two methods applied.

The kinetics and the mechanism of the PtO electro–reduction are unknown and there is no theory that explains the process. This study presents qualitative data for the PtO oxide reduction in 0.5 M aq. H_2SO_4 electrolyte solution that can be used in a qualitative analysis of the reduction process and shed light on any applicable kinetic laws. In a similar manner to the oxide growth study, we analyzed the charge density of the oxide reduction as a function of the well–controlled experimental conditions. The charge density of the reduced PtO oxide increases as the reduction potential value becomes less positive. Furthermore, it also increases with the increase in the reduction time and/or the temperature. A rapid increase in quantity of the reduced oxide's charge density is observed after the removal of ca. one monolayer of PtO. The relation between the charge density of the remaining oxide and the reduction time is non–linear for the entire experimental potential, time and temperature range.

References

1. Aubrey Stimola, Nickel, Rosen publishing group Inc., New York, 2007.
2. Joseph R. Davis, Nickel, cobalt and their alloys, AMS Inernational USA, 2000.
3. S. Maximovitch and R. Durand, *J. Electroanal. Chem.*, 149 (1983) 273.
4. P. W. T. Lu and S. Srinivasan, *J. Electrochem. Soc.* 125 (1978) 1416.
5. P. C. Yu and C. M. Lampert, *Solar Energy Mater.* 19 (1989) 1.
6. M. Fleischmann. K. Korinek and D. Pletcher, *J. Chem. Soc. Perkin II*, (1972) 1396.
7. R.G. Gunther and S. Gross, Eds., Proc. Symp. on the Nickel Electrode (Electrochemical Society, Princeton, NJ. 1982).
8. R.G. Gunther, S. Gross, Eds., in: Proc. Symp. on Nickel Electrodes, Electrochem. Soc. Vols. 82–84 (Electrochemical Society, Princeton, NJ, 1988)
9. P. Oliva, J. Leonardi, J.F. Laurent, C. Delmas, J.J. Braconnier, M. Figlarz and F. Fievet, *J. Power Sources* 8 (1982) 229
10. S.L Yau, F.R.F. Fan, T.P. Moffat, A.J. Bard, *J. Phys. Chem.*, 98 (1994) 5493
11. F. Hahn, D. Floner, B. Beden, C. Lamy, *Electrochimica Acta*, 32 (1987) 1631
12. R.J. Smith, R.E. Hummel, J.R. Ambrose, *Corros. Sci.*, 27 (1987) 815
13. L.M.M. de Souza, F.P. Kong, F.R. McLarmont, R.H. Muller, *Electrochimica Acta*, 42 (1997) 1253
14. R. Sandoval, R. Schrebler, H. Gómez, *J. Electroanal. Chem.*, 210 (1986) 287
15. C.A. Melendres, M. Pankuch, *J. Electroanal. Chem.*, 333 (1992) 103
16. H.W. Hoppe, H.H. Strehblow, *Surf. Interf. Anal*., 14 (1989) 121
17. A. Seyeux, V. Maurice, L. H. Klein, P. Marcus, *J. Solid State Electrochem.*, 9 (2005) 337
18. W. Paik, Z. Szklarska–Smialowska, *Surf. Sci.*, 96 (1980) 401
19. A.A. Wronkowska, *Surf. Sci.*, 214 (1989) 507
20. G. Larramona, C. Gutiérrez, *J. Electrochem. Soc.*, 137 (1990) 428
21. M. Grdeń, K. Klimek, *J. Electroanal. Chem.*, 581 (2005) 122

22. J.J. Braconnier, C. Delmas, C. Fouassier, M. Figlarz, B. Beaudouin and P. Hagenmuller, *Rev. Chim. Min*. 21 (1984) 496

23. C. Faure, C. Delmas and P. Willmann, *J. Power Sources* 36 (1991) 497

24. P.V. Kamath, M. Dixit, L. Indira, A.K. Shukla, V.G. Kumar and N. Munichandraiah, *J. Electrochem. Soc*. 141 (1994) 2956

25. Michel Broussely, Industrial applications of batteries: from cars to aerospace and energy storage, Elsevier, Oxford, 2007

26. David Linden, Handbook of batteries and fuel cells, McGraw–Hill, 1984

27. K.J. Vetter, J.W. Schultze, *J. Electroanal. Chem.* 34 (1972) 131.

28. K.J. Vetter, J.W. Schultze, *J. Electroanal. Chem.* 34 (1972) 141.

29. B.E. Conway, *Prog. Surf. Sci.* 49 (1995) 331.

30. A. Damjanovic, A. Dey, J.O'M. Bockris, *J. Electrochem. Soc.* 113 (1966) 739.

31. A. Damjanovic, V.I. Birss, *J. Electrochem. Soc.* 130 (1983) 1688.

32. A. Damjanovic, V.I. Birss, *J. Electrochem. Soc.* 133 (1986) 1621.

33. A. Damjanovic, V.I. Birss, *J. Electrochem. Soc.* 134 (1987) 113.

34. G. Tremiliosi-Filho, G. Jerkiewicz, B.E. Conway, *Langmuir* 8 (1992) 658.

35. G. Jerkiewicz, J.J. Borodzinski, *Langmuir* 9 (1993) 2202.

36. G. Jerkiewicz, J.J. Borodzinski, *J. Chem. Soc., Faraday Trans.* 90 (1994) 3669.

37. Alsabet M, Grden M, Jerkiewicz G, *J. Electroanal. Chem.*, 589 (2006) 120

38. F. Barz, M. Lungu, *J. Electroanal. Chem.*, 133 (1982) 101.

39. K. J. Vetter, J. W. Schultze, *J. Electroanal. Chem.*, 34 (1972) 131.

40. S. Shibata, M. P. Sumino, *Electrochim Acta*, 20 (1975) 739.

41. N. R. De Tacconi, A. J. Calandra, A. J. Arvia, *J. Electroanal. Chem.*, 57 (1974) 325.

42. L. D. Burke, A. Moynihan, *Electrochim Acta*, 15 (1970) 1437.

43. S. Shibata, *Electrochim. Acta*, 29 (1984) 453.

44. Yu. B. Vassiliev, V. S. Bagotzky, V. A. Gromyko, *J. Electroanal. Chem.*, 178 (1984) 247.

45. Yu. B. Vassiliev, V. S. Bagotzky, O. A. Khazova, *J. Electroanal. Chem.*, 181 (1984) 219.

46. N. R. De Tacconi, A. J. Calandra, A. J. Arvia, *J. Electroanal. Chem.*, 51 (1974) 25.

47. Jaspal S. Mayell, *J. Electrochem. Soc.*, 113 (1966) 385

48. A. J. Rudge, L.M. Peter, G. A. Hards, R. J. Potter, *J. Electroanal. Chem.*, 366 (1994) 253

49. B.E. Conway, T.C. Liu, *Proc. R. Soc. Lond.*, A429 (1990) 375.

50. B.E. Conway, G. Tremiliosi-Filho, G. Jerkiewicz, *J. Electroanal. Chem.* 297 (1991) 435.

51. G. Jerkiewicz, G. Tremiliosi-Filho, B.E. Conway, *J. Electroanal. Chem.* 334 (1992) 359.

52. B.E. Conway, G. Jerkiewicz, *J. Electroanal. Chem.* 339 (1992) 123.

53. G. Tremiliosi-Filho, L.H. Dall'Antonia, G. Jerkiewicz, *J. Electroanal. Chem.* 422 (1997) 149.

54. F. Villiard, G. Jerkiewicz, *Can. J. Chem.* 75 (1997) 1656.

55. H. Angerstein-Kozlowska, B.E. Conway, W.B.A. Sharp, *J. Electroanal. Chem*. 43 (1973) 9.

56. B.E. Conway, B. Barnett, H. Angerstein-Kozlowska, V.B. Tilak, *J. Chem. Phys.* 93 (1990) 8361.

57. H. You, D.J. Zurawski, Z. Nagy, R.M. Yonco, *J. Chem. Phys.* 100 (1994) 4699.

58. G. Jerkiewicz, G. Vatankhah, A. Zolfaghari, J. Lessard, *Electrochem. Comm.* 1 (1999) 419.

59. S. Gottesfeld, *J. Electrochem. Soc.* 127 (1980) 272.

60. S. Gottesfeld, G. Maia, J.B. Floriano, G. Tremiliosi-Filho, E.A. Ticianelli, E.R. Gonzalez, *J. Electrochem. Soc.* 138 (1991) 3219.

61. M. Peuckert, *Surf. Sci.* 141 (1984) 500.

62. K.S. Kim, N. Winograd, R.E. Davis, *J. Am. Chem. Soc.* 93 (1971) 6296.

63. G.C. Allen, P.M. Tacker, A. Capon, R. Parsons, *J. Electroanal. Chem.* 50 (1974) 335.

64. J.S. Hammond, N. Winograd, *J. Electroanal. Chem.* 78 (1977) 55.

65. G. Sparrow, Nickel, Marshall Cavendish Corporation, New York, 2005

66. Nickel Institute©, www.nickelinstitute.org

67. European Nickel PLC©, www.enickel.co.uk

68. R. M. Dell, D. A. J. Rand, Understanding batteries, Royal Society of Chemistry, Cambridge, UK, 2001.

69. Gates Energy Products, Rechargeable Batteries Applications Handbook, Butterworth-Heinemann, Washington, 1998.

70. Dkimages©, www.dkimages.com

71. Johnson Matthey©, www.matthey.com

72. A. G. Pinkus, Chemistry: Foundations and Applications, Macmillan Reference, USA, 2004

73. M. G. Fontana and N. D. Greene, Corrosion Engineering, 3rd ed., McGraw Hill, New York, 1986.

74. D.A. Jones, *Principles and Prevention of Corrosion*, Macmillan Pub. Co., New York, 1992.

75. Pierre R. Roberge, Handbook of Corrosion Engineering, McGraw-Hill, Washington, 2000.

76. H. L. F. Helmholtz, *Ann. Physik*, 89 (1853) 211.

77. Prof. T. Wandlowski©, http://www.dcbserver.unibe.ch/groups/wandlowski/research/edl.html

78. Peter Atkins, Julio de Paula, PHYSICAL CHEMISTRY, 8th Ed., W H Freeman & Co, 2006.

79. John O'M. Bockris, Amulya K. N. Reddy, Modern electrochemistry: an introduction to an interdisciplinary area, Vol. 2, Plenum Publishing Corporation, New York, 1970.

80. R. G. Compton, Giles H. W. Sanders, Electrode potential, Oxford University press, Oxford, UK, 1996.

81. S. Srinivasan, E. Gileadi, *Electrochimica Acta*, 11 (1966) 321

82. Southampton Electrochemistry Group, "*Instrumental Methods in Electrochemistry*", Ellis Horwood, New York, 1985

83. John O'M. Bockris, Amulya K. N. Reddy, Modern electrochemistry: an introduction to an interdisciplinary area, vol. 2, Plenum Publication Corporation, New York, 1973.

84. S. Trasatti, *Electrodes of Conductive Metallic Oxides* Part A, Elsevier, New York, 1980, Chapter 2

85. S. Trasatti, in: A. Wieckowski (Ed.), Interfacial Electrochemistry, Marcel Dekker, New York, 1999, Chapter 43

86. Budinski, Kenneth G., Surface engineering for wear resistance, Englewood Cliffs, New Jersey, 1988.

87. Marjorie A. Brimi, James R. Luck, Electrofinishing, American Elsevier Pub. Co., 1965.

88. Linda Garverick, Corrosion in the petrochemical industry, ASM International, Ohio, USA, 1994.

89. Joseph Wang , Analytical Electrochemistry, 3rd edition, John Wiley and Sons Inc., New J ersey, 2006.

90. Howard Fairbrother, Department of Chemistry, Johns Hopkins University, JHU Surface Analysis Laboratory.

91. R. Woods, Chemisorption at Electrodes in Electroanalytical Chemistry, vol. 9, Ed. A.J. Bard, Marcel Dekker Inc., New York, 1976.

92. B.E. Conway, W.B.A. Sharp, H. Angerstein-Kozlowska, E.E. Criddle, *Anal. Chem.* 45 (1973) 1321.

93. R. Simpraga and B.E. Conway, *J. Electroanal. Chem.*, 280 (1990) 341.

94. M.N. Hull, H.I. James, *J. Electroanal. Chem.*, 45 (1973) 281.

95. S.A.S. Machado, L.A. Avaca, *Electrochimica Acta*, 39 (1994) 1385.

96. Conway, B.E., Bai, L., *J. Chem. Soc., Faraday Trans. I.,* 81 (1985) 1841.

97. Lasia, A., Rami, A., *J. Electroanal. Chem.,* 294 (1990) 123.

98. B.A. Boukamp, *Solid State lonics*, 1986, 20, 31-44.

99. R.D. Armstrong, and M. Henderson, *J. Electroanal. Chem.*, 1972, 39, 81-90.

100. D.A. Harrington, and B.E. Conway, *Electrochim. Acta*, 32 (1987) 1703.

101. G.J. Brug, A.L.G. Van Den Eeden, M. Sluyters-Rehbach, and J.H. Sluyters, *J. Electroanal. Chem.*, 176 (1984) 275.

102. E. Navarro-Flores, and S. Omanovic, *J. Mol. Catal. A: Chemical*, 242 (2005) 182.

103. P. Zoltowski, *Electrochim. Acta*, 38 (1993) 2129.

104. S. Trasatti, and O.A. Petrii, *Pure Appl. Chem.*, 63 (1991) 711.

105. Y. Sasaki, T. Yamashita, *Thin Solid Films*, 334 (1998) 117.

106. M. Grdeń, K. Klimek, A. Czerwiński, *J. Solid State Electrochem.*, 8 (2004) 390.

107. C. Zhang, S.M. Park, *J. Electrochem. Soc.*, 134 (1987) 2966.

108. H. Bode, K. Dehmelt, J. Witte, *Electrochimica Acta*, 11 (1966) 1079.

109. S. Passerini, B. Scrosati, *J. Electrochem. Soc.*, 141 (1994) 889.

110. A. Gorenstein, F. Decker, W. Estrada, C. Esteves, A. Andersson, S. Passerini, S. Pantaloni, B. Scrosati, *J. Electroanal. Chem.*, 277 (1990) 277.

111. G. Barral, F. Njanjo-Eyoke, S. Maximovitch, *Electrochimca Acta*, 40 (1995) 2815.

112. M. Boinet, S. Maximovitch, F. Dalard, O. de Bouvier, *J. Mat. Sci.*, 38 (2003) 4041.

113. A. Delahaye-Vidal, B. Beaudoin, N. Sac-Epée, K. Tekaia-Elhsissen, A. Audemer, M. Figlarz, *Solid State Ionics*, 84 (1996) 239.

114. J. McBreen "The Nickel Oxide Electrode" in "Modern Aspects ofElectrochemistry", Vol. 21, Eds. R.E. White, J.O'M. Bockris, B.E. Conway, Plenum Press, New York 1990, pp. 29-63.

115. W. Visscher, E. Barendrecht, *Electrochimica Acta*, 25 (1980) 651.

116. D. Floner, C. Lamy, J.M. Leger, *Surf. Sci.*, 234 (1990) 87.

117. K. Watanabe, T. Kikuoka, N. Kumagai, *J. Appl. Electrochem.*, 25 (1995) 219.

118. S.L. Medway, C.A. Lucas, A. Kowal, R.J. Nichols, D. Johnson, *J. Electroanal. Chem.*, 587 (2006) 172.

119. F. Hahn, B. Beden, M.J. Croissant, C. Lamy, *Electrochimica Acta*, 31 (1986) 335.

120. T.C. Wen, C.C. Hu, Y.J. Li, *J. Electrochem. Soc.*, 140 (1993) 2554.

121. J. Desilvestro, D.A. Corrigan, M.J. Weaver, *J. Phys. Chem.*, 90 (1986) 6408.

122. C.A. Melendres, W. Paden, B. Tani, W. Walczak, *J. Electrochem. Soc.*, 134 (1987) 762.

123. V. I. Birss, M. Chang, J. Segal, *J. Electroanal. Chem.* 355 (1993) 181.

124. G. Vatankhah, J. Lessard, G. Jerkiewicz, A. Zolfaghari, B.E. Conway, *Electrochim. Acta* 48 (2003) 1613.

125. G. Jerkiewicz, G. Vatankhah, J. Lessard, M.P. Soriaga, Y.S. Park, *Electrochim. Acta* 49 (2004) 1451.

126. M.E. van der Geest, N.J. Dangerfield, D.A. Harrington, *J. Electroanal. Chem.* 420 (1997) 89.

127. G. Jerkiewicz, in: A. Wieckowski (Ed.), *Interfacial Electrochemistry*, Marcel Dekker, New York, 1999, Chapter 32.

128. D.A. Harrington, *J. Electroanal. Chem.* 420 (1997) 101.

129. J.R. McBride, G.W. Graham, C.R. Peters, W.H. Weber, *J.Appl. Phys.* 69 (1991) 1596.

130. Corrosion: Meta/Environment Reactions, Eds.: L.L. Shreir, R.A. Jarman, G.T. Burstein, Butterworth-Heinemann, Oxford 2000.

131. K. Juodkazis, J. Juodkazytė, R. Vilkauskaitė, V. Jasulaitienė, *J. Solid State Electrochem.*, 12 (2008) 1469.

132. B. Beden, A. Bewick, *Electrochimica Acta*, 33 (1988) 1695.

133. A. Kowal, C. Gutiérrez, *J. Electroanal. Chem.*, 395 (1995) 243.

134. A. Seghiouer, J. Chevalet, A. Barhoun, F. Lantelme, *J. Electroanal. Chem.*, 442 (1998) 113.

135. D.M. MacArthur, *J. Electrochem. Soc.*, 117 (1970) 422.

136. G. Barral, S. Maximovitch, F. Njanjo-Eyoke, *Electrochimica Acta*, 41 (1996) 1305.

137. A. Seyeux, V. Maurice, L.H. Klein, P. Marcus, *J. Electrochem. Soc.*, 153 (2006) B453.

138. R.S. Schrebler-Guzmán, J.R. Vilche, A.J. Arvia, *J. Electrochem. Soc.*, 125 (1978) 1578.

139. R.S. Schrebler-Guzmán, J.R. Vilche, A.J. Arvia, *J. Appl. Electrochem.,* 9 (1979) 183.

140. H Gómez Meier, J.R. Vilche, A.J. Arvia, *J. Appl. Electrochem.,* 10 (1980) 611.

141. M. Dmochowska, A. Czerwiński, *J. Solid State Electrochem.*, 2 (1998) 16.

142. Z.I. Kudryavtseva, L.A. Burkal'tseva, A.G. Pshenichnikov, *Russ. J. Electrochem.*, 40 (2004) 1208.

143. J.C. Vickerman, I. Gilmore, Surface Analysis: The Principal Techniques, Wiley, 2009.

144. B.P. Payne, A.P. Grosvenor, M.C. Biesinger, B.A. Kobe, N.S. McIntyre, *Surf. Interface Anal.*, 39 (2007) 5823

145. A.P. Grosvenor, M.C. Biesinger, R.S.C. Smart, N.S. McIntyre, *Surf. Sci.*, 600 (2006) 1771.

146. K.S. Kim, N. Winograd, *Surf. Sci.*, 43 (1974) 625.

147. M.C. Biesinger, B.P. Payne, L.W.M. Lau, A. Gerson, R.S.C. Smart, *Surf. Interface Anal.*, 41 (2009) 324.

148. B.P. Payne, M.C. Biesinger, N.S. McIntyre, *J. Electron Spectroscopy Rel. Phenomena*, 175 (2009) 55.

149. E. Asselin, A. Alfantazi, S. Rogak, *Surf. Interface Anal.*, 41 (2009) 489.

150. J.F. Wolf, L.S.R. Yeh, A. Damjanovic, *Electrochimica Acta*, 26 (1981) 811.

151. A. Damjanovic, L.S.R. Yeh, J.F. Wolf, *Electrochimica Acta*, 26 (1981) 825.

152. J.F. Wolf, L.S.R. Yeh, A. Damjanovic, *Electrochimica Acta*, 26 (1981) 409.

153. N. Cabrera, N.F. Mott, *Rep. Prog. Phys.*, 12 (1948) 163.

154. W. Visscher, E. Barendrecht, *Surf. Sci.*, 135 (1983) 436.

155. W. Visscher, E. Barendrecht, *J. Appl. Electrochem.*, 10 (1980) 269.

156. K. Schultze, H. Bartelt, *Int. J. Hydrogen Energy*, 17 (1992) 711.

157. A.G. Pshenichnikov, L.A. Burkal'tseva, Z.I. Kudryavtseva, *Electrochimica Acta*, 45 (2000) 4143.

158. J. Nan, Y. Yang, Z. Lin, *Electrochimica Acta*, 51 (2006) 4873.

159. A. Velon, I. Olefjord, *Oxid. Met.*, 56 (2001) 415.

160. L.H. Dall'Antonia, G. Tremiliosi-Filho, G. Jerkiewicz, *J. Electroanal. Chem.*, 502 (2001) 72.

161. P. Iotov, S. Kalcheva, A.M. Bond, *J. Electroanal. Chem.*, 638 (2010) 275.

162. I.G. Casella, M.R. Guascito, M.G. Sannazzaro, *J. Electroanal. Chem.*, 462 (1999) 202.

163. B. Lesiak, A. Jablonski, Z. Prussak, P. Mrozek, *Surf. Sci.*, 223 (1989) 213.

164. M.A. Tafreshi, S. Csillag, Z.W. Yan, C. Bohm, E. Lefèvre, C. Colliex, *J. Phys. I France*, 3 (1993) 1649.

165. J.F. Watts, An Introduction to Surface Analysis by Electron Spectroscopy, Oxford University Press, Oxford, 1990.

166. J. Végh, *J. Electron Spectroscopy Related Phenomena*, 151 (2006) 159.

167. C.J. Powell, J.M. Conny, *Surf. Interface Anal.*, 41 (2009) 269.

168. S. Oswald, W. Brückner, *Surf. Interface Anal.*, 36 (2004) 17.

169. Y. Pozdeev-Freeman, A. Gladkikh, *J. Electronic Material*, 30 (2001) 931.

170. Microlab 310-F Operators Manual, Rev. 2.0, VG Scientific, Vision Instruments, 1997.

171. M.P. Seah, *Thin solid films*, 81 (1981) 279.

172. H. Oechsner, *Applied Physics*, 8 (1975) 185.

173. J. F. Moulder, W. F. Stickle, P. E. Sobol, K. D. Bomben, Handbook of X-ray Photoelectron Spectroscopy, Physical Electronics Inc., Minnesota, 1995.

174. M. P. F, H. J. Mathieu, Surface Science, 139 (1984) 549.

175. M. Alsabet, M.Sc. Thesis, Queen's University, Kingston, Canada, 2005.

176. S. Maximovitch, *Electrochimica Acta*, 41 (1996) 2761.

177. E. Sikora, D.D. MacDonald, *Electrochimica Acta*, 48 (2002) 69.

178. I. Ishikawa, *Thin Solid Films*, 117 (1996) 281.

179. B.J. Boyle, E.G. King, K.C. Conway, *J. Am. Chem. Soc.*, 76 (1954) 3835.

180. O.D. Gonzalez, G. Parravano, *J. Am. Chem. Soc.*, 78 (1956), 4533.

181. CRC Handbook of Chemistry and Physics, Ed. D.R. Lide, CRC Press, Boca Raton, 1995.

182. S. Mrowec, Z. Grzesik, *J. Phys. Chem. Solids*, 65 (2004) 165.

183. J.S. Choi, W.J. Moore, *J. Phys. Chem.*, 66 (1962) 1308.

184. A. Atkinson, R.I. Taylor, *J. Mat. Sci.*, 13 (1978) 427.

185. K. Maier, H. Mehrer, E. Lessmann, W. Schüle, *Phys. Stat. Solidi*, 78 (1976) 689.

186. M.V. Vazquez, G.F. Darbyshire, R.E. Carbonio, V.A. Macagno, *J. Power Sources*, 25 (1989) 75.

187. D. Berndt in Battery Technology Handbook, Ed. H.A. Kiehne, M. Dekker, 2003, New York.

188. A.K. Shukla, S. Venugopalan, B. Hariprakash, *J. Power Sources*, 100 (2001) 125.

189. C. Zhang, S.M. Park, *J. Electrochem. Soc.*, 136 (1989) 3333.

190. S. Motupally, C.C. Streinz, J.W. Weidner, *J. Electrochem. Soc.*, 142 (1995) 1401.

191. Z. Mao, P. De Vidts, R.E. White, J. Newman, *J. Electrochem. Soc.*, 141 (1994) 54.

192. M.S. Kim, K.B. Kim, *J. Electrochem. Soc.*, 145 (1998) 507.

193. S.I. Cordoba-Torresi, C. Gabrielli, A. Hugot-Le Goff, R. Torresi, *J. Electrochem. Soc*., 138 (1991) 1548.

194. P. Bernard, C. Gabrielli, M. Keddam, H. Takenouti, J. Leonardi, P. Blanchard, *Electrochimica Acta*, 36 (1991) 743.

195. I.C. Faria, R. Torresi, A. Gorenstein, *Electrochimica Acta*, 38 (1993) 2765.

196. M. Gonsalves, A.R. Hillman, *J. Electroanal. Chem.*, 454 (1998) 183.

197. H.M. French, M.J. Henderson, A.R. Hillman, E. Veil, *J. Electroanal. Chem.*, 500 (2001) 192.

198. M.S. Kim, T.S. Hwang, K.B. Kim, *J. Electrochem. Soc.*, 144 (1997) 1537.

199. G.T. Cheek, W.E. O'Grady, *J. Electroanal. Chem.*, 421 (1997) 173.

200. Y. Mo, E. Hwang, D.A. Scherson, *J. Electrochem. Soc.*, 143 (1996) 37.

201. S.I. Pyun, K.H. Kim, J.N. Han, *J. Power Sources*, 91 (2000) 92.

202. T. Ohligschläger, G. Schwitzgebel, *Phys. Chem. Chem. Phys.*, 3 (2001) 5290.

203. M. Wehrens-Dijksma, P.H.L. Notten, *Electrochimica Acta*, 51 (2006) 3609.

204. A.K.M. Fazle Kibria, S.A. Tarafdar, *Int. J. Hydrogen Energy*, 27 (2002) 879.

205. L. Bing, Y. Huatang, Z. Yunshi, Z. Zuoxiang, S. Deying, *J. Power Sources*, 79 (1999) 277.

206. X. Cao, J. Wei, Y. Luo, Z. Zhou, Y. Zhang, *Int. J. Hydrogen Energy*, 25 (2000) 643.

207. S. Deabate, F. Fourgeot, F. Henn, *Electrochimica Acta*, 51 (2006) 5430.

208. X.J. Han, P. Xu, C.Q. Xu, L. Zhao, Z.B. Mo, T. Liu, *Electrochimica Acta*, 50 (2005) 2763.

209. K.P. Ta, J. Newman, *J. Electrochem. Soc.*, 145 (1998) 3860.

210. X.Y. Wang, J. Yan, Y.S. Zhang, H.T. Yuan, D.Y. Song, *J. Appl. Electrochem.*, 28 (1998) 1377.

211. G.W.D. Briggs, P.R. Snodin, *Electrochimica Acta*, 27 (1982) 565.

212. L. Xiao, J. Lu, P. Liu, L. Zhuang, J. Yan, Y. Hu, B. Mao, C. Lin, *J. Phys. Chem. B*, 109 (2005) 3860.

213. H.S. Kim, T. Itoh, M. Nishizawa, M. Mohamedi, M. Umeda, I. Uchida, *Int. J. Hydrogen Energy*, 27 (2002) 295.

214. Y.G. Yoon, S.I. Pyun, *Electrochimica Acta*, 42 (1997) 2465.

215. G.W.D. Briggs, M. Fleischmann, *Trans. Faraday Soc.*, 67 (1971) 2397.

216. D.M. MacArthur, *J. Electrochem. Soc.*, 117 (1970) 729.

217. H. Chen, J.M. Wang, T. Pan, Y.L. Zhao, J.Q. Zhang, C.N. Cao, *J. Power Sources*, 143 (2005) 243.

218. Y.L. Zhao, J.M. Wang, H. Chen, T. Pan, J.Q. Zhang, C.N. Cao, *Electrochimica Acta*, 50 (2004) 91.

219. Z. Takehara, M. Kato, S. Yoshizawa, *Electrochimica Acta*, 16 (1971) 833.

220. G. Gille, S. Albrecht, J. Meese-Marktscheffel, A. Olbrich, F. Schrumpf, *Solid State Ionics*, 148 (2002) 269.

221. S. Motupally, C.C. Streinz, J.W. Weidner, *J. Electrochem. Soc.*, 145 (1998) 29.

222. B. Paxton, J. Newman, *J. Electrochem,.Soc.*, 143 (1996) 1287.

223. M. Opallo, A. Prokopowicz, *Electrochem. Comm.*, 5 (2003) 737.

224. H. Zhou, Z. Zhou, *Solid State Ionics*, 176 (2005) 1909.

225. V. Srinivasan, J.W. Weidner, R.E. White, *J. Solid State Electrochem.*, 4 (2000) 367.

226. D.D. MacDonald, S.J. Smedley, *Electrochimica Acta*, 35 (1990) 1949.

227. W.C. Chen, B.J. Heuser, *J. Alloys Comp.*, 312 (2000) 176.

228. O.M. Katz, E.A. Gulbransen, *Rev. Sci. Instr.*, 31 (1960) 615.

229. D.N. Jewett, A.C. Makrides, *Trans. Faraday Soc.*, 61 (1965) 932.

230. X.Q. Tong, Y. Sakamoto, F.A. Lewis, R.V. Bucur, K. Kandasamy, *Int. J. Hydrogen Energy*, 22 (1997) 141.

231. M. Cappadonia, J. Divisek, T. von der Heyden, U. Stimming, *Electrochimica Acta*, 39 (1994) 1559.

232. P. Elumalai, H.N. Vasan, N. Munichandraiah, *J. Power Sources*, 93 (2001) 201.

233. B. Scharifker, G. Hills, *Electrochimica Acta*, 28 (1983) 879.

234. S. Fletcher, A. Smith, *Can. J. Chem.*, 56 (1978) 606.

235. A.J. Bard, L. Faulkner, Electrochemical Methods. Fundamentals and Applications, Wiley, New York, 1980.

236. A.T. Hubbard, F.C. Anson, *Anal. Chem.*, 38 (1966) 58.

237. K. Aoki, K. Tokuda, H. Matsuda, *J. Electroanal. Chem.*, 160 (1984) 33.

238. A.K. Hjelm, G. Lindbergh, A. Lundqvist, *J. Electroanal. Chem.*, 506 (2001) 82.

239. M.E.G. Lyons, H.G. Fay, J.G. Vos, A.J. Kelly, *J. Electroanal. Chem.*, 250 (1988) 207.

240. D. Benito, J.J. García-Jareño, J. Navarro-Laboulais, F. Vicente, *J. Electroanal. Chem.*, 446 (1998) 47.

241. C.A. Melendres, S. Xu, *J. Electrochem. Soc.*, 131 (1984) 2239.

242. A. Kowal, R. Niewiara, B. Perończyk, J. Haber, *Langmuir*, 12 (1996) 2332.

243. X. Zuo, C. Xu, H. Xin, *Electrochimica Acta*, 42 (1997) 2555.

244. P.J. Kulesza, Z. Galus, *J. Electroanal. Chem.*, 323 (1992) 261.

245. P.V. Stasiukaitis, V. Skominas, *J. Electroanal. Chem.*, 459 (1998) 121.

246. B. Paxton, J. Newman, *J. Electrochem. Soc.*, 144 (1997) 3818.

247. M. Jain, A.L. Elmore, M.A. Matthews, J.W. Weidner, *Electrochimica Acta*, 43 (1998) 2649.

248. D.A. Bonnell, *Prog. Surf. Sci.*, 57 (1998) 187.

249. J.P. Diard, C. Montella, *J. Electroanal. Chem.*, 557 (2003) 19.

250. W.P. Gomes, F. Cardon, *Prog. Surf. Sci.*, 12 (1982) 155.

251. U. König, J.W. Schultze, in "Interfacial Chemistry. Theory, Experiment and Applications", Ed. A. Więckowski, M. Dekker, New York 1999.

252. R. De Gryse, W.P. Gomes, F. Cardon, J. Vennik, *J. Electrochem. Soc.*, 122 (1975) 711.

253. A.J. Bard, R. Memming, B. Miller, *Pure Appl. Chem.*, 63 (1991) 569.

254. R. Pietrzak, R. Szatanik, M. Szuszkiewicz, *J. Alloys Comp.*, 282 (1999) 130.

255. M.J. Pałys, Z. Stojek, *J. Electroanal. Chem.*, 534 (2002) 65.

256. M. Ciszkowska, Z. Stojek, *J. Electroanal. Chem.*, 466 (1999) 129.

257. N.P.C. Stevens, A.M. Bond, *J. Electroanal. Chem.*, 25 (2002) 538.

258. Y. Roichman, N. Tessler, *Appl. Phys. Lett.*, 80 (2002) 1948.

259. G.G. Raju, Dielectrics in Electric Fields, Marcel Dekker, New York, 2003.

260. N. Hirai, H. Tanaka, S. Hara, *Appl. Surf. Sci.*, 130–132 (1998) 506.

261. U. Stimming, *Electrochimica Acta*, 31 (1986) 415.

262. A. Natarajan, G. Oskam, P.C. Searson, *J. Phys. Chem. B*, 102 (1998) 7793.

263. H. Ishii, N. Hayashi, E. Ito, Y. Washizu, K. Sugi, Y. Kimura, M. Niwano, Y. Ouchi, K. Seki, *Phys. Stat. Sol. A*, 201 (2004) 1075.

264. P.Y. Yu, M. Cardona, Fundamentals of Semiconductors. Physics and Materials Properties. Springer, Berlin, 2003.

Appendices

Hydrogen Trapping Effect

The passive Ni(II)/Ni(III) films formed on the metallic Ni electrodes are not perfect and exhibit defects in the structure such as crystal imperfection, non–stoichiometry, ion vacancies and incorporated solution species [176,226,248]. Therefore, it is expected that some of those defects could act as hydrogen traps in the diffusion process and affects the rate of H^+ diffusion and thus the measured *D* values. However, according to our result, those hydrogen traps does not have any influence on the measured *D* values as we will discuss it below. The process of H^+ transport under the conditions of reversible trapping (the trapped proton can be released or de–trapped) could be described by the following equation [214,249]:

$$v_{\text{tot}} = J_{\text{diff}} - v_{\text{trap}} + v_{\text{de-trap}} \qquad \text{(A-1)}$$

where J_{diff} is the rate of diffusion (diffusion flux), v_{trap} and $v_{\text{de-trap}}$ are the rates of H^+ trapping and de–trapping, respectively. The v_{trap} and $v_{\text{de-trap}}$ are expressed as $k_i N_{\text{trap}}$, where k_i is the rate constant of trapping/de–trapping processes and N_{trap} is the concentration of the trap. For small $v_{\text{de-trap}}$ value, the calculated diffusion coefficient will be smaller than the one calculated from typical Fick's–based equations, such as J_{diff} in Eq. A-1. For full discussion of this aspect, we need to estimate the traps concentration. Since Ni(II) compounds posses semiconducting properties, the number of p–type acceptors or defects

located in the depletion zone of the Ni(II) layer can be estimated from Mott–Schottky plots according to the following equation [250-252]:

$$C^{-2} = 2\left(\varepsilon_o \varepsilon_r e N_{trap}\right)^{-1}\left[-\left(E - E_{fb}\right) - k_B T e^{-1}\right] + C_{dl}^{-2} \qquad \text{(A-2)}$$

where ε_r is the dielectric permittivity of a semiconducting layer, N_{trap} is the acceptor concentration (a p–type semiconductor), E_{fb} is the flat–band potential, C_{dl} is the double layer capacitance and e is the elementary charge; the other terms have their usual meaning as defined earlier in this study. The last term represents the double layer capacitance in the potential range where the Mott–Schottky equation is applicable. The double layer capacitance is much smaller than the space charge capacitance, $C_{dl} << C_{sc}$, and it is considered potential independent [252]. In this case, C_{dl} can be neglected and the total measured capacitance is practically equal to the space charge layer capacitance ($C^{-1} = C_{sc}^{-1} + C_{dl}^{-1}$) [252]. The concentration of p–type acceptors (N_{trap}) is calculated from the slope of C^{-2} vs. E plots, assuming $\varepsilon_r \approx 12$ [112]. At room temperature, the calculated N_{trap} values are in the range of 5.1×10^{19} to 2.9×10^{19} cm^{-3}. These values are ca. 2 orders of magnitude smaller than the values reported in [112] for solutions of neutral and basic pH, but much closer to those presented in [177] for high potential values in neutral pH.

The acceptor concentration value could be compared to the concentration of mobile protons in $Ni(OH)_2$, bearing in mind that only one proton participates in transport processes ($Ni(OH)_2 \leftrightarrow NiOOH$ reaction). Using the molecular mass of $Ni(OH)_2$ (92.7 g $mole^{-1}$) and $Ni(OH)_2$ density (4.15 g cm^{-3}) [181], we obtain a concentration of reacting

protons of ca. 2.7×10^{22} cm^{-3} at room temperature. The comparison of this value with the calculated N_{trap} value indicates that the defects or the acceptors could lower the total concentration of reacting protons by about 0.2% only. The thickness of the depleted layer (L) can be estimated from the following equation [253]:

$$L = \frac{\varepsilon_0 \varepsilon_r}{C_{SC}} \qquad \text{(A-3)}$$

where C_{sc} is the space charge capacitance per real surface area. Considering C_{sc} value in the range where a linear C^{-2} vs. E relation is observed (not discussed in this study), we estimated the thickness of the depleted layer which is in the 1 to 3.5 nm range at room temperature. Such obtained values of L are higher than the ones reported for nickel at E_p = 0.5 V, and constitute ca. 2.2 – 7.6 monolayers of β-$Ni(OH)_2$ [9,112]. This indicates that the depleted layer constitutes about 7 – 26% of the total thickness of the Ni(II) layer, as estimated from the charge of peak V.

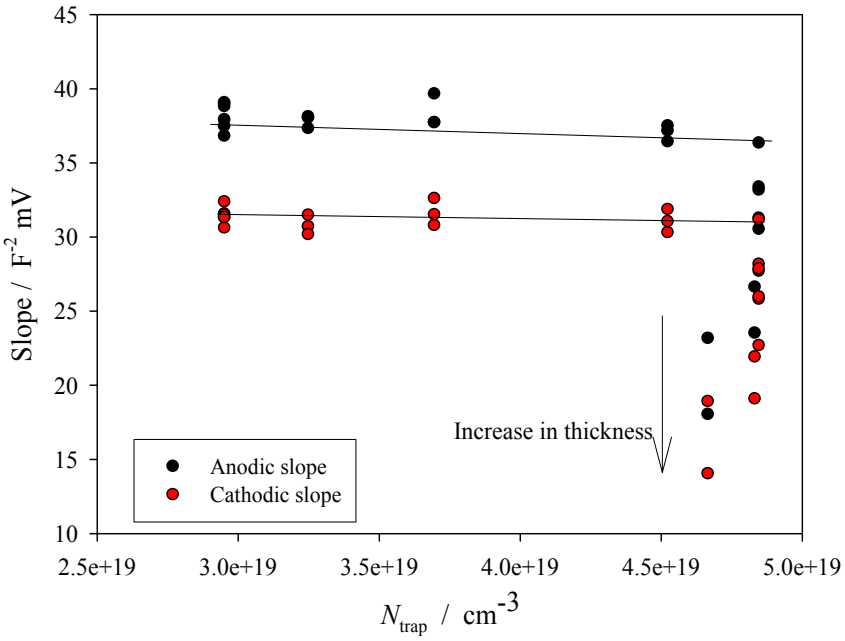

Figure A-1a. Influence of the defects concentration (N_{trap}) on the slope of j_p vs. $v^{1/2}$ relation (anodic and cathodic) calculated on the basis of Fig 6.4 (N_{trap} calculated from Eq. A-2 at $T = 293$ K).

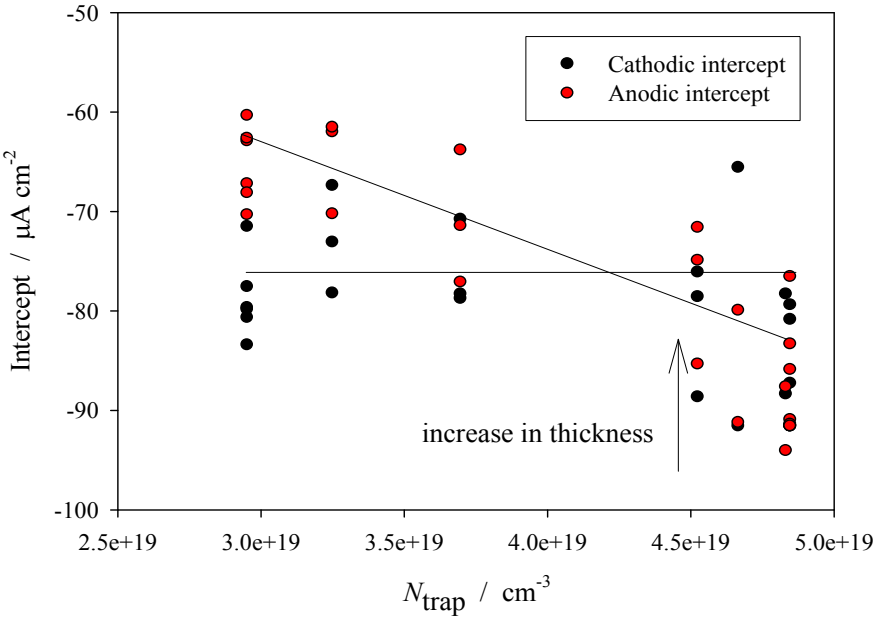

Figure A-1b, Influence of the defects concentration (N_{trap}) on the intercept of j_p vs. $v^{1/2}$ relation with y–axis, for the anodic and cathodic processes, calculated on the basis of Fig 6.4.

In Figs. A-1a and b, we present the influence of N_{trap} on the anodic and the cathodic slopes of j_p vs. $v^{1/2}$ plots (A-1a) and the intercepts of j_p at $v^{1/2}$ with the y–axis (A-1b). We observe that both the slopes and the intersections are apparently N_{trap} independent. One could note that although the oxide thickness increases (see the arrows), the number of defects (N_{trap}) is constant; only the slopes and the intercept change with increase in thickness. This indicates that the number of the defects does not affect the slope or the intercept. From the above results, it follows that the transport of the proton is apparently unaffected by the number of the defects which acts as acceptor sites in the depleted layer. Although the number of the measured defects reflects only a fraction of the total thickness of Ni(II)/Ni(III) layers, it is expected that two–fold increase in the number of the defects in this fraction of the film could influence the proton penetration through it, unless the proton trapping processes are insignificant.

Electric Field Influence on the Proton Migration

The electric field could facilitate or inhibit the proton transport depending on the direction of the H^+ transport [254]. In general, in the presence of migrational and diffusional transport processes, the overall flux of transported species could be presented as [254-257]:

$$J = J_d + q N_c C E \qquad \text{(A-4)}$$

where J_d is the diffusional transport (according to Fick's equations), q is the charge of migrating species, N_c is the species concentration, E is the electric field and C is the

mobility which is related to the diffusion coefficient according to Einstein's relation ($D = C\ k_B\ T\ q^{-1}$) [258,259]. The influence of electric field on the diffusion process was reported for surface diffusion with potential dependence [260].

In the potential region of Ni(II) oxidation, the direction of the electric field should facilitate the transport of H^+ from the electrode towards the solution, i.e. in the same direction as required for a simple $Ni(OH)_2 \rightarrow NiOOH$ reaction, bearing in mind that the oxidation starts at the oxide–solution interface. In this case, the proton transport rate should increase resulting in higher values of the diffusion coefficient. When the migrational transport of H^+ is considered, the shape of the potential drop profile across the passive film must be assumed [261]. The simplest situation is a linear potential drop across the entire film. In this case, the obtained electric field is linearly proportional to the film thickness. In the case of non–intrinsic semiconductors (i.e. depletion or accumulation), a significant part of potential drop is located in the space charge region (SCR). When the space charge layer does not extend to cover the entire thickness of passive film, as in the case of Ni(II) system, an inhomogeneous electric field is distributed across the film. The oxidation of Ni(II) takes place at a potential positive to the flat–band potential, which indicates that during the formation of NiOOH, the hydroxide is under accumulation conditions. Under such conditions, most of the potential drop is located in the electric double layer on the electrolyte side of the interface [262]. When an external electric field is applied to a highly doped semiconductor, screening of the electric field could prevent the penetration of the field deeply inside the semiconductor [263].

On the other hand, it is known that the transport of charged particles is proportional to the surrounding electric field when $qa_xE << k_BT$ (a_x is an interstitial distance between positions) [153]. Based on this relation, we can estimate the importance of the electric field on transport of H^+ in our experimental conditions. The following parameters have been used in our calculation; elementary charge as q (H^+ transport), a_x is 3 or 4 Å (possible distance between H^+ atoms in $Ni(OH)_2$/NiOOH lattice, respectively), E was calculated to be 0.66 V, and the approximate film thickness is ca. 7 nm. The value of the electric field is estimated from the difference between oxidation potential (1.46 V) and the flat band potential (ca. 0.80 V). The obtained qa_xE is in the order of 10^{-20}, which is about an order of magnitude higher than the k_BT value. A comparison of these values indicates that the condition presented above, the influence of the electric field on the transport of H^+ is not fulfilled (a saturation velocity) [264]. Although this calculation contains many simplifications, such as different film thickness and non–homogeneity of potential drop across the film, the final qualitative conclusions will not be changed.

From an electrochemical point of view, an electric field independent of H^+ transport would be interpreted as independent transport of electrode potential and, in turn, of potential scan rate. If so, contribution from migration of H^+ during the transport should move j_p vs. $v^{1/2}$ plots up without changing the slope. As a result, the intersection of j_p vs. $v^{1/2}$ plots with the origin should be positive, instead of negative as is observed on Fig. 6.4. Finally, in [257] it was shown that, for low electrolyte concentration with diffusion and migration transport, the j_p vs. $v^{1/2}$ plots pass through the origin, which is opposite to our experimental findings. Observed in Fig. 6.4, the influence of estimated thickness on the slope and intersection of j_p vs. $v^{1/2}$ plots also rules out significant influence of the electric

field on proton transport. In the case of constant potential drop across the film, the electric field should decrease with increasing the oxide thickness. This leads to slower proton transport in the electric field and a decreased value of j_p vs. $v^{1/2}$ slope. The effect observed in Fig. 6.4 is opposite; the slope first increases and then levels off, indicating that an increase in the thickness facilitates proton transport. This effect, then can be attributed to a thickness dependent composition of Ni(II) or Ni(III) phases, an increase in Ni(III) contribution and/or formation of additional compounds, e.g. NiO, but not to contribution from proton electro–migration.